Assessing hydrometeorological controls on subalpine plant community evapotranspiration and evaluating the METRIC method using high-resolution UAV imagery in the Canadian Rocky Mountains

by

Sheryl Hei Man Chau

A thesis

presented to the University of Waterloo

in fulfillment of the

thesis requirement for the degree of

Master of Science

in

Geography (Water)

Waterloo, Ontario, Canada, 2022

Author's Declaration

I hereby declare that I am the sole author of this thesis. This is a true copy of the thesis, including any required final revisions, as accepted by my examiners.

I understand that my thesis may be made electronically available to the public.

Abstract

Subalpine wetlands in the Canadian Rocky Mountains function as buffers for snowmelt runoff towards downstream systems and communities. However, hydrological regimes are changing rapidly in these ecosystems due to climate warming in the region causing earlier snowmelt patterns and extended vegetation growth periods. Response of vegetation health and composition to temperature and precipitation increases can have a significant influence on evapotranspiration (ET), the main component of wetland water balances. Subalpine plant communities are especially sensitive to shading mechanisms over the growing season, which limits ET flux. However, as the composition of plant communities are expected to migrate with climate, it is important to monitor changes in primary water sinks such as ET in vulnerable ecosystems, such as subalpine wetlands. Due to difficult accessibility, few studies have been conducted to monitor these ecosystems. Recent technological advances in unmanned aerial vehicles (UAV) provide opportunities to monitor these ecosystems at a high spatial resolution.

This study aims to quantify plant community scale ET, assess the spatial variability and sensitivity of this ET to climate and vegetation health, and evaluate the Mapping Evapotranspiration with Internalized Calibration (METRIC) model for ET estimation in a subalpine wetland. ET was measured in-situ using a dynamic closed chamber method for the plant community scale at Fortress Mountain in Kananaskis, Alberta. Vegetation health, water content, and plant water stress was derived from spectral signatures using vegetation indices. High-resolution imagery with multispectral, thermal, and LiDAR sensors were collected during ground measurements to capture the spatial variability of ET throughout the wetland using the METRIC model. Modelled ET was compared with chamber ET measurements to assess the accuracy and applicability of the METRIC model using UAV imagery in a subalpine wetland.

Net radiation and plant community type were the dominant controls on ET at the community scale. Variability in physiological differences between plant communities, such as depth of stomatal openings, cuticle thickness, leaf surface area to volume ratio, and root water uptake rates affect plant response of ET to radiation and temperature. Plant physiology as well as volumetric water content, proximity to surface water, and groundwater connections, also influenced spatial ET trends.

METRIC model results had high estimation accuracy when compared to chamber results. METRIC ET had strong relationship with hourly (R^2=0.79) and daily (R^2=0.82) chamber ET. Taller vegetation (trees and shrubs) had higher estimation accuracy than lower-lying vegetation (ground vegetation and moss). Spatial variability of ET using the local indicators of spatial association (LISA) with METRIC results showed clusters of high ET in the Southern and Western sections of the meadow and low ET in the Northern and Eastern sections of the meadow.

The results of this study demonstrate that as plant communities are expected to migrate with changing climate conditions in subalpine ecosystems, METRIC model applications using UAV imagery could be an effective solution to monitoring plant community ET at a high spatial resolution in vulnerable and inaccessible areas.

Acknowledgements

Table of Contents

List of Figures

List of Tables

Chapter 1: Introduction and Literature Review

1.1 Introduction

The Canadian Rocky Mountains (CRM) are the source of major river systems that provide water to subalpine ecosystems and serve as water supply for the majority of Western Canada (Aber et al., 2012; Debeer et al., 2016). There is an abundance of subalpine wetlands in the CRM that play a critical role in the storage and transmission of this water. These wetlands have unique and diverse hydrological environments (Wissinger et al., 1999), which are characterized by high elevation, cold temperatures, and short growing seasons (Wissinger et al., 1999). Snow or ice cover is present for 8 to 10 months of the year, which affects the species of vegetation that can grow in cold conditions and controls evapotranspiration (ET), the dominant hydrologic flux from these systems (Körner, 2003; Pomeroy et al., 2009). Climate predictions in the CRM indicate longer growing seasons and increasing vulnerability to lower elevation species migration in subalpine wetlands due to rising temperatures, earlier snowmelt, and later snow accumulation (Intergovernmental Panel on Climate Change [IPCC], 2013).

Changes in temperature and precipitation (P) due to anthropogenic climate change can have a significant impact on the hydrological regime including water temperature, P phase and type, snow water equivalent (SWE), discharge, groundwater, lakes, and glacier storage patterns (Hauer et al., 1997; Viviroli & Weingartner, 2004). Warmer temperatures and increased P are expected to promote earlier snowmelt and longer growing seasons, altering moisture regimes and encouraging migration of lower altitude species upslope (Choler, 2005; IPCC, 2013; Grime, 2006). Further, changing climate and increased frequency and intensity of spring flooding, summer drought, and summer forest fires in alpine regions could cause relocation or extinction of subalpine plant species through competitive replacement with lower elevation vegetation (Körner, 2003; Rejmánková et al., 1999). As plant communities change with moisture, temperature, and nutrient regimes (Petrone et al., 2004; Sloat et al., 2015; Xu et al., 2022), increases in ET serve as positive feedback to drought in subalpine ecosystems. As such, climate warming will have significant effects on these habitats, which can be detrimental for subalpine plant species survival, wetland hydrological functioning and downstream water transmission (Aber et al., 2012; Wissinger et al., 1999).

High elevation regions contain some of the most vulnerable ecosystems for climate change as the rate of warming is higher than the global average and is expected to have significant effects on hydrological cycles and plant communities (IPCC, 2013). Over the last 100 years, CRM have shown a statistically significant warming pattern and subsequent glacial retreat (IPCC, 2013; Hauer et al., 1997). Studies show that regional climate warming is closely linked to degradation of alpine wetland ecosystems due to earlier snowmelt timing, longer growing seasons and changes in water availability (Hayashi, 2020; Mitsch & Wu, 1995; Rejmánková et al., 1999; Zhang et al., 2011; Zhao et al., 2010). Subalpine wetlands are directly affected by snowmelt patterns and snowpack thickness from winter snow accumulation and upstream glaciers for long-term water availability (Toetz, 1995). Short-term and long-term changes in snowmelt timing result in water table fluctuations in downstream wetlands, which is the primary control on plant species, distribution, and vegetation health (Wickland et al., 1999). As plant communities evolve over long-term changes in the hydrological cycle, the emergence of new plant species due to climate change effects could alter the ET flux and water use of these ecosystems (Rejmánková et al., 1999).

ET is recognized as one of the major components of the water balance and is quantified to monitor water loss in an ecosystem (Healy et al., 2007; Trenberth et al., 2007). ET is a major process for water loss in subalpine regions and is necessary for monitoring flood management in downstream communities (Brown et al., 2010; Hrach et al., 2021; Oke, 1978). During ET, water is lost to the atmosphere through evaporation from surfaces and transpiration from plants (Oke, 1978). Transpiration occurs at the plant stomata, and stomatal conductance, the measure of stomata opening, is an important factor of transpiration rates (Giménez et al., 2013; Oke, 1978). The controls on transpiration could vary by species and temperature gradients unique to each region and ecosystem (Yan et al., 2019). In the late spring and early summer, cooler air and soil temperatures limit transpiration rates, water uptake and hydraulic conductance from plants and soil (Petrone et al., 2001; Yan et al., 2019). Earlier onset of warmer temperatures in these regions could promote increased transpiration and stomatal conductance (Yan et al., 2019). As the rate of ET is highly dependent on climate and plant species, accelerated warming due to anthropogenic climate change will have a strong influence on ET patterns in subalpine wetlands (Sloat et al., 2015; Xu et al., 2022) and further investigation of ET functionality between plant species and distribution for specific alpine regions should be quantified in order to better understand the impact on downstream systems.

2

ET estimation is often limited by the spatial and temporal resolution of direct or remote sensing measurements, especially in subalpine ecosystems due to difficult terrain within mountainous areas. Many direct measurement methods have been used to calculate ET as point measurements but are often limited in spatial or temporal resolution, and it is difficult to estimate the spatial variability of fluxes within an ecosystem (Jovanovic & Israel, 2012; Jung et al., 2010; Shuttleworth, 2012). As a result, upscaling methods have been used to estimate ET at regional and global scales using direct measurements and satellite imagery (Jung et al., 2010; Zhang, Y. et al., 2016). Process-based upscaling methods extract hydrometeorological variables from imagery to view the spatial distribution of temperature, moisture, and plant species, and further map ET model results to various spatial scales (Aboutalebi et al., 2020; Nieto et al., 2019; Torres-Rua et al., 2020). Models that estimate the temporal and spatial variability of ET are essential for larger scale hydrologic modeling, general circulation models, and flood forecasting models (Allen et al., 2007; Betts et al., 1997; Spies et al., 2015). Since the modeling results are limited to the spatial resolution of the input imagery, increased accessibility to high resolution unmanned aerial vehicle (UAV) imagery will improve estimates of the spatial variability of ET at an ecosystem scale.

1.2 Literature Review

1.2.1 Alpine Hydrology

Hydrological regimes in alpine regions are characterized by winter snow accumulation, glacier volume, spring snowmelt, low rates of ET, autumnal baseflow, and variable P throughout the year (Hauer et al., 1997; Hayashi, 2020; Viviroli & Weingartner, 2004). These regimes are affected by high elevation, temperature, and solar radiation gradients that result in glacial and snowpack formations, mineral soil composition, and sparse vegetation (Dymond & Johnson, 2002; Hayashi, 2020). Snowmelt usually lasts from April through to July; however, peak snowmelt has been occurring earlier due to increased temperatures in the region (Pomeroy et al., 2009; Whitfield & Pomeroy, 2016). Glacier and snowpack volumes have also been decreasing due to the quantity of snowmelt and shorter refreezing periods (Bengtsson, 1982; Pomeroy et al., 2009; Wickland et al.,1999). Accelerated warming due to climate change will have a strong effect on the water balance by altering the quantity and phase of P from snowfall to rainfall, SWE, timing and volume of river discharge, and change in composition, structure and density of plant communities (DeBeer et al., 2016; Hauer et al., 1997; IPCC, 2013).

Orographic effects cause high spatial, seasonal, and interannual variability in temperature and P throughout alpine regions such as the CRM, producing higher amounts of P at higher elevations and on windward slopes (Hauer et al., 1997; Hayashi, 2020; Paznekas & Hayashi, 2016; Smith, 2008). Orography has a major influence on snowpack depth and P patterns, accounting for approximately 37% of P East of the Rockies (Reinelt, 1970; Smith, 2008). Westerly winds originating from the Pacific Coast bring moist air towards the CRM, losing moisture as winds move West to East through orographic lift (Thériault et al., 2021). Although moisture is lost on the leeward slopes of the Coast Mountains before reaching the Rockies, western slopes will still receive high amounts of P due to rising and cooling of air masses (Barry, 1992; Thériault et al., 2021). On the east slope of the Rockies, cold air descends and becomes warmer and drier (Osmond, 1941). Chinook winds, caused by Westerly winds reaching Southern and Central Alberta, are formed on the Eastern downslope and bring warmer temperatures and lower P to Southeastern areas of Alberta and the Prairie region (Nkemdirim, 1996; Osmond, 1941). However, P can occur from air masses moving from the Great Plains and the Gulf of Mexico and up the Eastern slope of the CRM (Hauer et al., 1997; Thériault et al., 2021).

The region is also impacted by the El Niño Southern Oscillation (ENSO) and Pacific Decadal Oscillation (PDO), which influence hydrometeorological conditions (Harder et al., 2015; Hauer et al., 1997). ENSO and PDO can affect hydrometeorological conditions in the Rocky Mountains but are not the sole explanation for changes in alpine hydrology (Harder et al., 2015; Hauer et al., 1997). Effects of ENSO are quantified by the Southern Oscillation Index (SOI), where negative SOI and positive PDO disrupts the flow of cold arctic air into the region, thus increasing temperature and decreasing P, snow accumulation, and streamflow (Whitfield et al., 2010; Newton et al., 2014). Negative PDO and positive SOI effects increases advection of cold arctic air over the region and leads to increased P, streamflow and decreasing temperatures (Whitfield et al., 2010; Newton et al., 2014). Although interannual hydrometeorology are affected by PDO and ENSO, Harder et al. (2015) conclude that climate warming is the most significant variable for temporal changes in P, groundwater, and snow accumulation in the CRM.

Timing, amount, and phase of P are important factors in the alpine water balance and are sensitive to temperatures in the region (Paznekas & Hayashi, 2016). A majority of alpine P occurs in the winter and early spring, when daily average temperatures in the CRM are below 0°C and P falls as snow (Paznekas & Hayashi, 2016). In summer and early autumn, P occurs from advective

cooling and the phase varies with elevation as temperatures are colder at higher elevations (Hauer et al., 1997; Paznekas & Hayashi, 2016). Therefore, most of the snow accumulation in alpine regions occurs in the winter as it requires air temperature to be consistently below freezing for snow P and to maintain the snowpack (Sospedra-Alfonso et al., 2015).

Winter snow accumulation and glacier volume contributes to freshwater recharge in the spring, summer and early autumn through runoff, soil moisture and groundwater (Sospedra-Alfonso et al., 2015). Snowpacks vary in depth and resistance to melt as deeper snowpacks with higher SWE are typically at higher elevations (Hauer et al., 1997; Hayashi et al., 2003). In the Rocky Mountains, snow begins to accumulate in high elevations in mid-autumn and the snowpack continues to grow until late spring or summer depending on temperature (Hauer et al., 1997). Shaded areas sustain snowpacks for longer periods of time and can delay runoff until late summer (Hrach et al., 2021). Snowmelt is the largest contributor to streamflow in the summer as it usually begins in March or April and peaks in May or June (Hauer et al., 1997; Pomeroy et al., 2009). In July and August, streamflow is reduced to baseflow levels and is mostly contributed by groundwater discharge (Hauer et al., 1997; Pomeroy et al., 2009). Diurnal changes in meteorological conditions such as solar radiation, temperature, and P are important drivers for snowmelt and can impact discharge timing and volume (Hauer et al., 1997). In most alpine regions, snow from winter accumulation begins to melt in late spring or summer and contributes to mountain streams as surface runoff and groundwater from saturated soils (Hauer et al., 1997).

Surface runoff and groundwater recharge are important contributors of freshwater to subalpine ecosystems and downstream communities throughout spring, summer, and autumn. Surface runoff from alpine areas contributes to 60% of the annual surface runoff worldwide (Grusson et al., 2015; Viviroli et al., 2003). Runoff efficiency in subalpine areas is typically more sensitive to changes in P (Knowles et al., 2015). The Rocky Mountains produce significantly more runoff than expected for their relative area with a moderate decrease in runoff from mountains to lowlands due to high P due to orographic effect and low evaporation rates due to colder temperatures and sparse vegetation (Hayashi, 2020; Huntingford et al., 1998; Viviroli & Weingartner, 2004). As runoff supplies water in the spring, groundwater recharge supplies water throughout the summer and autumn to downstream systems (Hauer et al., 1997; Hayashi, 2020). Groundwater stored in bedrock depressions and saturated soils supply moisture to subalpine vegetation throughout the summer (Hayashi, 2020).

The alpine water balance is sensitive to temperature, which continues to change with regional warming (DeBeer et al., 2016; Dymond & Johnson, 2002; IPCC, 2013). Daily minimum temperatures in Southwestern Canada are continuing to rise along with annual P increasing 5-35% in the last century (Zhang et al., 2000). Warming can cause regional climate patterns to shift to higher altitudes and latitudes, altering long-term patterns and interannual variability of P, ET, snowmelt timing, and spring freshet (Hannah et al., 2007; Lapp et al., 2005). Mid-latitude alpine glaciers are retreating at a rate of 5 to 20 meters per year (IPCC, 2013). Interannual glacier and snowpack volume continues to decrease with higher temperatures due to longer melting periods in the summer, shorter refreezing and accumulation periods in the spring and autumn, and increased rate of sublimation of snowpack in the winter and spring (Bengtsson, 1982; Hauer et al., 1997; Knowles et al., 2015; Pomeroy et al., 2009; Wickland et al., 1999). Total discharge from spring runoff could be significantly reduced, causing lower levels of soil moisture and groundwater recharge, runoff, and streamflow (Hauer et al., 1997). Both snowmelt fed and glacier fed streams would be impacted by glacier ablation or disappearance (Hauer et al., 1997).

Long-term warming scenarios in the CRM show a significant decline in winter snow accumulation and spring runoff volumes (Lapp et al., 2005). Snowpack in the mountains is expected to decrease over time, which would lead to lower SWE and lower volumes of water available for downstream communities (Lapp et al., 2005; Rinehart et al., 2008). Studies show that as the rain-to-snow ratio increases with warming climate, and rainfall generates more streamflow than snowfall, downstream communities are at higher risk of flooding from the change in P phase (Dingman, 2015; Harder et al., 2015; Lapp et al., 2005; Whitfield, 2012). As climate projections show higher frequency of heat waves and annual warming trends in alpine areas, earlier snowmelt timing and higher volume of meltwater is expected to flow to downstream communities during the spring and summer months (IPCC, 2013).

Increased rainfall and earlier snowmelt timing can cause late spring or early summer flooding and subsequent spring runoff in mountain regions (Barros et al., 2017; Leith & Whitfield, 1998). In the CRM, P is increasing in volume in multiple day events, interannual variability, and spring P volume (Harder et al., 2015). P phase is increasingly shifting from snowfall to rainfall due to warmer air temperatures (Harder et al., 2015). As rain-on-snow P contributes to faster rates of snowmelt, especially at lower elevations, the volume of snowpacks is significantly declining due to increasing rainfall P (Harder et al., 2015; Whitfield, 2012). Rainfall runoff will increase in late

autumn and early winter, as higher temperatures contribute more rainfall than snowfall P (Harder et al., 2015; Leith & Whitfield, 1998). Higher streamflow in the late autumn and early winter period leads to earlier spring runoff and reduced late summer and early fall streamflow in the following year (Kerkhoven & Gan, 2011; Leith & Whitfield, 1998; Whitfield & Pomeroy, 2016). The change in P phase occurring in spring and autumn prolongs the snowmelt period of glaciers and snowpacks, leading to earlier and longer growing seasons and shorter snow- or ice-covered periods (Harder et al., 2015; Lapp et al., 2005; Parker, Vinebrooke & Schindler, 2008).

Seasonal response of ET is expected to change with longer and earlier growing seasons. Earlier snowmelt timing could result in higher water table fluctuations in spring leading to drought and could influence moisture regimes controlling ET rates in wetlands (Brown et al., 2010; Xu et al., 2022). Early season ET in snowmelt-fed systems, such as subalpine wetlands, is heavily reliant on snowmelt timing, as snow or ice cover prevents radiation from reaching underlying vegetation and frozen soil (Brown et al., 2010). Since the albedo of exposed surfaces is lower than snow, more radiation is absorbed and surfaces warm at a higher rate, leading to a positive feedback loop with higher net radiation, temperature, and thus ET (IPCC, 2013; Oke, 1978; Pomeroy et al., 2003).

Alpine and subalpine ecosystems have low ET rates relative to lowland ecosystems due to sparse vegetation cover and lower temperatures (Hayashi, 2020). These areas have colder soil temperatures, which increases the viscosity of water and limits the uptake and transpiration from plants (Yan et al., 2019). Although ET in subalpine areas is usually highest during the summer due to transpiration (Knowles et al., 2015), seasonal variability in P, snow cover and water table melt rates can change the ET rates of a site (Brown et al., 2010). With warming temperatures, water uptake and transpiration may increase in plants or encourage species migration from lowland plant communities (Harte et al., 2006; Yan et al., 2019). Small changes in alpine and subalpine land cover could also alter discharge and ET patterns, as well as the local water balance (Knowles et al., 2015).

Alpine regions contribute a large share of freshwater to the world's population through discharge in lakes and rivers by supplying 40-60% of the total global discharge (DeBeer et al., 2016; Hayashi, 2020; Viviroli & Weingartner, 2004). Communities are often dependent on freshwater resources for energy, agriculture, forestry, mining, and the development of cities

(DeBeer et al., 2016; Lapp et al., 2005; Sospedra-Alfonso et al., 2015; Viviroli & Weingartner, 2004). In the CRM watersheds, many aboriginal communities also rely on freshwater supply from the Mackenzie and Saskatchewan River systems, and demand for potable water increases as downstream populations grow (DeBeer et al., 2016; Lapp et al., 2005). Despite the ecological importance of alpine and subalpine ecosystems for freshwater resources, depletion of these resources is intensifying (DeBeer et al., 2016). Available annual streamflow is particularly important for developing areas with population growth and agricultural activity and depletion of this resource would negatively impact many communities in Western Canada (Lapp et al., 2005).

Wetlands in alpine, subalpine, and lowland regions function as buffers for snowmelt runoff to prevent flooding, droughts, and reduce flood damage in these communities (Aber et al., 2012; Mitsch & Wu, 1995). As snowmelt from glaciers passes through these ecosystems, large quantities of water are stored in the soil and vegetation or lost to the atmosphere before reaching lower lying communities (Aber et al., 2012). As greater populations reside downstream from glacier-fed systems, water storage in wetlands and loss through ET are essential processes for flood management (Aber et al., 2012; Hrach et al., 2021; Whitfield, 2012). Higher temperatures could put these ecosystems at risk of hydrologic change, most notably with summer water table decline due to longer growing seasons, higher ET rates and vegetation health due to plant water stress (Lee et al., 2015; Mitsch & Wu, 1995). Therefore, it is important to evaluate the effect of climate warming on subalpine wetlands, plant species distribution and the associated ET flux.

1.2.2 Alpine Ecohydrology: Role of Wetlands

Climate in alpine regions is characterized by freezing winter and mild summer temperatures, strong and complex wind patterns, and high cloud cover and P (Aber et al., 2012; Hauer et al., 1997; Viviroli & Weingartner, 2004). Radiation is variable due to cloud cover, hill shading, and scattering from adjacent or distant surfaces, resulting in unique microclimates (Dubayah & Rich, 1995; Marsh et al., 2012; Hrach et al., 2021). Responses to microclimate include the spatial distribution of plant species, advective effects, and thermal circulation systems that influence ET of an ecosystem (Oke, 1978). Microclimates are further complicated through shading dynamics that block radiation and reduce temperature and moisture availability (Barros et al., 2017; Hrach et al., 2021; Isard, 1989).

Diurnal and seasonal variability of solar radiation and temperature are determining factors of hydrometeorological processes including ET, P phase, and P quantity (Debeer et al., 2016; Rinehart et al., 2008). ET varies throughout the day, with the highest rates in the early afternoon when incoming solar radiation is high and stomatal conductance is at its peak for photosynthesis processes (Malek, 1992; Monteith, 1963; Oke, 1978). The lowest rates of ET are typically in the late afternoon and nighttime when stomata begin to close due to insufficient lighting or plant water stress, caused by low water content in plant or soil (Oke, 1978). The rate of ET is highest in July and August when radiation and temperature are highest (Hrach et al., 2021; Lafleur et al., 1997). ET occurs more readily under warmer conditions, as heat increases the rate of evaporation and radiation promotes healthier vegetation and stomatal opening (Brown et al., 2010).

Mountain topography affects climatic conditions for ET through shading, temperature, moisture, and wind gradients (Marsh et al., 2012; Oke, 1978; Whittaker et al., 1968). Extreme elevational gradients create shading from immediate topography and surrounding terrain (Marsh et al., 2012). Surfaces can be shaded by different horizon-shadows including self-shadows, which are shadows caused by the direction of the slope from the sun, and hill shade caused by surrounding topography (Marsh et al., 2012). Self-shadows and horizon-shadows have large implications for temperature, energy balance, snowmelt, and ET (Dymond & Johnson, 2002; Marsh et al., 2012). Some areas that are affected by horizon-shade and lower-lying vegetation are also subject to canopy shade (Brown et al., 2010; Marsh et al., 2012). Since stomatal conductance can vary within a leaf and between leaves in different canopy layers (Saugier & Katerji, 1991), canopy shade can reduce ET rates of lower-lying vegetation by reducing incoming solar radiation and leaf-surface interactions throughout the growing season (Brown et al., 2010). While shading decreases incoming solar radiation at the surface, scattered radiation from surrounding terrain can increase the incoming longwave radiation at the surface (Rinehart et al., 2008). As ET occurs most effectively during periods of high solar radiation, shading and radiation scattering in mountainous regions can have a significant effect on the radiation and water balance (Brown et al., 2010; Rinehart et al., 2008; Hrach et al., 2021).

Spatial variability of temperature and moisture regimes determine vegetation composition and distribution, which is a significant control on wetland ET (Brown et al., 2010; Petrone et al., 2004; Smith et al., 1993; Whittaker et al., 1968). Wetlands are often covered by non-vascular plants such as mosses in wet conditions and lichens in dry conditions (Chapin III et al., 1996). As

vascular plants dominate in warmer and moderately wet growth conditions, longer growing seasons could result in increased abundance in vascular plants, decreased cover of non-vascular plants, decreased species diversity and species evenness (Chapin III et al., 1996; Rejmánková et al., 1999; Walker et al., 2006). Heterogeneity in plant species and distribution can change the ET rate at community and ecosystem scales (Saugier & Katerji, 1991). Lichens dominate in drier soil conditions but have lower rates of ET and contain different elements than mosses, which could affect soil nutrient dynamics after plant decomposition (Brown et al., 2010; Chapin III et al., 1996; Culicov & Yurukova, 2006; Harte et al., 2006). Additionally, broadleaf trees are expected to migrate upslope in alpine areas, competitively replacing conifer trees (Sloat et al., 2015; Xu et al., 2022). Plant productivity is also limited by stomatal size and density, which varies between species (Oke, 1978). Therefore, the response of ET to changing landscapes will depend on the spatial distribution of plant species, moisture, and temperature regimes, which is changing with climate warming projections.

Plants at higher elevations have different functional properties due to temperature and radiation differences (Körner et al., 1989). The short growing seasons, variable radiation, and cold conditions of subalpine wetlands are an adverse environment for most species (Körner, 2003). However, subalpine plants have adapted over millennia and a unique distribution of plant species thrive in these colder conditions (Aber et al., 2012; Körner, 2003). Subalpine vegetation is usually restricted to frost-resistant species as these ecosystems are subject to extreme cold temperatures and snow cover for long periods of time (Aber et al., 2012). Elevation, slope, and aspect determine the amount of incoming solar radiation that reaches the surface and the shading patterns that dictate spatial variability of temperature and plants species (Aber et al., 2012; Allen & Peet, 1990; Duguay, 1993; Dymond & Johnson, 2002; Whittaker et al., 1968). Due to high elevation, plants in subalpine ecosystems experience low productivity, biomass, and coverage (Whittaker et al., 1968). Dense, low plant canopies at high elevation are efficient at thermal energy and nutrient storage (Körner et al., 1989). It is well documented that plant height, specific leaf area, and dry matter is decreased at higher elevations, while leaf thickness and stomatal density is increased (Körner, 2003; Körner et al., 1989; Stanisci et al., 2020). Since alpine plants are genetically shorter and have smaller flowers than other plants, they would have low competitive ability for light from taller plants that could migrate from lower elevations (Körner et al., 1989; Stanisci et al., 2020). Taller plants also reduce albedo when they grow above snow cover, leading to an increase in

surface and air temperature (Chapin III et al., 1996). These physical differences between alpine and lower-lying vegetation could influence climate conditions and the rate of ET.

Drought, flooding, and other large fluctuations in the water table can also alter the distribution of plant species and overall ET, as P and soil moisture are main determinants of ET in high-elevation wetlands (Coners et al., 2016; Petrone et al., 2004; Wickland et al., 1999). As temperature and P regimes increase in high elevation regions (Shea & Marshall, 2007), the prolonged periods of warm weather can dry out soil and vegetation that has adapted to moist conditions, making this environment at risk for longer and more frequent periods of drought and forest fires (Rejmánková et al., 1999; Schoennagel et al., 2004). In the Rocky Mountains, streamflow is increasingly lower in late summer and early fall, contributing to drought conditions in downstream ecosystems (Kerkhoven & Gan, 2011; Rood et al., 2008). Spring flooding and summer drought periods could impact species diversity and distribution of plants, and further change the rate of ET in subalpine wetlands (Dymond & Johnson, 2002; Petrone et al., 2015). ET is largely driven by species distribution and species composition (Stanisci et al., 2020), which is heavily impacted by temperature and moisture gradients that are projected to change at an accelerated rate due to anthropogenic climate warming (IPCC, 2013; Whittaker et al., 1968). As plant stomata close to retain water during periods of drought, summer drought frequency and intensity is expected to increase and reduce ET due to plant water stress (Barros et al., 2017; Oke, 1978). Long-term drought cycles can have lasting effects on plant abundance and biomass and could eliminate some plant species permanently (Clark et al., 2016; Rejmánková et al., 1999). Although high elevation plants usually have higher stomatal conductance compared to lower elevation vegetation (Körner, 2003), higher frequency and intensity of drought could reduce stomatal conductance and lower the rate of ET through reduced water availability.

As CRM temperatures continue to rise, the diversity and distribution of plant species in subalpine wetlands will be impacted (Cui et al., 2009; Stanisci et al., 2020). The distribution of ecosystems and biomes are projected to move to higher elevations in alpine regions, displacing many alpine species with lower-lying species (Choler, 2005; Hoegh-Guldberg et al., 2018). Regional warming of 1.5°C is likely to have severe impact on species diversity, while a warming of 2°C to 3°C could result in critical loss of alpine habitats (Hoegh-Guldberg et al., 2018). Alpine regions contain unique plant biodiversity, which has evolved and adapted in cold and adverse conditions (Hoegh-Guldberg et al., 2018). As species diversity is determined by the moisture

gradient and nutrient availability in an ecosystem, plant species are limited by variable water levels and nutrient-poor soil (Hauer et al., 1997; Rejmánková et al., 1999; Whittaker et al., 1968). Water table fluctuations are common in mountain ecosystems that rely on snowmelt timing and high P for water availability (Rejmánková et al., 1999). Alpine soils contain low nutrient concentration in comparison to similar ecosystems in lower elevations, and subalpine plants have adapted defences for survival (Nybakken et al., 2011). Nutrients are stored in winter snowpacks that begin to melt in the spring and enter soils through the surface and groundwater (Hauer et al., 1997). Subalpine plant species are dependent on moist conditions supplied by groundwater throughout the summer (Hayashi, 2020). As anthropogenic climate change affects the timing, magnitude, and frequency of flood events, the flux of water, nutrients, and biota can affect ecosystem biodiversity and integrity (Chapin III et al., 1996; Hauer et al., 1997; Whitfield, 2012).

Subalpine wetlands in the CRM are an ecologically significant and rapidly changing habitat for unique plant and animal species (Aber et al., 2012; Hrach et al., 2021). Wetland ecosystems have been recognized for their species diversity, hydrological importance, and nutrient and gas cycling (Aber et al., 2012; Mitsch & Wu, 1995). The biophysical function of these ecosystems is expected to change significantly with anthropogenic climate change (Wissinger et al., 1999). Many of the subalpine wetlands within CRM serve as important ecosystems for plant species that are sensitive to habitat change (Aber et al., 2012; Wissinger et al., 1999). Extreme events such as droughts, flooding and fires are expected to increase due to increased climate variability in alpine ecosystems (Rejmánková et al., 1999; Schoennagel et al., 2004; Whitfield, 2012). Climate change affects the plant species and composition of these ecosystems, further compromising the hydrologic function and carbon uptake that is governed by native plant species (Harte et al., 2006; Wissinger et al., 1999). As ET is an important control for water loss in subalpine wetlands, it is important to monitor ET and plant biodiversity to understand the ecological trajectory of these ecosystems as well as the resiliency of their role as storage reservoirs and transmitters of water to downstream systems.

1.2.3 Evapotranspiration Modelling and Measurements

ET is the largest flux in the global terrestrial water balance and is an important indicator of water availability and ecosystem health at local, regional, and global scales (Healy et al., 2007; Jung et al., 2010; Trenberth et al., 2007). ET is largely controlled by vegetation cover, temperature, and

moisture conditions, all of which are expected to change with accelerated climate warming (IPCC, 2013; Jung et al., 2010; Zhang Y., et al., 2016). Wetland ET modelling has traditionally been limited to the spatial scale of satellite imagery, which is often too coarse to examine the spatial variability of wetland plant communities (Zhang et al., 2011). Thus, as climate conditions are changing at various spatial scales, it is important to monitor changes in ET at higher spatial and temporal resolutions to understand interactions between ET and these drivers at local and regional scales (IPCC, 2013; Jung et al., 2010; Zhang, Y. et al., 2016).

Advancements in satellite and UAV imagery collection and improvements in ground-based measurements have provided the ability to monitor ET at various spatial and temporal scales using closed chamber methods, eddy covariance (EC) systems, scintillometry, sapflow, and lysimetry (Armstrong et al., 2019; Diarra et al., 2017; Fang et al., 2016; Jovanovic & Israel, 2012; Shuttleworth, 2012). Remotely sensed imagery provides a method of computing the spatial variability of ET by estimating variables used for ET modeling (Allen et al., 2007; Liu et al., 2016). Temperature, P, plant structure, vegetation health and cover have been estimated from multispectral, thermal, and LiDAR imagery to assess ET at different spatial scales (Chen & Liu, 2020). Satellite imagery is often free and provides consistent measurements of large areas without physical collection from the user (Li et al., 2018; Zhang, Y. et al., 2016), but is often limited by low temporal and spatial resolution and clear skies for visibility (Wang et al., 2020). UAV imagery avoids these limitations but requires physical access to collect data, which can be time consuming and dependent on weather and accessibility to site (Jovanovic & Israel, 2012; Shuttleworth, 2012). Although both methods are more efficient and accurate at capturing the spatial heterogeneity of ET than ground-based measurements, ground-truthing is still a crucial step in remote sensing validation (Shuttleworth, 2012).

As UAVs can capture multispectral, thermal, and LiDAR datasets at a higher spatial resolution than satellite imagery, the spatial resolution of derived variables for ET modeling can be estimated at the plant community scale (Aboutalebi et al., 2020; Niu et al., 2020). Smaller pixel sizes can capture the spatial heterogeneity of temperature, P, plant structure, vegetation health and cover, and reduce the effects of mixed pixel problem at the satellite sub-pixel scale (Li et al., 2018; Liu et al., 2016; Niu et al., 2020). ET upscaling methods use multiple small-scale measurements of model parameters to estimate ET over a larger scale (Jovanovic & Israel, 2012; Liu et al., 2016).

Selection of upscaling methods are based on data availability as well as spatial, temporal, and spectral resolution (Chen & Liu, 2020). Upscaling approaches have been effective in calculating global or regional scale ET estimates from a combination of EC tower networks and satellite or aerial imagery (Armstrong et al., 2019; Fu et al., 2014; Liu et al., 2016). Common upscaling approaches include averaging, geostatistical, machine learning, and simulation methods (Li et al., 2018). Averaging methods, such as arithmetic average and area-weighted average, have good results in homogeneous areas (Li et al., 2018; Liu et al., 2016). Geostatistical methods interpolate values based on the spatial autocorrelation of ET and although they are seldom used for upscaling ET, recent studies have optimized geostatistical methods, such as area-to-area kriging, to upscale ET flux over heterogeneous land cover (Ge et al., 2015; Li et al., 2018; Liu et al., 2016). Machine learning techniques, such as artificial neural networks, support vector machine, and random forest, have been used for upscaling ET estimates and ET model parameters for spatial and temporal modeling (Li et al., 2018; Liu et al., 2016). These upscaling techniques require many direct measurements and/or training samples for accurate results, especially for heterogeneous land cover (Isard, 1986; Jovanovic & Israel, 2012). Simulation methods use empirical relationships and theoretical models to estimate ET using process-based models (Fang et al., 2016; Li et al., 2018). As remote sensing imagery is an essential component to most process-based models (Chen & Liu, 2020; Allen et al., 2007), and is the defining resolution for model outputs, high resolution UAV imagery can be applied for higher resolution spatial estimates of ET.

Chen & Liu (2020) characterize process-based ET estimation models as either temperature-based or conductance-based models. Temperature-based models rely on thermal imagery for surface energy balance modeling, which is limited to clear sky conditions and time of image capture when using satellite imagery (Chen & Liu, 2020; He et al., 2017). As surface temperature is sensitive to latent heat loss and is used to calculate sensible heat flux in surface energy balance models, temperature-based models are most effective at estimating the spatial variability of instantaneous ET in water limited conditions with sparse vegetation cover (Chen & Liu, 2020). Conductance-based ET models rely on shortwave-infrared (SWIR) imagery ($0.9 - 1.7\mu m$) to derive structural information about vegetation to quantify leaf or canopy stomatal conductance (Chen & Liu, 2020). These models are particularly effective at monitoring long-term temporal variation in ET and upscaling instantaneous values of ET to daily values due to long-term record availability of derived leaf area index (LAI) from satellite imagery (Liu et al., 2012). Although,

14

Jiang et al. (2016) reports temporal inconsistencies with long-term satellite-derived LAI due to satellite orbital drift and sensor degradation, vegetation structural parameters typically have less temporal fluctuation than surface temperature and thus conductance-based models are preferred for temporal upscaling (Chen & Liu, 2020). Vegetation structural parameters can also be derived from LiDAR systems, and further used for conductance-based ET models at finer spatial resolution when obtained from UAV systems (Mitchell et al., 2012). However, SWIR sensors have only recently been assessed for UAV deployment, in which the effectiveness can be compromised in geometric performance and high signal-to-noise ratio in low radiation settings (Honkavaara et al., 2016). Therefore, temperature-based models are the most common method for ET modeling using UAV imagery.

Temperature-based models, or energy balance models, estimate ET as a residual of the surface energy balance using a combination of direct measurements and indirect remote sensing methods (Chen & Liu, 2020). Energy transfer at the surface is calculated using the surface energy balance equation in these models (Allen et al., 2007; Tang et al., 2013),

$$R_n = G + H + LE \tag{1}$$

where R_n is net radiation (W m^{-2}), G is the ground heat flux (W m^{-2}), H is the sensible heat flux (W m^{-2}) and LE the latent heat flux (W m^{-2}). ET is then calculated as a residual of the surface energy balance (Chen & Liu, 2020; Tang et al., 2013),

$$ET = (R_n - G - H)/\lambda \tag{2}$$

where λ is the latent heat of vapourization (J kg^{-1}).

Energy balance models can be categorized as one-source (OSEB) or two-source energy balance (TSEB) models (Chen & Liu, 2020; Tang et al., 2013). TSEB models are most suitable for sparsely vegetated study areas with patches of bare soil, as the energy balance is calculated separately for soil and vegetation surfaces (Chen & Liu, 2020; Tang et al., 2013). The temperature gradient within each surface in TSEB models is addressed with directional brightness temperatures obtained from satellite or sensor view geometry (Norman et al., 1995; Tang et al., 2013). Other approaches to obtaining soil and vegetation temperature surfaces include the use of the Light Use Efficiency model (Houborg et al., 2012) and dual viewing angles coupled with radiative transfer modeling (Guzinski et al., 2015; Hoffman et al., 2016). The TSEB-PT is one of the most common

models for UAV imagery and uses a single viewing angle to measure surface brightness temperature from the sensor to the Earth's surface at the time of image capture (Aboutalebi et al., 2020; Nieto et al., 2019; Niu et al., 2020; Norman et al., 1995; Torres-Rua et al., 2020). Soil and canopy ET is calculated separately based on brightness temperatures and fractional cover (F_c) or LAI, then sensible, latent, and soil heat fluxes are derived from each surface separately (Norman et al., 1995). Using the Priestley-Taylor approximation, TSEB-PT can estimate the canopy temperature by partitioning net radiation into sensible and latent heat fluxes, thus separating canopy and soil temperatures for calculating canopy and soil ET separately (Norman et al., 1995; Anderson et al., 2007). Several models have modified TSEB-PT to improve on sensible heat flux estimation, including the Dual-Temperature-Difference (DTD) model, Atmosphere-Land Exchange Inverse (ALEXI) model and Disaggregated ALEXI (DisALEXI) model (Chen & Liu, 2020). Hoffman et al. (2016) reported that the DTD model yielded more accurate ET estimates than the traditional TSEB-PT model when compared with EC measurements. However, TSEB-PT is still widely used for high resolution ET mapping using UAV imagery (Aboutalebi et al., 2020; Nieto et al., 2019; Niu et al., 2020; Torres-Rua et al., 2020).

Traditional OSEB models consider the surface as homogeneous, and do not account for differences between vegetated and non-vegetated surfaces, or between different vegetation communities (Tang et al., 2013). However, these surfaces have been separated in some OSEB models using LAI or F_c (Chen & Liu, 2020). Over the past 40 years, OSEB models have developed various methods in calculating sensible heat flux, most notably by defining the temperature gradient between air temperature and aerodynamic surface temperature, the surface temperature at the momentum roughness length (Tang et al., 2013). As the thermodynamic temperatures of soil and vegetation will influence sensible heat flux (Norman et al., 1995), the Surface Energy Balance Algorithm for Land (SEBAL) and Mapping ET with Internalized Calibration (METRIC) are OSEB models that have addressed the temperature gradient by calculating the slope between surface albedo and surface temperature (Allen et al., 2007; Bastiaanssen et al., 1998).

SEBAL uses a combination of field measurements and multispectral, near-infrared, and thermal-infrared imagery to compute surface albedo, vegetation indices, surface temperature, and ET (Bastiaanssen et al., 1998). Surface albedo is used in atmospheric correction, where the darkest pixel is given a value of zero (Bastiaanssen et al., 1998). The slope between surface albedo and surface temperature is used to parameterize the area-effective momentum flux, which is

16

traditionally derived from wind profiles or sonic anemometers (Bastiaanssen et al., 1998). LAI is calculated using vegetation height and the vegetation index output, and further used with field measurements of net radiation to estimate soil heat flux (Bastiaanssen et al., 1998). Field measurements of hydrometeorological variables are used for calculating sensible heat flux (H) and latent heat flux (LE), as well as describing the spatial variability of environmental conditions with empirical relationships (Bastiaanssen et al., 1998). The near-surface temperature gradient between aerodynamic surface temperature and air temperature is calculated from H and a linear relationship with surface temperatures from thermal imagery at wet (H = 0) and dry (LE = 0) pixels (Bastiaanssen et al., 1998). Although SEBAL calculates fluxes independently from land cover, these modifications to traditional OSEB models account for the limitations of absolute surface temperatures from thermal imagery, lack of wind profile or sonic anemometers for calculation of momentum flux, and the spatial variability of soil heat flux (Allen et al., 2007; Bastiaanssen et al., 1998; Chen & Liu, 2020).

METRIC uses the SEBAL model as the foundation for calculating a near-surface temperature gradient and improves on SEBAL by integrating hydrometeorological references, elevation, and the Penman-Monteith equation (Allen et al., 2007; Bastiaanssen et al., 1998; Chen & Liu, 2020). Unlike TSEB-PT, METRIC and SEBAL are OSEB models, which do not calculate the energy balance from vegetated surfaces and soil surfaces separately but include additional parameters accounting for the near-surface temperature gradient, soil heat flux, and area-effective momentum flux (Allen et al., 2007; Bastiaanssen et al., 1998; Chen & Liu, 2020; Tang et al., 2013). METRIC builds upon SEBAL by incorporating additional hydrometeorological and elevational data for atmospheric correction, improved classification of wet and dry pixels, explaining regional advection, and producing higher resolution ET mapping (Allen et al., 2007). Using local hydrometeorological data, wet and dry conditions are classified, and reference ET is calculated using the Penman-Monteith method (Allen et al., 2007). Reference ET is used for calibration in both wet and dry conditions and extrapolation of instantaneous ET for periods of 24 hours and longer to reduce effects of regional advection caused by the traditional method of using evaporative fraction (Allen et al., 2007). Hot and cold pixels are identified in thermal imagery and are adjusted to elevation data for a customized lapse rate to calculate energy balance conditions separately for the wet (cold) and dry (hot) conditions (Allen et al., 2007).

By using local hydrometeorological and topographical data, METRIC is ideal for estimating ET in smaller study areas at a high spatial resolution (Allen et al., 2007). The METRIC model uses satellite imagery to estimate ET at spatial resolution of less than a few hundred kilometers and has been applied to Landsat imagery at a resolution of 30 m (Allen et al., 2007; Carrasco-Benavides et al., 2014). Although the model is traditionally used with satellite imagery, it can also be applied with UAV imagery for higher spatial resolution ET estimates (Niu et al., 2020). With UAV deployment, the spatial resolution of LiDAR-derived DEMs for elevation or LAI and the thermal imagery for classification of hot and cold pixels can be improved for use in the METRIC model (Aboutalebi et al., 2020; Niu et al., 2020).

As ET modeling becomes more sophisticated with new vegetation indices, improved spatial resolution, and adaptation of satellite-based estimation models to UAV imagery, upscaling ET at the local scale can be achieved (Niu et al., 2020). Classifying mixed pixels will be problematic at any spatial scale, however, spatial heterogeneity at sub-pixel scale in satellite images can be captured with higher resolution UAV images (Liu et al., 2016; Niu et al., 2020). With increasing affordability and accessibility, UAVs give researchers the ability to capture imagery of sites at their own leisure, whereas satellite imagery requires clear-sky conditions and coinciding over-pass times (Colomina & Molina, 2014; Wang et al., 2020; Zecha et al., 2013). UAVs may be deployed during cloudy days, but deployment is also limited to drier days with minimal wind speed (Colomina & Molina, 2014; Niu et al., 2020). Upscaling from plot-scale to ecosystem-scale ET using closed chamber methods and UAV imagery-derived variables with the METRIC model can provide spatially continuous ET estimates at a local scale that coarser satellite imagery and EC networks could not capture (Aboutalebi et al., 2020; Colomina & Molina, 2014; Wang et al., 2020; Zecha et al., 2013).

Direct measurements, such as the closed chamber method, can provide ET at the plot-scale, which is useful for identifying spatial variability of ET across a site and for ground-truthing remotely sensed measurements (McLeod et al., 2004; Shuttleworth, 2012; Siewert & Olofsson, 2020). However, these methods are often limited to low temporal resolution, physical access to sites, time constraints, and weather conditions (Siewert & Olofsson, 2020; Simpson et al., 2019; Jovanovic & Israel, 2012). EC systems provide high temporal resolution of ET but records measurements as a spatial average over an ecosystem, which is ideal for upscaling temporally to regional or global scales using satellite imagery (Fang et al., 2016; Siewert & Olofsson, 2020).

18

UAV imagery has been applied in multiple industries, including agriculture, water management, and city planning (Aboutalebi et al., 2020; Colomina & Molina, 2014; Siewert & Olofsson, 2020). As UAVs are becoming more popular for environmental monitoring due to increased affordability and spatial accuracy, studies could incorporate UAV-derived parameters into ET estimation models for high resolution upscaling at the ecosystem scale in vulnerable ecosystems, such as subalpine wetlands.

1.3 Knowledge Gaps

ET of subalpine plant communities is rarely studied due to difficulty in collection and site access. However, the ecological diversity of these regions is at risk of species migration, which can influence ET at the ecosystem scale and downstream water yield (Chapin III et al., 1996; Körner et al., 1989). As climate change influences hydrological regimes in alpine regions and the moisture and nutrient regimes in subalpine wetlands, the spatial and seasonal variability of plants will be affected (Smith et al., 1993). Interactions between radiation, vegetation and topography are critical for understanding the radiation and water balance, especially in montane regions where snow and variable topography is prevalent (Rinehart et al., 2008). Climate change resistance and resiliency of subalpine wetlands can be measured by processes that strongly impact ecological function, including ET (Rejmánková et al., 1999). As ET patterns will be affected by changes in plant species and distribution, it is essential to monitor changes in plant biodiversity and ET as a measure of climate change resistance and resiliency in subalpine wetlands.

Energy balance models have often been applied for landscape or global scale studies due to the limited spatial resolution of satellite imagery. As higher resolution UAV imagery becomes available, energy balance models can be useful for estimating the spatial variability of ET within an ecosystem from individual plant functional types. OSEB models, such as METRIC and SEBAL, have been applied with satellite imagery for ET estimation with high confidence (Niu et al., 2020). However, few studies have used UAV imagery in METRIC applications, especially in subalpine environments. Therefore, further research of UAV applications in subalpine ecosystems is required to assess the spatial variability of subalpine plant community ET at the ecosystem scale and the applicability of METRIC in subalpine environments.

1.4 Research Objectives

The objectives of this thesis are to: (1) determine the sensitivity of ET to plant community species, local meteorological conditions, vegetation health, and plant water stress; (2) evaluate the spatial

variability of ET at a subalpine meadow; and (3) assess the accuracy of METRIC model ET estimations using high-resolution UAV imagery.

Chapter 2: Research site and methodology

2.1 Study Site

This study was conducted at a subalpine wetland on Fortress Mountain in Kananaskis, Alberta (50°49'04" N 115°12'52" W). Fortress Mountain is located in the Kananaskis Range approximately 30 km South of Canmore, Alberta, East of Spray Valley and North of Peter Lougheed Provincial Parks (Figure 1a). The wetland, herein referred to as Bonsai, is characterized as a temporary subalpine marsh meadow and is approximately 2,083 m in elevation and 9,000 m^2 in size (Hrach et al., 2021). Bonsai is north of a 500 m headwall and separated from the headwall base by a talus slope reaching up to 200 m (Hrach et al., 2021). A seasonal tarn, referred to as Bonsai Lake, is located approximately 150 m North and is surrounded by recessional moraines (Christensen et al., 2020). Bonsai Lake is fed by spring snowmelt from two creeks that join approximately 100 m South of the tarn and drains into Galatea Creek. By late summer, both creeks and Bonsai Lake are completely dried out.

A vegetation survey conducted in August 2018 and 2019 determined that the dominant vegetation types are horsetail (*Equisetum hyemale*), tufted fleabane (*Erigeron caespitosus*), willows (*Salix*), larch (*Larix laricina*), subalpine fir (*Abies lasiocarpa*), and brown moss (*Tetrodontium brownianum*) (Hrach et al., 2021; Rooney et al., 2019, unpublished). For this study, measurement locations were divided into 18 plots containing dominant vegetation types across the site. Figure 1 shows the study area with locations of plots and measurement stations, while Table 1 describes the main vegetation type, LAI, and biomass in each plot.
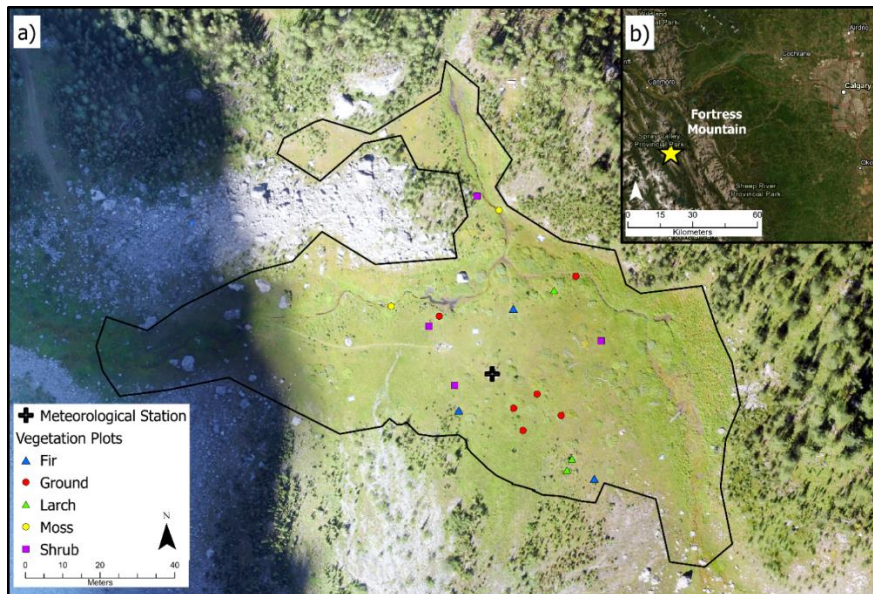
Figure 1. a) Study area map of Bonsai showing surface temperature and meteorological stations and measurement plots; b) Study area location within the southeastern part of the Rockies Mountains in Alberta, Canada.

Table 1. Dominant plant types, LAI, and biomass in plots within Bonsai wetland, Fortress Mountain, Alberta, Canada.

* Ground refers to a mixture of low vegetation, including horsetail and tufted fleabane
** Moss LAI was estimated with linear regression of biomass and LAI in other vegetation plots

Plot	Plant Community	LAI	Biomass (g)
1	Larch	3.40	51.76
2	Larch	4.56	64.19
3	Fir	5.96	63.77
4	Larch	1.71	17.56
5	Shrub	1.84	20.75
6	Ground*	1.74	5.99
7	Shrub	2.43	34.87
8	Ground*	0.97	4.88
9	Ground*	2.38	5.11
10	Ground*	2.28	7.05
11	Ground*	1.96	12.37
12	Ground*	2.36	15.00
13	Shrub	2.02	11.85
14	Shrub	2.94	28.01
15	Fir	6.37	61.36
16	Fir	3.74	47.92
17	Moss	2.57**	10.03
18	Moss	2.72**	11.01

2.2 Field and Lab Methods

2.2.1 Gas Sampling and Analysis

ET fluxes were measured in 18 vegetation plots using a dynamic closed chamber method with an infrared gas analyzer (IRGA) (EGM-4, PP Systems, Massachusetts, USA) from August 24 to September 5, 2020. Each plot contained a circular PVC collar with an area of 317.31 cm^2 inserted approximate 2.5 cm into the soil. Plots were comprised of 3 larch trees, 3 fir trees, 4 shrubs and 8 mixed ground vegetation plots, including 2 moss plots.

ET fluxes were collected during daylight hours according to methods outlined in Brown et al. (2010) and Solondz et al. (2008) using dynamic closed chambers made of clear plexiglass (height=40cm, inside diameter=21 cm). Measurements of relative humidity (RH), air temperature (T_{air}), and photosynthetic active radiation (PAR) were taken using the TRP-2 Temperature & PAR probe (PP Systems, Amesbury, Massachusetts, USA) inside each chamber to determine changes in actual vapour pressure (e) over time. The instantaneous rate of ET could then be calculated using a modified approach from Stannard (1988), based on McLeod et al. (2004),

$$ET_{in} = 3.6\frac{MVC}{A} \tag{3}$$

where ET_{in} is the instantaneous rate of ET (mm h^{-1}), M is the slope of the vapour pressure curve, over the time measurement interval (g m^{-3} s^{-1}), V is the volume of the chamber (m^3), C is a dimensionless calibration factor accounting for vapour absorption in the chamber and A is the surface area covered by the chamber (m^2). Chamber volume included the stick-up height of the PVC collars and excluded the volume occupied by vegetation. The calibration factor for plexiglass is defined in McLeod et al. (2004) as 1.534, and the surface area of each collar was measured as 317.31 cm^2. The result is multiplied by 3.6 to convert ET from g m^{-2} to mm hr^{-1}.

Measurements were logged at 5 second intervals for 2 - 3 minutes at each plot in random order over the study period, to ensure that ET fluxes were captured over a wider range of environmental variables, and to average out effects of different light, temperature and moisture regimes that occur throughout the day (LeCain et al., 2002; Brown et al., 2010: Phillips et al., 2016) using the Transfer Software from PP Systems (Simpson et al., 2019; Stannard, 1988). Data were then divided into sunlit and shaded measurements based on average photosynthetic photon

flux density (PPFD) recorded at the meteorological tower during measurement times and field observations of horizon shading the site. Three measurements were taken during full sunlight (PPFD > 780 µmol m^{-2} s^{-1}) on August 24 and 26, and September 5, 2020. Two measurements were taken during hillshade (PPFD < 480 µmol m^{-2} s^{-1}) on August 31 and September 2, 2020. Although all plots have the same surface area, they vary in leaf area. To normalize data between plant communities, total ET was divided by the LAI of each plot. Since moss do not have leaves, the moss LAI is determined through linear regression of biomass and LAI using all other vegetation plot samples. The results of this study were analyzed with both total ET and normalized ET.

2.2.2 Meteorological Data

A meteorological tower was located approximately at the centre of the study area to measure air temperature and RH at a height of 3.4 m (Vaisala HMP 155, Helsinki, Finland), net radiation (NR4 Net Radiometer, Kipp and Zonen, The Netherlands) and PPFD (Li-Cor 2319, Lincoln, Nebraska, USA) at 3.05 m, and wind speed and direction (R.M. Young 05103 – 10A anemometer, Traverse City, Michigan, USA) at a height of 3.8 m. Soil heat flux was measured at a depth of 5 cm at two locations using soil heat flux plates (Husk Flux Thermal Sensor HFP01, Delft, Netherlands). Soil moisture was measured at 10 cm depth and averaged between two ECH$_2$O EC-5 sensors (Meter Group, Hopkins, Washington, USA), while soil temperature was measured at depths of 5 and 10 cm with Soil Thermistors (Li-Cor 7900 – 180; Nebraska, USA). All data was logged to a CR1000 datalogger (Campbell Scientific, Utah, USA) every 10 seconds and averaged every 30 minutes. Approximately 350 m north, another meteorological station measured P using a tipping bucket rain gauge and event logger (Hoskin Scientific, British Columbia, Canada).

Manual hydrometeorological measurements were taken during chamber measurements, including Forward-Looking Infrared (FLIR) images with a ThermaCAM P20 NTSC (FLIR Systems Inc., Oregon, USA) and soil moisture with a Hydrosense 2 at a depth of 20 cm (Campbell Scientific Inc., Utah, USA) at each vegetation chamber plot. FLIR images were processed in FLIR Tools to identify surface temperature variation between plots. Raw pixel values were converted into surface temperature values using Planck's Law and the Stefan-Boltzmann relationship (Tattersall, 2016),

$$T_s = \frac{B}{\ln\left(\frac{R}{s}\right) + F} \qquad (4)$$

where T_s is surface temperature, B, R, and F are coefficients for the camera lens, and s is radiation. The coefficients for the camera lens were found in the image metadata, while radiation was calculated using emissivity, atmospheric temperature, reflected apparent temperature, RH, and object distance (Tattersall, 2016). An emissivity value of 0.97 from the camera was used, while atmospheric temperature and RH were obtained from the meteorological tower. Object distance was estimated by species height, where ground vegetation was 1 m in distance, while shrubs and trees were 0.5 m in distance. As all vegetation plots had high emissivities and short object distances, reflected apparent temperature was assumed to be equivalent to atmospheric temperature (Senior et al., 2019; Tattersall, 2016).

2.2.3 Spectral Signatures

An ASD FieldSpec 4 Standard-Res spectroradiometer (Analytical Spectral Devices, Inc., Boulder, Colorado, USA) was used to collect spectral signatures of vegetation plots and various land cover across the site (Pomeroy et al., 2020 unpublished data). Red, near-infrared, and shortwave-infrared regions of spectral signatures were analyzed using spectral indices such as Normalized Difference Vegetation Index (NDVI), Water Index (WI), and Plant Water Stress (PWS) to assess vegetation health and water content (Bannari et al., 1995; Peñuelas et al., 1993). NDVI measures vegetation health, where positive values represent vegetated areas and higher values equate to higher chlorophyll content (Yengoh et al., 2015). High chlorophyll content in leaves is correlated with low reflectance of visible red (630-690 nm) light as chlorophyll is known to absorb light in the red wavelength (Bannari et al., 1995; Yengoh et al., 2015). As more dense and green vegetation absorbs less NIR (760-900 nm), healthier vegetation will reflect more NIR (Bannari et al., 1995; Yengoh et al., 2015). NDVI was calculated as the ratio between the difference in reflectance between NIR and visible red wavelengths, and the sum of the two bands (Rouse et al., 1974),

$$NDVI = \frac{NIR - RED}{NIR + RED} \qquad (5)$$

where *NIR* is the amount of reflectance in the near-infrared wavelength (800 nm) and *RED* is the amount of reflectance in the visible red wavelength (680 nm) (Caturegli et al., 2020).

Vegetation water content can be estimated from WI using reflectance in wavelengths of 900 nm and 970 nm where higher values of WI indicate higher water content in both leaves and soil (Peñuelas et al., 1993; Sims & Gamon, 2003). WI was calculated as the ratio between the amount of reflectance at a water absorption band and a reference wavelength (Peñuelas et al., 1993),

$$WI = \frac{R_{900}}{R_{970}} \tag{6}$$

where R_{900} is the reflectance at a reference wavelength (900 nm) and R_{970} is the reflectance at a water absorption band (970 nm). Plant water stress (PWS) is equivalent to WI/NDVI and is an effective indicator of water limitation, where higher values of PWS indicate higher water limitation in plants, reducing water availability for ET (Caturegli et al., 2020):

$$PWS = \frac{WI}{NDVI} \tag{7}$$

2.2.4 UAV Imagery

UAV Imagery was collected during clear, sunny days on August 24 and August 26, 2020 (Pomeroy et al., 2020 unpublished data). Thermal and multispectral imagery was collected on August 26 using a Duet T Thermal Mapping Camera with a RGB and thermal imaging sensor on an eBee X drone (spatial accuracy=1.5cm) and a Parrot Sequoia+ multispectral sensor on an eBee drone (horizontal accuracy=3.0cm). LiDAR imagery was collected on August 24 using a Riegl Mini Vux-1 laser scanner on a DJI M600 Pro drone (vertical accuracy=0.5m, horizontal accuracy=1.5m).

To ground-truth the multispectral imagery, spectral signatures were collected using an ASD FieldSpec 4 Standard-Res spectroradiometer (Analytical Spectral Devices, Inc., Boulder, Colorado, USA) with a corresponding differential GPS (dGPS) measurement (Leica Geosystems, Heerbrugg, St. Gallen, Switzerland) of various land covers across the site (Pomeroy, Harder & Heavens, 2020 unpublished data). Four SI-111-SS surface temperature sensors (Apogee Instruments Inc., Utah, USA) were installed across the site and measurements were sampled every 5 seconds and averaged every minute to a CR10x or CR23x data logger (Campbell Scientific Inc., Utah, USA) for thermal ground-truthing. Harvested LAI measurements were collected at 16 vegetation plots to estimate LAI derived from LiDAR imagery and outputs.

Thermal, RGB, and multispectral images were imported into Pix4Dmapper, where images were georeferenced, radiometrically corrected, and stitched together into mosaics. Multispectral imagery was further calibrated using ground calibration targets and absolute spectral reflectance values using 56 reflectance spectra and dGPS positioning. Using the red and near-infrared (NIR) bands in the multispectral imagery, a NDVI image was generated using Equation 5 for soil heat flux calculation and hot and cold pixel selection (Allen et al., 2007).

2.3 Modelling Approaches

2.3.1 Narrowband-to-Broadband Conversion Model

Land surface broadband albedo is an important parameter for calculations of net radiation, surface temperature and identification of vegetation types, and is a necessary input for the calculation of net radiation, ground heat flux, and cold pixel selection in the METRIC model (Allen et al., 2013; Allen et al., 2007). The broadband albedo can be calculated from multispectral imagery and reference spectrum using a narrowband-to-broadband (NTB) conversion model (Liang, 2001; Tasumi et al., 2008; Xu et al., 2020). Although these models have typically been applied using satellite imagery, broadband or shortwave albedo (α_{SW}) can also be calculated with UAV-based multispectral cameras by integrating the spectral reflectance and solar radiation occurring within the shortwave range (Xu et al., 2020),

$$\alpha_{SW} = \int_{350}^{2500} \rho(\lambda_i)\, R_s(\lambda_i)\, d\lambda \, / \, \int_{350}^{2500} R_s(\lambda_i)\, d\lambda \qquad (8)$$

where ρ is spectral reflectance (%), R_s is solar radiation (W m^{-2}), and λ_i is the wavelength (nm) within the shortwave range of 350 nm to 2500 nm.

The Simple Model of Atmospheric Radiative Transfer of Sunshine software (SMARTS 2.9.5, National Renewable Energy Laboratory, Golden, CO, USA) developed by Gueymard (1995) is a radiative transfer model that provides predictions of solar radiation at the surface using reflectance spectra and atmospheric observations (Tasumi et al., 2008; Xu et al., 2020). Meteorological conditions recorded at the tower at UAV flight time, study site location and elevation, and 56 reflectance spectra samples of moss, ground vegetation, shrubs, fir trees, larch trees, soil, rock, and water were used as inputs for the SMARTS 2.9.5 model simulation. Assuming Lambertian land surfaces, the model produced solar radiation values using different surface types for Equation 8 to estimate the broadband and narrowband albedo for each surface type.

To estimate the narrowband albedo (α_N) of each band in the multispectral imagery, the at-surface spectral reflectance and solar radiation occurring within the upper limit (b_N) and lower limit (a_N) of each band is integrated (Xu et al., 2020),

$$\alpha_N = \int_{a\_N}^{b\_N} \rho(\lambda_i)\, R_s(\lambda_i)\, d\lambda \,/\, \int_{a\_N}^{b\_N} R_s(\lambda_i)\, d\lambda \tag{9}$$

where ρ is spectral reflectance (%), R_s is solar radiation (W m^{-2}), and λ_i is the wavelength (nm). The narrowband albedos of four bands were calculated using the Parrot Sequoia+ multispectral bands: Green (510 – 590 nm), Red (620 – 700 nm), Red-Edge (725 -745 nm), and NIR (750 – 830 nm).

Following the methodology in Liang (2001), linear regression was used to derive a NTB conversion for the Parrot Sequoia+ broadband albedo ($\alpha_{Sequoia}$) using the results from Equation 8 and 9,

$$\alpha_{Sequoia} = -1.549292G + 1.983171R + 0.196258RE + 0.346759NIR + 0.002953 \tag{10}$$

where G is the green band, R is the red band, and NIR is the near-infrared band. As described in Liang (2001), the fitting of Equation 10 was tested using the determination coefficient (R^2) and residual standard error (RSE).

2.3.2 Canopy Height Model

LAI is often an important control on ET and is used to estimate the surface emissivity for outgoing longwave radiation and momentum roughness length when calculating aerodynamic resistance in METRIC (Allen et al., 2007). The availability of light detection and ranging (LiDAR) has brought improved techniques for obtaining biophysical and topographical parameters useful for ET modeling (Aboutalebi et al., 2020; Zheng & Moskal, 2009). LiDAR imaging creates point cloud datasets that represent three-dimensional surfaces allowing examination of vegetation height and LAI at high spatial resolution (Aboutalebi et al., 2020; Zheng & Moskal, 2009). LiDAR pulses penetrate canopies to reach the ground surface and return multiple signals, which can provide vertical information about vegetation and ground cover that two-dimensional imagery cannot capture (Hu et al., 2019).

Wetland vegetation can be difficult to detect in LiDAR datasets due to the short, dense canopies that can often be misclassified as "ground" pixels (Luo et al., 2015). However, plant

height and LAI have been estimated using a canopy height model (CHM) in wetland ecosystems (Hopkinson et al., 2005; Luo et al., 2015). LiDAR imagery was processed in LAStools to filter out noise, classify ground and vegetation pixels, and vegetation height was estimated using CHM,

$$CHM = DSM_{canopy} - DSM_{ground} \tag{11}$$

where *DSM$_{canopy}$* is the digital surface model of the canopy derived from the first returns and *DSM$_{ground}$* is the digital surface model of the ground derived from the ground returns. To estimate LAI, regression using CHM plant height and harvested LAI was performed. The modeled LAI results were assessed using the determination coefficient (R^2) and mean absolute error (MAE).

2.3.3 METRIC Model
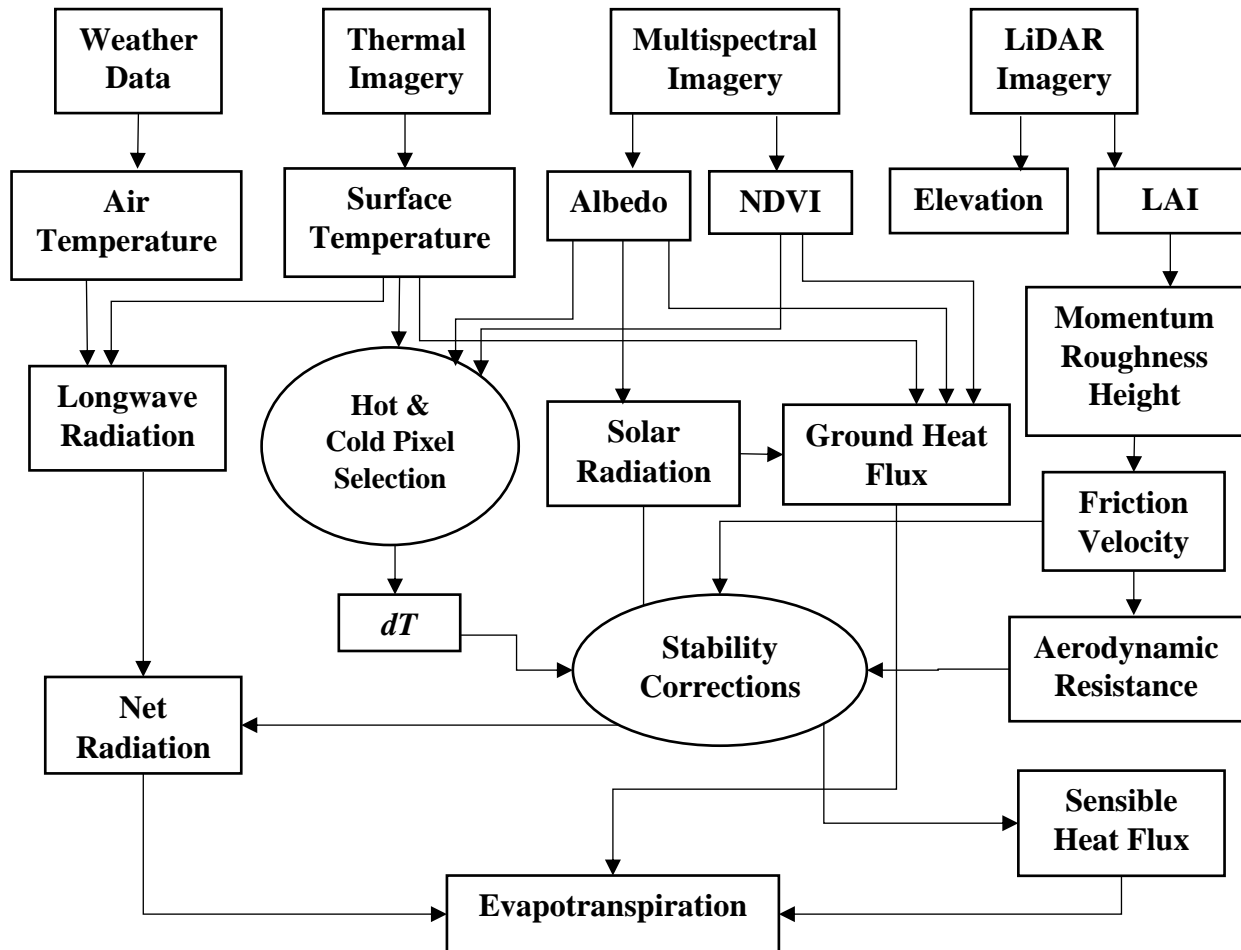
Figure 2. Simplified METRIC methodology diagram.

The METRIC model estimates ET from imagery using the computational methods in the SEBAL model and calibration from a user-selected hot and cold pixel (Allen et al., 2007; Bastiaanssen et al., 1998). Following the SEBAL model, the energy balance is estimated at the surface using multispectral and thermal imagery, vegetation indices, and local meteorological conditions,

$$LE = R_n - G - H \tag{12}$$

where LE is the latent energy (W m^{-2}) used by ET, R_n is net radiation (W m^{-2}), G is the soil heat flux (W m^{-2}), and H is the sensible heat flux (W m^{-2}).

Net radiation (R_n) is calculated with solar radiation, atmospheric transmissivity, and longwave radiation from multispectral and thermal imagery (Tasumi, 2019),

$$R_n = (1 - \alpha)R_s + \varepsilon R_{Ld} - R_{Lu} \tag{13}$$

where α is shortwave albedo, R_s is solar radiation (W m^{-2}), ε is surface emissivity, R_{Ld} is incoming longwave radiation (W m^{-2}), and R_{Lu} is outgoing longwave radiation (W m^{-2}). The α from the NTB model is used, while R_s is calculated as,

$$R_s = \frac{G_{sc} \cos \theta_{rel} \tau_{sw}}{d^2} \tag{14}$$

where G_{sc} is the ASTM-Standard value for the solar constant of 1366.1 W m^{-2}, θ_{rel} is the solar incidence angle (rad), τ_{sw} is broad-band atmospheric transmissivity (dimensionless), and d is the Earth-Sun distance (AU). τ_{sw} is calculated as,

$$\tau_{sw} = 0.35 + 0.627 \exp\left[\frac{-0.00146P}{K_t \cos \theta_{hor}} - 0.075\left(\frac{W}{\cos \theta_{hor}}\right)^{0.4}\right] \tag{15}$$

where P is the atmospheric pressure (kPa), W is the water in the atmosphere (mm), θ_{hor} is the solar zenith angle over a horizontal surface (rad), and K_t is the unitless turbidity coefficient. P is calculated as a function of temperature and elevation,

$$P = 101.3\left(\frac{293 - 0.0065z}{293}\right)^{5.26} \tag{16}$$

where 293 is the standard air temperature (K) from ASCE's standard (Walter et al., 2000) and z is the elevation above sea level (m). W is calculated as a function of atmospheric pressure and near-surface vapor pressure estimated from meteorological conditions at the weather station (Garrison & Adler, 1990),

$$W = 0.14e_a P_{air} + 2.1 \qquad (17)$$

where P_{air} is the atmospheric pressure (kPa) and e_a is near-surface vapor pressure (kPa). K_t was determined using elevation and an assumption of an average sun angle of 45˚ above the horizon (Allen, Hill, & Srikanth, 1994),

$$K_t = 0.75 + (2E - 5)z \qquad (18)$$

The Earth-Sun distance (d) is squared for Equation 19 and is estimated using the Julian day of the year (Duffie & Beckman, 1991),

$$d^2 = \frac{1}{1+0.033\cos(\text{DOY } 2\pi/365)} \qquad (19)$$

where DOY is the Julian day of the year.

The Stefan-Boltzmann equation is used to calculate both incoming (R_{Ld}) and outgoing longwave radiation (R_{Lu}). R_{Lu} is calculated using surface emissivity and surface temperature,

$$R_{Lu} = \varepsilon\sigma T_s^4 \qquad (20)$$

where ε is surface emissivity, σ is the Stefan-Boltzmann constant (5.67×10^{-8} W m^{-2} K^{-4}), and T_s is surface temperature (K). ε is obtained from LAI (Tasumi, 2003),

$$\varepsilon = 0.95 + 0.01\, LAI \ \text{ for LAI} \leq 3 \qquad (21)$$

and $\varepsilon = 0.98$ for LAI > 3, where LAI is leaf area index. R_{Ld} is calculated using atmospheric transmissivity and near-surface air temperature,

$$R_{Ld} = \varepsilon_a\sigma T_a^4 \qquad (22)$$

where ε_a is atmospheric emissivity (dimensionless) and T_a is near-surface air temperature (K). T_a was collected from the meteorological tower and ε_a is calculated using atmospheric transmissivity (Allen et al., 2007; Bastiaanssen, 1995),

$$\varepsilon_a = 0.85(-\ln \tau_{sw})^{0.09} \qquad (23)$$

Soil heat flux (G) is estimated using R_n, T_s and NDVI assuming imagery is collected near midday (Bastiaanssen, 2000),

$$G = R_n(T_s - 273.15)(0.0038 + 0.0074\alpha)(1 - 0.98\,NDVI^4) \qquad (24)$$

31

where R_n is net radiation (W m^{-2}), T_s is surface temperature (K), α is shortwave albedo, and *NDVI* is the Normalized Difference Vegetation Index.

Sensible heat flux (H) is calibrated in METRIC by iteration of the near-surface temperature gradient (dT) and the aerodynamic resistance (r_{ah}) between two near-surface heights defined as z_1 and z_2. In each iteration, H is calculated as,

$$H = \rho_{air} C_p \frac{dT}{r_{ah}} \tag{25}$$

where ρ_{air} is air density (kg m^{-3}), C_p is specific heat of air at constant pressure (1005 J kg^{-1} K^{-1}), and r_{ah} is aerodynamic resistance (s m^{-1}) between z_1 (0.1 m) and z_2 (2 m). ρ_{air} is calculated from a simplified equation of the universal gas law (Allen et al., 1998),

$$\rho_{air} = \frac{1000P}{1.01(T_S - dT)R} \tag{26}$$

where P is mean atmospheric pressure for the pixel elevation (kPa), R is the specific gas constant (287 J kg^{-1} K^{-1}), and ($Ts-dT$) is substitute for near-surface air temperature at the pixel. dT is estimated through a linear relationship with surface temperature (Bastiaanssen, 1995),

$$dT = a + bT_{s\,datum} \tag{27}$$

where a and b are calibration constants from the hot and cold pixels selected in the image and T_s $_{datum}$ (K) is T_s adjusted to an elevation datum and customized lapse rate using a digital elevation model. The first iteration of r_{ah} assumes neutral stability,

$$r_{ah} = \frac{\ln(z_2/z_1)}{u_* k} \tag{28}$$

where u_* is the friction velocity (m s^{-1}) and k is the von Karman's constant (0.41). The first iteration of u_* is computed as,

$$u_* = \frac{k u_{200}}{\ln(200/z_{om})} \tag{29}$$

where u_{200} is wind speed (m s^{-1}) at the blending height (200 m) and z_{om} is the momentum roughness height (m). u_{200} is estimated using the wind speed from the weather station,

$$u_{200} = \frac{u_w \ln(200/z_{omw})}{\ln(z_x/z_{omw})} \tag{30}$$

where u_w is the wind speed (m s^{-1}) measured at the weather station at z_x (m) height above the surface and z_{omw} (m) is the momentum roughness length at the weather station surface. For vegetation less than 1 m in height, z_{om} can be estimated using LAI (Tasumi, 2003),

$$z_{om} = 0.018 \, \text{LAI} \tag{31}$$

Subsequent iterations of u_* and r_{ah} incorporate air stability corrections using the Monin-Obukhov length,

$$u_* = \frac{u_{200} k}{\ln (200/z_{0 \, \text{m}}) - \psi_{m(200 \, \text{m})}} \tag{32}$$

$$r_{ah} = \frac{\ln (z_2/z_1) - \psi_{h(z_2)} + \psi_{h(z_1)}}{u_* k} \tag{33}$$

where $\psi_{m(200 \, \text{m})}$, $\psi_{h(z_2)}$ and $\psi_{h(z_1)}$ are the dimensionless stability corrections for 200 m, z_2 and z_1 respectively. The stability corrections are calculated with the Monin-Obuklov length (L), which represents the height where air stability and mechanical mixing are equal (Allen et al., 2007),

$$L = \frac{\rho_{\text{air}} C_p u_*^3 T_s}{kgH} \tag{34}$$

where g is the gravitational acceleration (9.807 m s^{-1}). All values for L were below 0, indicating that the lower atmospheric boundary layer is unstable and stability corrections are calculated as (Paulson, 1970; Webb, 1970),

$$\psi_{m(200 \, \text{m})} = 2 \ln \left(\frac{1 + x_{(200 \, \text{m})}}{2} \right) + \ln \left(\frac{1 + x_{(200 \, \text{m})}^2}{2} \right) - 2 \arctan \left(x_{(200 \, \text{m})} \right) + 0.5\pi \tag{35}$$

$$\psi_{m(2 \, \text{m})} = 2 \ln \left(\frac{1 + x_{(2 \, \text{m})}^2}{2} \right) \tag{36}$$

$$\psi_{m(0.1 \, \text{m})} = 2 \ln \left(\frac{1 + x_{(0.1 \, \text{m})}^2}{2} \right) \tag{37}$$

where

$$x_{(n \, \text{m})} = \left(1 - 16 \frac{n}{L} \right)^{0.25} \tag{38}$$

where n is the height of each correction (i.e. 200 m, 2 m, and 0.1 m).

The *dT* parameter in Equation 25 is calibrated with a user-selected hot pixel and cold pixel in METRIC (Allen et al., 2007). Hot and cold pixel selection followed the process described in Allen et al. (2013), where hot pixels are filtered for the lowest 10% in NDVI, then the highest 20% in $T_{s\,datum}$. From the filtered hot pixel candidates, a single pixel was selected based on homogeneity with neighboring cells that were within ±0.2 K of the average $T_{s\,datum}$. Cold pixels were filtered for the highest 5% in NDVI, then the lowest 20% in $T_{s\,datum}$. From the population of filtered cold pixel candidates, a pixel was selected based on homogeneity with neighboring cells that was within ±0.2 K of the average $T_{s\,datum}$ and ±0.02 of the albedo (α) threshold determined by (Allen et al., 2013),

$$\alpha_{threshold} = 0.001343\beta + 0.3281 \exp{(-0.0188\beta)} \tag{39}$$

where β is the sun angle (˚) above the horizon.

Equation 25 is then rearranged to solve for *dT* and the surface energy balance from Equation 12 is rearranged to solve for *H* at the location of both the hot and cold pixels. The calibration coefficients (*a* and *b*) for Equation 27 can then be determined using the values for *dT* and $T_{s\,datum}$ (Allen et al., 2007),

$$b = \frac{dT_{hot} - dT_{cold}}{T_{s\,datum\,hot} - T_{s\,datum\,cold}} \tag{40a}$$

$$a = dT_{hot} - bT_{s\,datum\,hot} \tag{40b}$$

where dT_{hot} and dT_{cold} refer to *dT* calculated at the hot and cold pixel respectively and $T_{s\,datum\,hot}$ and $T_{s\,datum\,cold}$ refer to $T_{s\,datum}$ at the hot and cold pixel respectively. The *dT* and r_{ah} parameters in Equation 25 were iterated 6 times until *a* and *b* in Equation 27 and r_{ah} in Equation 25 were stable.

The reference ET (ET_r) for hot and cold pixels is calculated using the standardized ASCE Penman-Monteith equation for short crop ET_r (Walter et al., 2000). The short crop ET_r equation is suitable for estimating the mean evaporative condition for vegetation under 0.12 m in height (Walter et al., 2000). Although some vegetation exceeds 0.12 m in height, a majority of the vegetation at the site are shorter than the alfalfa-based reference (0.5 m). ET at the cold pixel is estimated as $0.50 \times ET_r$ as opposed to the suggested value of $1.05 \times ET_r$ due to lack of irrigation and precipitation and the time of the growing season, as suggested by Allen et al. (2007) and Tasumi (2019). ET at the hot pixel is estimated using the bare soil condition as $0.05 \times ET_r$ from

the FAO-56 manual (Allen et al., 1998) to account for residual evaporation from moist soils after light (8 mm) precipitation from previous weeks.

Finally, instantaneous ET (ET_{inst}) is calculated from the *LE* as a residual from the energy balance,

$$ET_{\text{inst}} = 3600 \frac{LE}{\lambda \rho_w} \tag{41}$$

where ET_{inst} is instantaneous ET (mm h^{-1}), λ is the latent heat of vaporization (J kg^{-1}) and ρ_w is the density of water (~1000 kg m^{-3}) where λ is calculated as,

$$\lambda = [2.501 - 0.00236(T_s - 273.15)] \times 10^6 \tag{42}$$

2.4 Statistical Analysis and Accuracy Assessment

Chamber ET results were tested for normalcy using the Shapiro-Wilks test and statistical significance among plant community groups using the Kruskal Wallis test, while a post-hoc Mann-Whitney-Wilcoxon test was used for comparison of plant community groups. Sunlit and shaded measurements of ET were analyzed separately for statistical significance between plant community groups and shading effects using the Mann-Whitney-Wilcoxon test. Meteorological data and spectral indices were correlated with ET results using multiple linear regression to test for statistical significance of the influence of climatic variables, vegetation health, and plant water stress on ET.

METRIC ET results were validated with dynamic closed chamber ET measurements captured during the same timeframe as the imagery. Although METRIC pixels have an area of 0.09 m^2 and chamber plots represent areas of 0.03 m^2, the vegetation plots were selected in homogenous areas and the average ET_{inst} is compared at the pixel location of each vegetation plot using the determination coefficient (R^2), root mean standard error (RMSE), mean bias error (MBE), and mean relative difference (MRD) described in He et al. (2017).

Spatial variability of average T_s, VWC, and chamber ET measurements were tested for the influence of proximity to the talus slope and the main creek flowing from the west side of the talus slope for each plant community using linear regression. The creek flowing from the east was excluded as it was dry during the study period. Spatial variability of METRIC results was analyzed using Local Moran's I and local indicators of spatial association (LISA) cluster analysis to find clusters and outliers of high and low ET values. The Local Moran's I value measures spatial clustering in the dataset through the correlation between values in each area plotted against the

average value of surrounding areas (Anselin, 1995). Positive spatial autocorrelation or clustering is defined by similar neighbouring values that have a strong deviation from the mean, while negative spatial autocorrelation or outliers are defined by dissimilar neighbouring values that have a strong negative deviation from the mean (Anselin, 1995; Boots, 2002). LISA identifies the type of spatial association based on the location's value and its spatial lag in the Moran scatter plot (Anselin, 1995).

Chapter 3: Results

3.1 Climate Conditions

During the study period from August 24 to September 5, 2020, 4 mm of P was received over 3 rainfall events, with the largest event on September 1 to 2 (3 mm) (Figure 3-A). VWC at the site had a daily average of 38% (±1) and followed trends in P (Figure 3-A). Daily average T_{air} fluctuated between 5˚C and 13˚C (Figure 3-C). Daily average net radiation decreased throughout the study period from 80 Wm^{-2} to 31 Wm^{-2} with 2 days of lower net radiation on August 29 and September 2 (Figure 3-B). Daily average soil temperature at 5 cm and 10 cm ranged from 10˚C to 6˚C over the study period (Figure 3-C). Prior to UAV image collection on August 26, a total of 8 mm of P was received over the previous 2 weeks. On the image collection day, the soils had an average VWC of 36%.
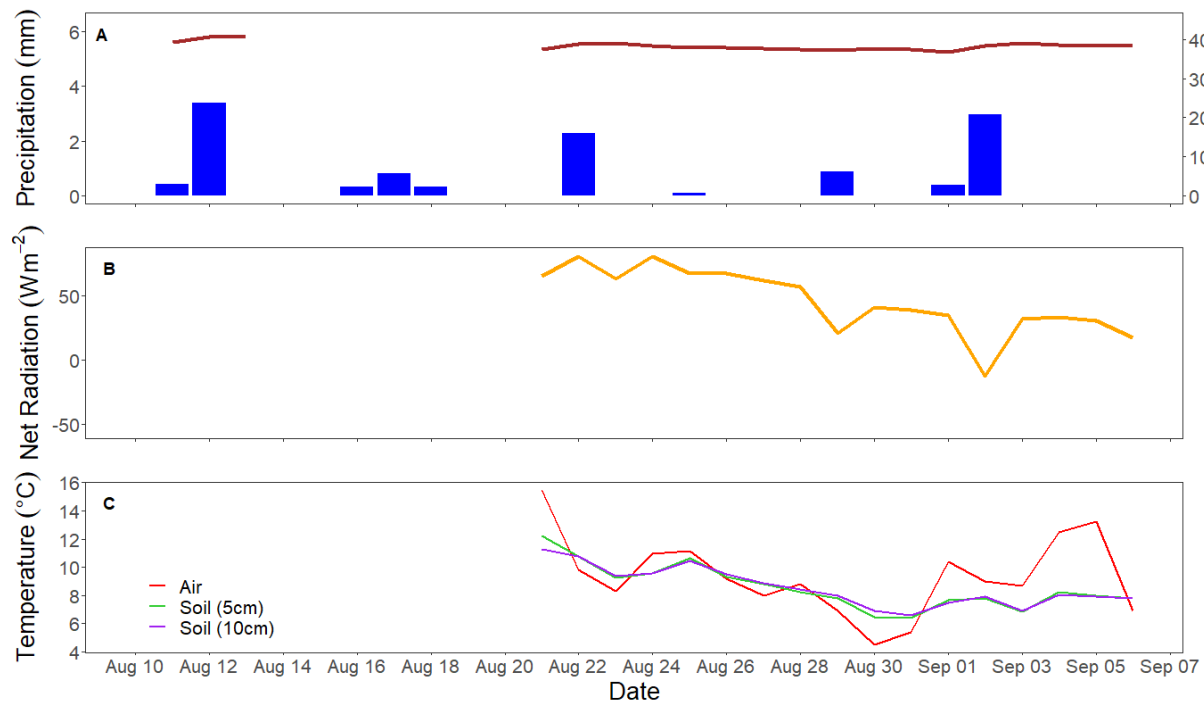
Figure 3. Hydrometeorological conditions measured at Bonsai wetland, Fortress Mountain, Alberta, from August 11 to September 5, 2020 of daily averages of a) precipitation and volumetric water content; and from August 21 to September 5, 2020 of daily averages of b) net radiation; and c) air and soil temperature at 5 cm and 10 cm depths.

On August 26, wind speed, RH, net radiation, and air temperature varied throughout the day. wind speed varied from $0.06 – 2.35$ m s^{-1}, relative humidity varied from $25 – 86\%$, net radiation varied from $-42 – 448$ W m^{-2}, soil heat varied from $-32 – 100$ W m^{-2}, T_{air} varied from $5.2 – 15.4$ °C, and soil temperatures ranged from $6.6 – 13.2$ °C at 5 cm depth and $7.5 – 12$ °C at 10 cm depth (Figure 4). Net radiation drops from 13:00 to 14:00 on August 26 (Figure 4-B) due to horizon shading from the headwall south of the meadow.
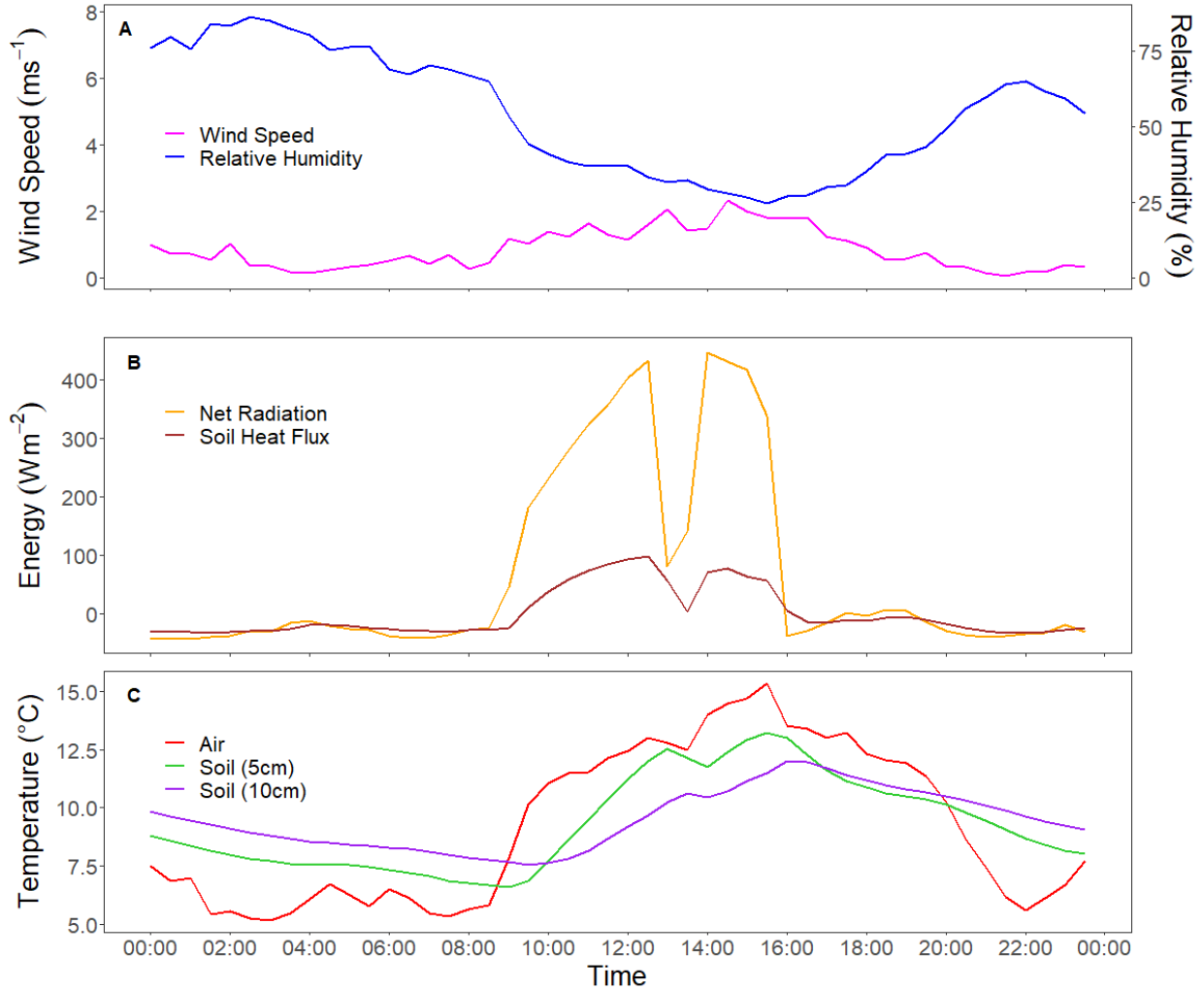
Figure 4. Hydrometeorological conditions measured at Bonsai, Fortress Mountain, Alberta on August 26, 2020. Half-hourly averages of a) wind speed and relative humidity; b) net radiation and soil heat flux; and c) air and soil temperature at 5 cm and 10 cm depths.

Average T_s and VWC of each plot are outlined in Table 2. On August 24 and 26, T_s was obtained using UAV thermal imagery, while the remainder of the measurement days used FLIR camera measurements. T_s between plots varied by as much as 6°C for each measurement day. Excluding the 2 unshaded (PPFD > 480 µmol m^{-2} s^{-1}) temperature measurements taken on September 2, average surface temperatures at all plots at Bonsai on August 24, 26, 31, September 2, and 5 were 18.5°C (±3.5), 18.9°C (±2.7°C), 6.1°C (±1.6°C), 7.0°C (±1.9°C), 10.1°C (±1.8°C), respectively. Soil moisture had a higher variation between plots, ranging from 2.8 – 45.9%, 3.4 – 45.5%, 1.4 – 35.4%, 3.7 – 45.7%, and 3.5 – 45.6%, while the average soil moisture at all plots was 26.6% (±23.4), 24.3% (±21.2), 15.8% (±14.4), 27.8% (±24.1), and 23.7% (±20.2) respectively.

Table 2. Average surface temperature (T_s) and volumetric water content (VWC) of all ET plots at Bonsai, Fortress Mountain, Alberta, during the 2020 study period.

* PPFD > 480 µmol m^{-2} s^{-1} during Ts measurement.

Plot	August 24 (Sun) Ts (°C)	VWC (%)	August 26 (Sun) Ts (°C)	VWC (%)	August 31 (Shade) Ts (°C)	VWC (%)	September 2 (Shade) Ts (°C)	VWC (%)	September 5 (Sun) Ts (°C)	VWC (%)
1	20.5	6.6	18.2	5.1	6.1	4.5	6.8	3.7	10.5	3.5
2	18.9	2.9	17.6	3.4	5.7	1.4	6.6	8.8	10.3	4.6
3	19.1	2.8	18.4	8.9	6.5	5.8	6.9	12.7	11.3	10.9
4	15.7	35.8	20.1	24.8	7.5	13.3	8.4	32.8	11.9	29.9
5	20.3	38.7	20.8	35.9	7.1	16.6	12.7*	40.1	13.6	35.6
6	19.3	31.8	17.8	21.9	5.1	17.0	6.7	27.2	10.1	19.4
7	15.0	29.7	20.2	22.9	6.5	15.7	6.7	31.9	10.5	27.5
8	18.4	31.9	18.9	30.8	6.0	17.9	6.8	32.2	8.8	30.6
9	18.4	41.0	20.1	36.6	6.7	25.3	6.8	42.3	11.2	15.3
10	17.9	26.6	19.4	23.9	6.1	13.1	6.9	24.9	9.1	30.7
11	19.5	29.2	17.7	24.4	5.7	17.3	6.2	29.6	8.8	27.4
12	19.8	21.9	18.2	19.3	5.7	17.7	5.6	24.3	9.1	23.9
13	19.5	20.3	16.9	24.9	5.0	13.4	6.6	29.5	10.4	20.3
14	17.0	30.1	18.6	27.1	4.6	15.3	7.0	32.8	9.9	25.5
15	18.5	20.7	21.6	21.6	6.1	12.1	6.9	13.9	11.4	15.3
16	19.5	45.9	18.3	19.9	6.2	6.8	7.7	23.8	10.2	16.0
17	18.0	43.7	20.8	45.5	7.2	35.4	13.6*	44.6	9.8	44.7
18	18.3	18.9	17.1	41.0	6.3	35.4	8.8	45.7	8.5	45.6

Average VWC and T_s taken during the chamber ET measurements (Table 2) had significant relationships ($p<0.05$) with distance to the main creek flowing from the headwall and the talus slope. Average T_s had a significantly negative moderate relationship ($R^2=0.36$) with proximity to the talus slope but did not have a significant relationship with proximity to the main creek. VWC had a significant positive relationship ($R^2=0.55$; $p<0.05$) with proximity to the main creek and a significant negative moderate relationship ($R^2=0.53$; $p<0.05$) with proximity to the talus slope.

3.2 Spectral Indices

Spectral signatures of plant communities measured on August 24 are shown in Figure 5. The larch tree and ground vegetation communities had the highest average reflectance in red and lowest average in NIR. The fir tree and moss communities had the lowest average reflectance in red highest average reflectance in NIR (Figure 5).
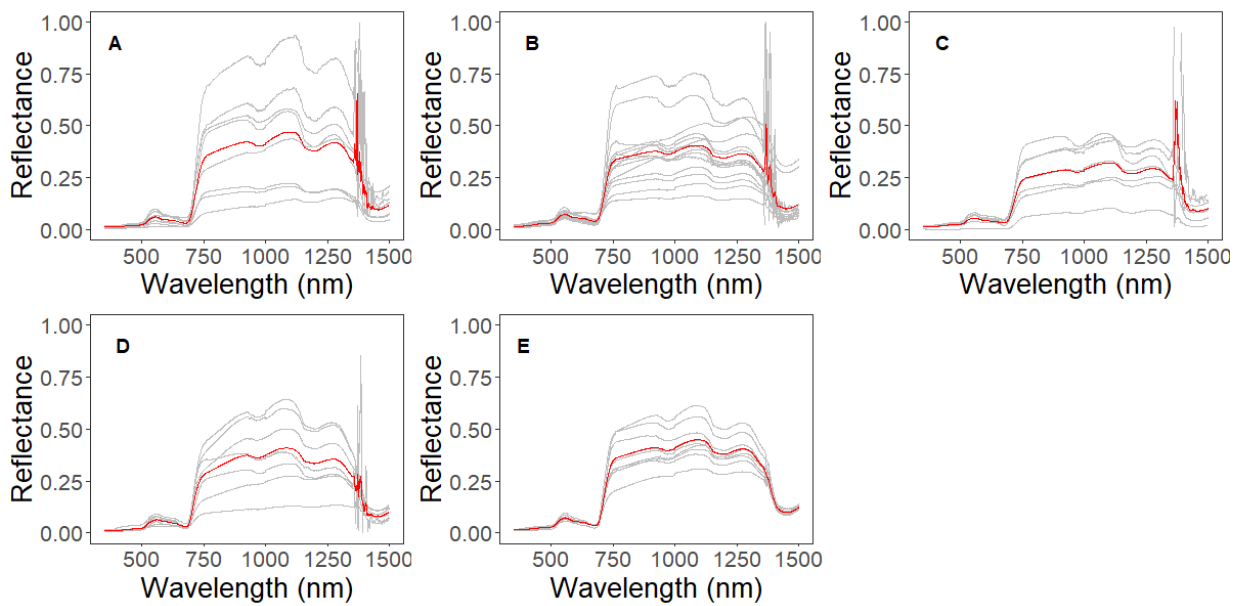
Figure 5. Spectral signatures of plant communities across Bonsai wetland, Fortress Mountain, Alberta, Canada on August 24 where grey lines are individual spectra and red lines are average spectra: a) fir trees; b) ground vegetation; c) larch trees; d) moss; and e) shrubs.
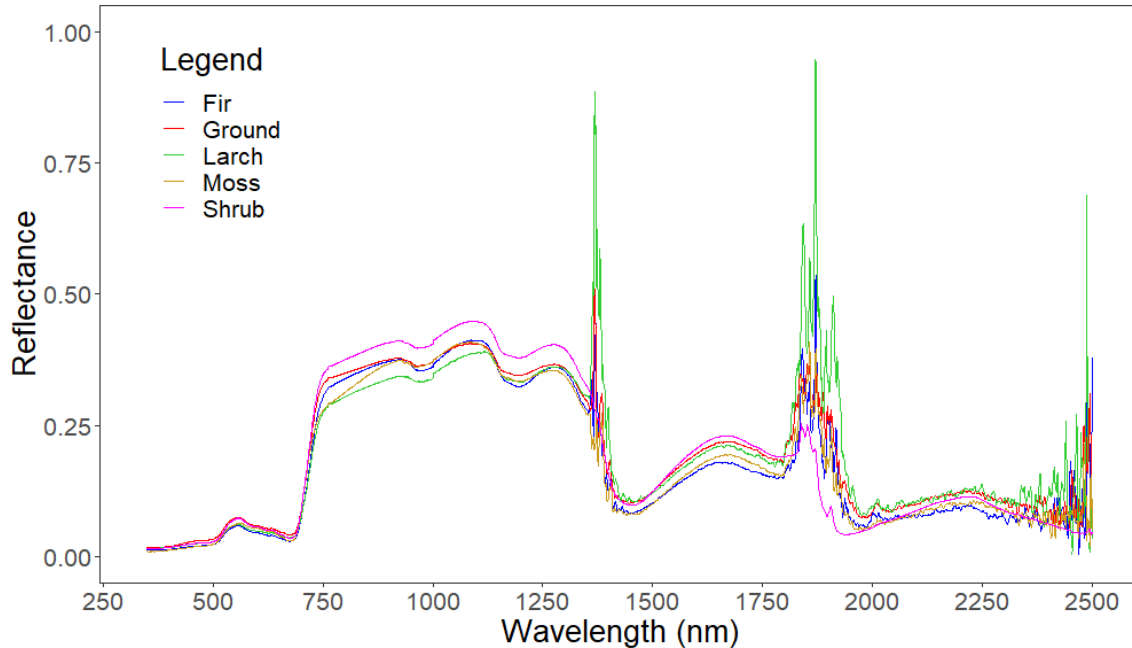
Figure 6. Average spectral signatures of plant communities across Bonsai wetland, Fortress Mountain, Alberta, Canada on August 24, 2020.

Table 3 shows NDVI, WI, and calculated PWS of each vegetation plot. NDVI scores averaged 0.76 and ranged from 0.57 – 0.86. Larch and mixed ground vegetation communities had the lowest NDVI score, while fir and moss communities had the highest. WI scores varied less, with an average of 1.06 and a range of 0.97 – 1.02. The shrub community had the lowest WI score, while fir and moss communities had the highest WI score. The PWS score had an average of 1.36 and ranged from 1.23 – 1.59. Larch and ground vegetation communities had the highest PWS scores, while the fir and the moss communities had the lowest PWS scores.

Linear regression was used to analyze the relationships between 18 plant community ET and NDVI, WI and PWS scores. Spectral indices are calculated using spectral signatures collected on August 24. As leaves within vegetation plots began to drop throughout the study period, vegetation health indices are only compared to the ET results on August 24, except for moss ET as there were not enough moss samples collected for statistical analysis. NDVI had strong relationship ($R^2 > 0.7$) with fir and shrub ET and very weak relationship ($R^2 < 0.01$) with all other plant community ET. WI had strong relationship ($R^2 > 0.7$) with fir, larch, and shrub ET and weak relationships ($R^2 < 0.2$) with all other plant community ET. PWS had strong relationships ($R^2 > 0.8$) with fir ET and moderate to weak relationship ($R^2 \leq 0.4$) with all other plant community ET. All

spectral indices were not statistically significant ($p>0.05$) with ET results of any plant communities, except for the WI results with shrub community ET.

Table 3. NDVI, WI, and PWS Scores for each plant community plot at Bonsai wetland, Fortress Mountain, Alberta, Canada based on spectral signatures taken on August 24, 2020.

Plant Community	Plot	NDVI	WI	PWS
Fir	3	0.86	1.05	1.23
	15	0.86	1.05	1.23
	16	0.76	1.00	1.33
Ground Vegetation	6	0.64	1.01	1.58
	8	0.64	1.01	1.59
	9	0.83	1.04	1.25
	10	0.58	1.01	1.75
	11	0.70	1.02	1.46
	12	0.76	1.03	1.37
Larch	1	0.68	1.03	1.50
	2	0.74	1.03	1.38
	4	0.74	1.00	1.35
Moss	17	0.85	1.05	1.23
	18	0.82	1.02	1.24
Shrub	5	0.71	0.97	1.37
	7	0.79	0.99	1.25
	13	0.78	1.00	1.28
	14	0.79	1.02	1.28

3.3 Albedo

The NTB albedo model performed well in predicting shortwave albedo using the narrowband albedo values of 56 reference spectra ($p<0.05$, $R^2=0.99$, RSE= 0.008). The green, red, and near-infrared bands had high statistical significance ($p<0.05$) and the red-edge band had lower statistical significance ($p=0.056$) for the calculation of shortwave albedo. However, the Red-Edge band was included in the albedo calculation, because the fit of the overall model improved when the Red-Edge band albedo was included. The shortwave albedo from the NTB model in Equation 10 is shown in Figure 7.
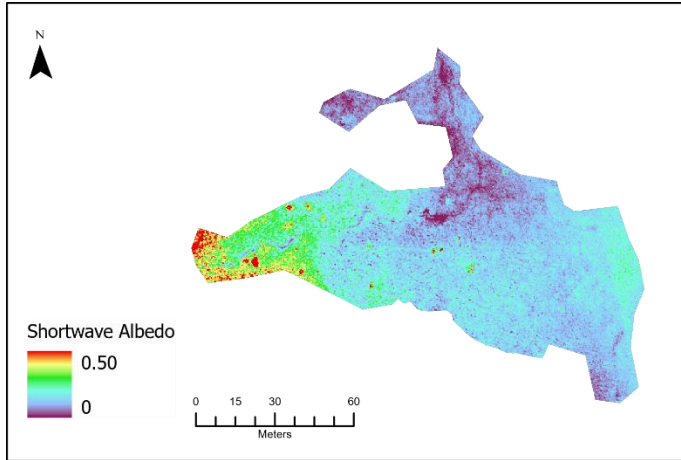
Figure 7. Shortwave albedo derived from NTB model of Bonsai, Fortress Mountain, Alberta on August 26, 2020.

3.4 Canopy Height and Leaf Area Index

Plant height estimated by the CHM showed moderate relationship ($p<0.05$, $R^2=0.34$, $n=18$) and low error (MAE=1.03) with ground-measured LAI samples at the vegetation plots (Figure 8). As shown in Figure 9-A, the CHM plant height results varied from $0 – 3.5$ m, where pixels with a value of 0 were classified as ground pixels in the CHM. The derived LAI (Figure 9-B) varied from $0 – 26$ and over 93% of the study area had a LAI ≤ 6. Most of the study area (54%) had a LAI ≤ 2, containing mixed ground vegetation. Most shrubs and trees had a LAI of $2 – 4$ (30%) or $4 – 6$ (9%) (Figure 9-B). The pixels with the highest LAI (>12) contained tall trees, dense shrubs, and rocks.
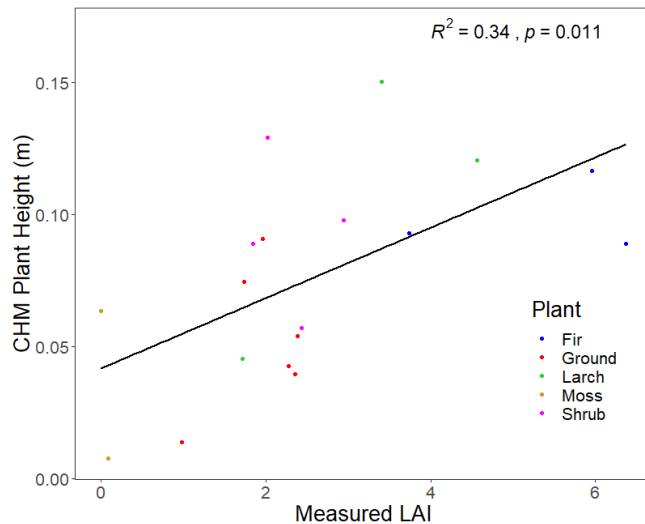
Figure 8. Relationship between CHM plant height with measured LAI of plant community groups at Bonsai, Fortress Mountain Alberta.

43
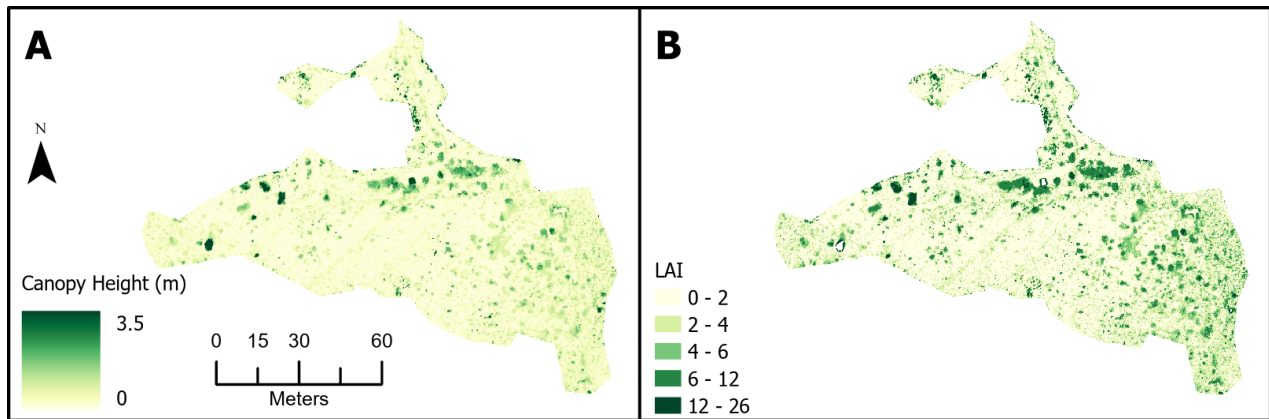
Figure 9. CHM results from LiDAR imagery taken at Bonsai, Fortress Mountain, Alberta on August 26, 2020 of a) plant height; and b) LAI.

3.5 Evapotranspiration

3.5.1 Chamber Evapotranspiration

Total hourly ET between plant communities is shown in Figure 10-A and normalized hourly ET between plant communities in Figure 10-B. Although shading conditions varied throughout the day, there was consistently 14 hours of daylight (PPFD > 0 μmol m^{-2} s^{-1}) recorded at the meteorological tower. Therefore, hourly ET was multiplied by 14 hours of daylight to estimate the daily ET. Total hourly ET at vegetation plots taken during sunlight (PPFD > 825 μmol m^{-2} s^{-1}) had an average of 0.17 mm and ranged from 0.09 – 0.42 mm on August 24, 0.06 – 0.50 mm on August 26, and 0.05 – 0.22 mm on September 5 (Figure 10). Total hourly ET measurements taken during hillshade (PPFD < 480 μmol m^{-2} s^{-1}) had an average of 0.07 mm and ranged from 0.01 – 0.14 mm on August 31 and 0.01 – 0.20 mm on September 2. Average sunlit ET measurements decreased from 0.21 mm hr^{-1} to 0.11 mm hr^{-1}, while shaded ET averages stayed at 0.06 - 0.07 mm hr^{-1} throughout the study period. The average total ET for all plant communities throughout the study period was 0.13 mm hr^{-1} or 1.76 mm day^{-1}.

The shrub and larch communities had the highest total average ET of 0.16 mm hr^{-1} within the study period. The ground vegetation community had a total average ET of 0.11 mm hr^{-1}, the fir tree community had a total average ET of 0.10 mm hr^{-1}, and the moss communities had the lowest total average ET of 0.09 mm hr^{-1}. On sunny days, shrub and larch tree communities had the highest total ET, while moss and fir tree communities had the lowest total ET, except for September 5, when the fir tree community ET was one of the highest. On shaded days, fir and

larch tree communities had the highest total ET of all plant community groups, whereas moss and ground vegetation community groups had the lowest total ET.
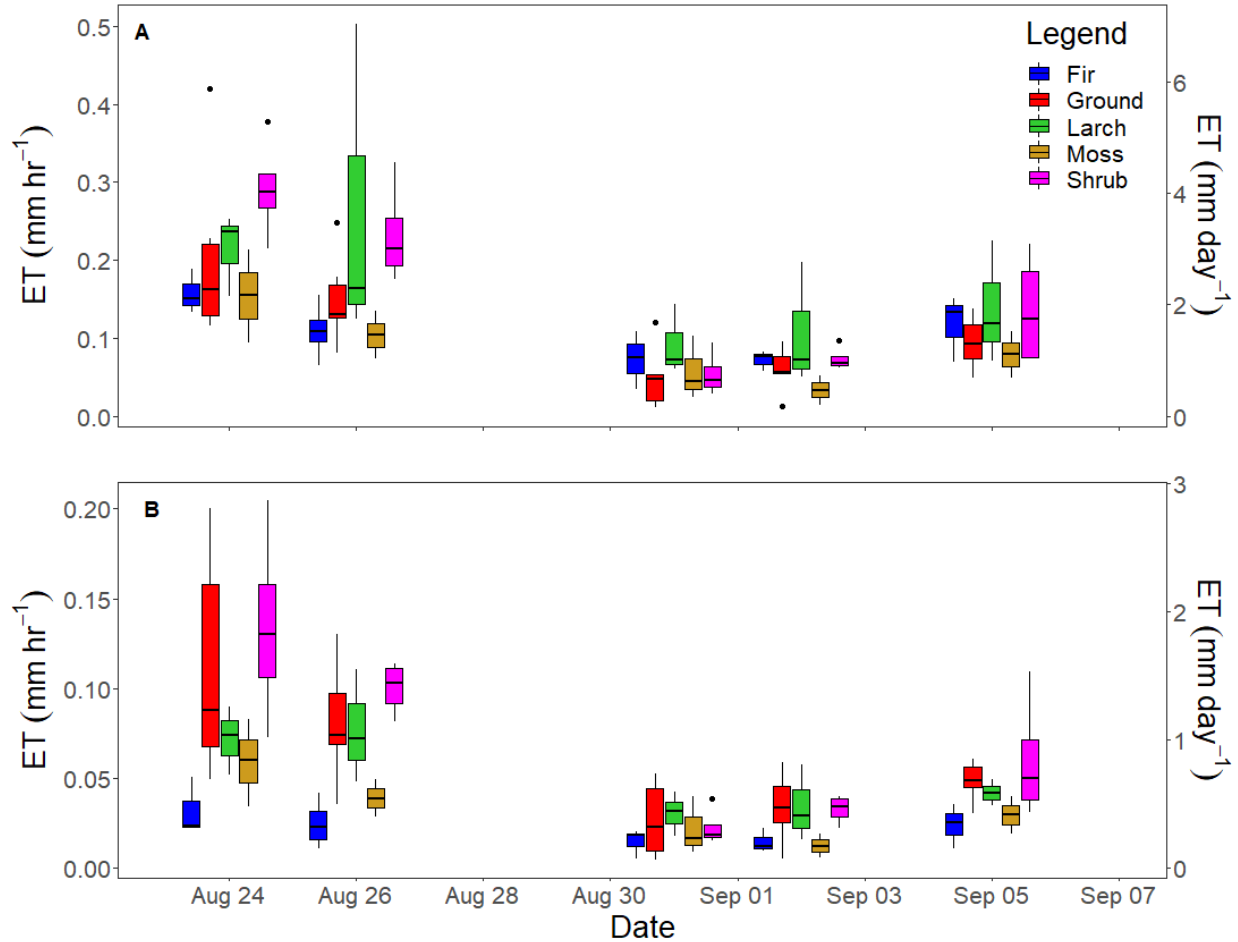
Figure 10. a) Total hourly and daily evapotranspiration of plant communities from August 24 to September 5, 2020; b) Normalized hourly and daily evapotranspiration of plant communities from August 24 to September 5, 2020.

As described in Table 1, plant communities varied by LAI, with fir and larch tree communities having the highest, ground vegetation and shrub communities having the lowest, and moss communities having an approximated LAI. Therefore, plant community ET results were also normalized by LAI (Figure 10-B). The plant community with the highest average normalized ET during sunlit measurements were shrubs. During shaded measurements, the highest average normalized ET varied between the shrub, larch, and ground vegetation communities. Fir tree communities had the lowest average normalized ET in both sunlit and shaded measurements, apart

from the shaded measurement on September 2, when moss plots had the lowest average normalized ET.

Sunlit and shaded measurements were separated by plant community group (Figure 11) and all plant communities showed a statistically significant difference (p<0.05) between sunlit and shaded measurements using the Whitney-Mann-Wilcoxon test. To test the statistical difference between the plant community groups, sunlit and shaded observations were tested separately. As the datasets did not follow a normal distribution, the Kruskal Wallis test was used and showed that plant communities were statistically different (Figure 11) during sunlit measurements ($H > 9.488$; $p < 0.001$) but not during shaded measurements ($H > 6.242$; $p > 0.10$). Therefore, a post-hoc Mann-Whitney-Wilcoxon test was performed for comparisons of plant community groups in the sunlit measurement dataset only (Table 4) and showed that moss communities were significantly different (p<0.05) from ground vegetation and shrub communities in normalized ET during sunlit measurements. Ground vegetation community was also statistically different from the fir tree community ($p < 0.00005$). Shrub community statistically different from moss ($p < 0.05$) and fir tree communities ($p < 0.0005$). While the fir tree community differed significantly from all communities except for moss, and the larch tree community only showed a significant difference with the fir tree community.
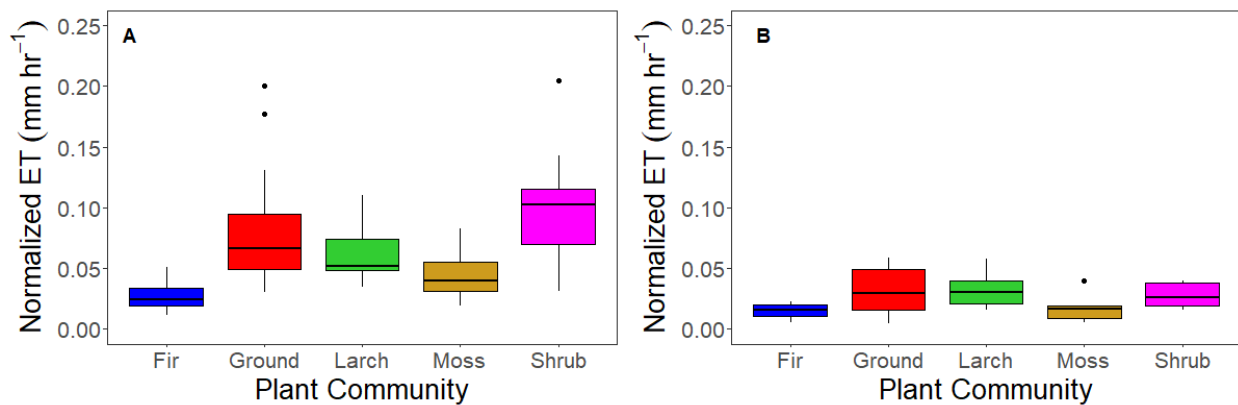
Figure 11. Plant community ET at Bonsai wetland, Fortress Mountain, Alberta during a) sunlit measurements on August 24, 26 and September 5; and b) shaded measurements on August 31 and September 2.

Table 4. Mann-Whitney-Wilcoxon test for normalized plant community ET comparisons at Bonsai wetland, Fortress Mountain, Alberta, Canada.

("ns" not statistically significant.
* <0.05
** <0.001
*** <0.0001)

	Moss (*n=2*)	Ground (*n=6*)	Shrub (*n=4*)	Fir Tree (*n=3*)	Larch Tree (*n=3*)
Ground	*				
Shrub	*	ns			
Fir Tree	ns	***	***		
Larch Tree	ns	ns	ns	**	

To test the influence of local climate on total ET (Figure 10-A), T_s, VWC, and net radiation were analyzed using a multiple linear regression model. T_s and VWC (Table 2) was taken at the plot level and net radiation (Figure 4-B) at the ecosystem level. As net radiation measurements were recorded every half hour, net radiation during each ET measurement was estimated using linear interpolation with the two closest recordings. Climatic variables showed moderate relationships (R^2=0.41) with ET rates across all plots. Results show that net radiation had the most statistically significant (p<0.05) positive influence on ET, while surface temperature had a lower statistical significance (p=0.10), and volumetric water content did not have a statistically significant influence (p=0.23).

Distance to the talus slope and the creek were tested for significance to the normalized ET using linear regression. The distance to the creek had a statistically significant (p<0.05) negative relationship with the normalized ET results but showed a weak relationship (R^2=0.23). Distance to the talus slope was not statistically significant (p=0.17) and showed a weak relationship (R^2=0.12) with normalized ET results.

3.5.2 METRIC Evapotranspiration

The METRIC model uses ASCE standardized Penman-Monteith equation for short crop ET to calculate ET_r at the location of hot and cold pixels (Allen et al., 2007). Table 5 details the parameters obtained from the meteorological tower and imagery-derived R_n and G at the hot and

cold pixel location for ET_r calculations. Energy balance parameters used in the final iteration of METRIC are displayed in Figure 12. METRIC ET results calibrated using ET_r (Figure 13) demonstrate that ET is highest near the talus slope and on the west side of the meadow. ET is the lowest on the north side of the creek where the water drains into Bonsai Lake and on the east side of the meadow where one creek had dried up by the beginning of the study period. The pixels with negative ET values were classified as rocks using the RGB imagery.

Table 5. Hourly reference evapotranspiration results at the cold pixel and hot pixel.

Parameter	Cold Pixel	Hot Pixel
Short crop ET, ET_{os} (mm h^{-1})	0.435	0.433
Net radiation, R_n (MJ)	1.645	1.742
Soil heat flux, G (MJ)	0.067	0.171
Air temperature, T_a (°C)	14.4	14.4
Wind speed, u_2 (m s^{-1})	1.934	1.934
Saturation vapor pressure, e_s (kPa)	1.313	1.313
Mean actual vapor pressure, e_a (kPa)	0.458	0.458
Slope of e_s-T_a curve, Δ (kPa °C^{-1})	0.106	0.106
Psychrometric constant, γ (kPa °C^{-1})	0.052	0.053
Hourly numerator for short crops, C_n (K mm s^3 Mg^{-1} h^{-1})	37	37
Hourly denominator for short crops, Cd (s m^{-1})	0.24	0.24
Reference ET correction	0.50	0.05
ET_r (mm h^{-1})	0.228	0.022
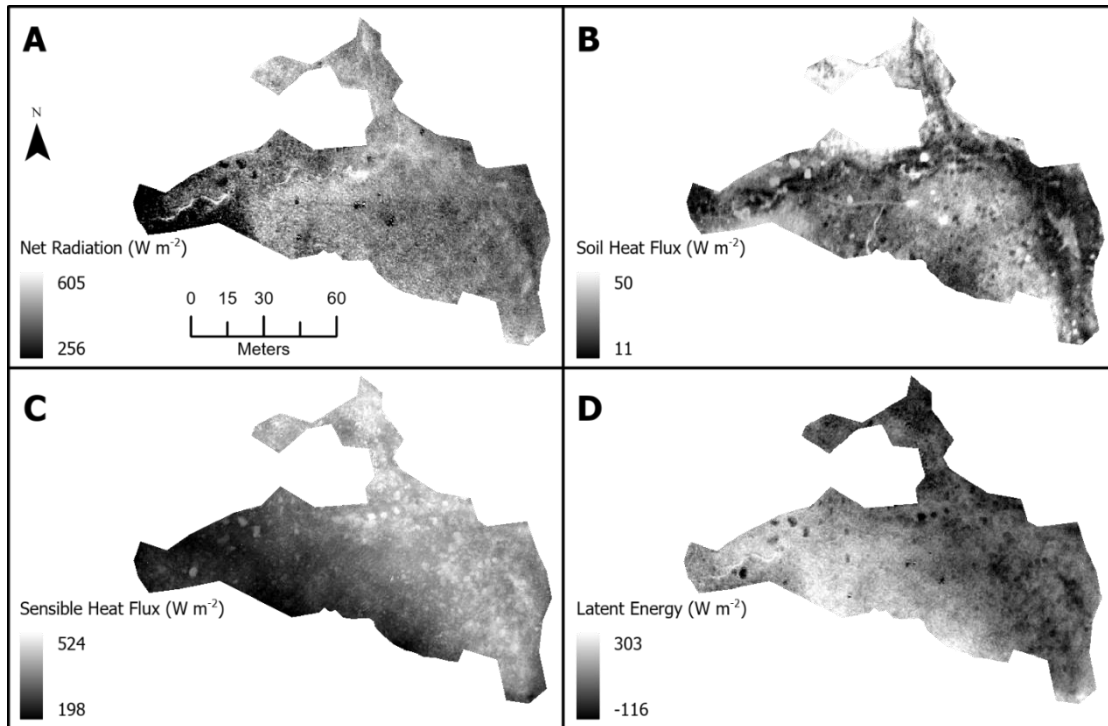
Figure 12. METRIC model outputs of Bonsai, Fortress Mountain, Alberta on August 26, 2020. Maps of: a) net radiation; b) soil heat flux; c) sensible heat flux; and d) latent energy.
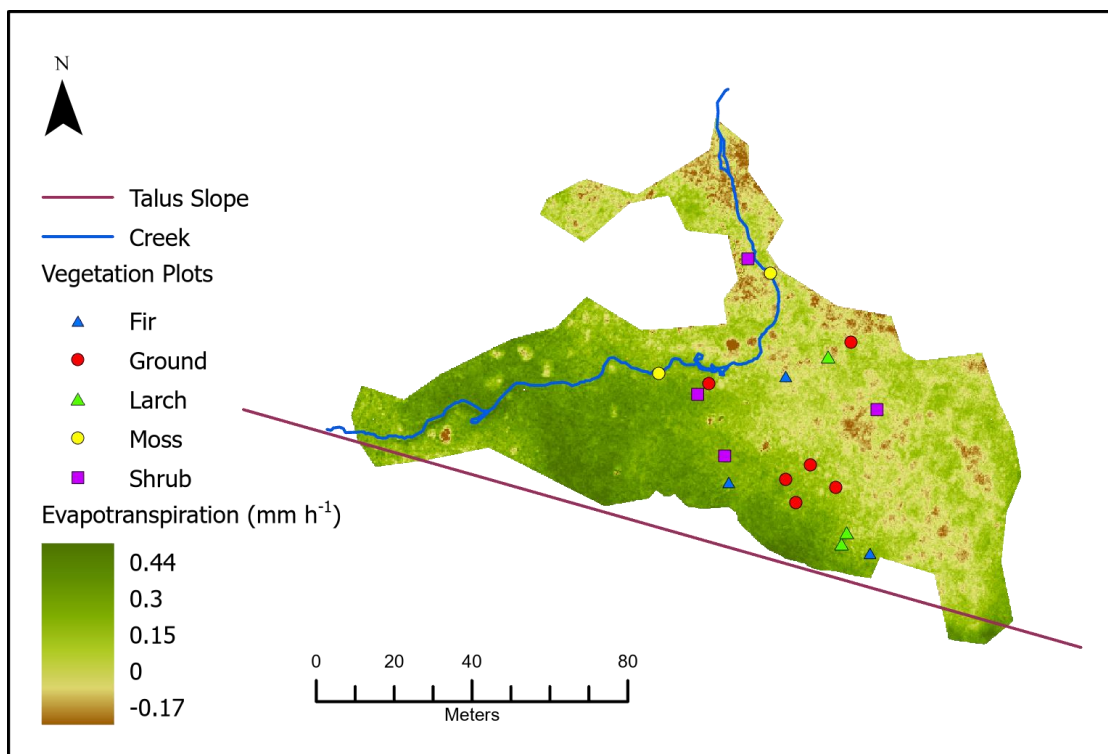
Figure 13. METRIC model evapotranspiration at Bonsai, Fortress Mountain, Alberta on August 26, 2020.

Dynamic closed chamber ET results used to assess the accuracy of METRIC results at the location of each vegetation plot were collected on an hourly and daily timescale (Table 6). Hourly chamber ET was collected on August 26 during the thermal imagery flight. Hourly METRIC values underestimated most of the shrub ET, overestimated moss ET, and had mixed results for fir, larch, and ground plots (Table 6). Overall, METRIC hourly ET results agreed well with field measurements, with an R^2 of 0.79, RMSE of 0.09 mm h^{-1}, mean bias (MBE) of 0.002 mm h^{-1}, and mean relative difference (MRD) of 47% (Figure 14-A). Average hourly ET for each plant community was relatively similar ($\pm$ 0.06 mm h^{-1}) between METRIC and chamber measurements, but still overestimated fir, ground, and moss communities and underestimated larch and shrub communities. Average hourly chamber ET and METRIC ET of plant communities agreed well with an R^2 of 0.91, RMSE of 0.05 mm h^{-1}, and MBE of 0.002 mm h^{-1}, but had a high relative difference of 114% (Figure 14-C).

Total average chamber ET is the average of all daily chamber ET measurements in the study period (Table 6). Daily ET values in both chamber and METRIC datasets were estimated by multiplying the hourly ET by 14 hours of daylight (PPFD > 0) recorded at the meteorological tower. When comparing daily METRIC values to the daily average chamber ET for the study period, larch ET and most the ground ET plots were overestimated and the fir, shrub, and moss ET values had mixed results. Overall, daily ET results agreed well with an R^2 of 0.82, RMSE of 0.95 mm day^{-1}, MBE of 0.25 mm day^{-1}, and MRD of 49% (Figure 14-B). The average daily ET for plant communities overestimated all communities, except for shrubs. However, the average daily ET still agreed well with an R^2 of 0.97, RMSE of 0.37 mm day^{-1}, and MBE of 0.20 mm day^{-1}, but had a high relative difference of 115% (Figure 14-D).

Table 6. Plant community evapotranspiration hourly estimates on August 26, 2020 and daily average estimates from the study period from dynamic closed chamber measurements and METRIC model results at Bonsai, Fortress Mountain, Alberta.

Plot	Plant Community	Chamber ET on August 26 (mm hr^{-1})	Chamber ET Total Average (mm day^{-1})	METRIC ET (mm hr^{-1})	METRIC ET (mm day^{-1})
3	Fir	0.06	1.45	0.16	1.64
15	Fir	0.11	1.23	0.09	0.52
16	Fir	0.13	1.71	0.21	2.62
Avg.	**Fir**	**0.10 (σ=0.01)**	**1.46 (σ=0.20)**	**0.15 (σ=0.05)**	**1.59 (σ=1.05)**
1	Larch	0.16	2.21	0.20	2.34
2	Larch	0.50	3.30	0.24	3.58
4	Larch	0.12	1.32	0.16	1.51
Avg.	**Larch**	**0.26 (σ=0.17)**	**2.28 (σ=0.81)**	**0.20 (σ=0.03)**	**2.48 (σ=0.85)**
5	Shrub	0.18	2.03	0.13	1.06
7	Shrub	0.20	2.10	0.12	0.88
13	Shrub	0.23	2.35	0.23	3.29
14	Shrub	0.32	2.32	0.20	2.44
Avg.	**Shrub**	**0.23 (σ=0.05)**	**2.20 (σ=0.14)**	**0.17 (σ=0.05)**	**1.92 (σ=1.00)**
6	Ground	0.13	1.12	0.18	2.06
8	Ground	0.13	1.34	0.17	1.78
9	Ground	0.25	2.56	0.14	1.29
10	Ground	0.08	1.32	0.16	1.61
11	Ground	0.13	1.48	0.23	3.29
12	Ground	0.18	1.47	0.24	3.44
Avg.	**Ground**	**0.15 (σ=0.05)**	**1.55 (σ=0.47)**	**0.19 (σ=0.04)**	**2.24 (σ=0.83)**
17	Moss	0.07	1.18	0.11	0.69
18	Moss	0.13	1.18	0.19	2.23
Avg.	**Moss**	**0.10 (σ=0.03)**	**1.18 (σ=0.00)**	**0.15 (σ=0.04)**	**1.46 (σ=0.77)**
Avg.	**All**	**0.17 (σ=0.07)**	**1.73 (σ=0.43)**	**0.17 (σ=0.02)**	**1.94 (σ=0.38)**
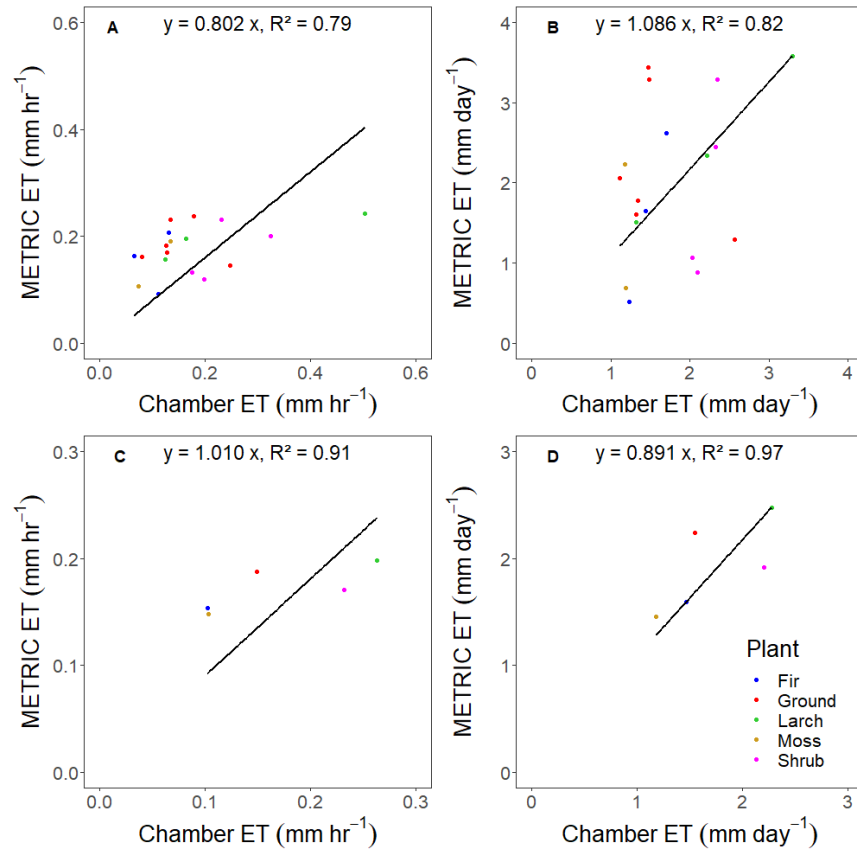
Figure 14. Comparison between METRIC model and chamber measurements at Bonsai, Fortress Mountain, Alberta of: a) hourly evapotranspiration; b) daily evapotranspiration; c) average hourly evapotranspiration; and d) average daily evapotranspiration.

Hourly METRIC ET accuracy was high among plant communities on August 26 with $R^2 \geq$ 0.84 and MBE of ±0.07 mm h^{-1} for all communities except moss, which not analyzed using R^2 or RMSE due to only having 2 chamber measurements. The shrub community had the best fit (R^2=0.95) and the lowest relative difference (MRD=26%). Although the larch community also had a low relative difference (MRD=33%), they had the highest amount of error (RMSE=0.15) and bias (MBE=-0.07). The fir community had the lowest amount of error (RMSE=0.07) and low bias (MBE=0.05) but had the highest relative difference (MRD=76%). Ground and moss communities had the lowest bias (MBE=0.04) and moderate relative differences (MRD=44-55%).

Daily METRIC ET agreed well with the averaged chamber ET of taller vegetation, such as fir, larch, and shrubs ($R^2 \geq$0.83) and was in moderate agreement with the ground vegetation (R^2=0.75) (Table 7). The tree plots had the lowest error (RMSE≤0.68) and bias (MBE≤0.20). The larch ET also had the lowest relative difference (MRD=10%), while fir ET had a moderate relative

difference (MRD=42%). Although shrub ET fit well (R^2=0.83) and had low relative difference (MRD=38%) and bias (MBE=-0.28), the results had a high amount of error (RMSE=0.91). Ground vegetation ET estimates had the highest amount of error (RMSE=1.29), bias (MBE=0.69), and relative difference (MRD=74%). Moss ET had a low bias (MBE=0.27) and the highest relative difference (MRD=65%). METRIC results had the best fit with plant community averages on hourly (R^2=0.91) and daily (R^2=0.97) timescales.

Table 7. Determination coefficient, root mean squared error, mean bias and mean relative difference statistics for hourly and daily plant community METRIC evapotranspiration at Bonsai, Fortress Mountain, Alberta.

Plant Community	R^2		RMSE		MBE		MRD (%)	
	Hourly	Daily	Hourly	Daily	Hourly	Daily	Hourly	Daily
All	0.79	0.82	0.09	0.95	0.00	0.25	47.10	48.81
Average	0.91	0.97	0.05	0.37	0.00	0.20	113.83	114.58
Fir (*n*=3)	0.87	0.87	0.07	0.68	0.05	0.13	76.27	41.80
Larch (*n*=3)	0.84	1.00	0.15	0.21	-0.07	0.20	32.78	9.55
Shrub (*n*=4)	0.95	0.83	0.08	0.91	-0.06	-0.28	25.85	37.64
Ground (*n*=6)	0.85	0.75	0.08	1.29	0.04	0.69	54.93	73.96
Moss (*n*=2)	n/a		n/a		0.04	0.27	43.80	65.11

Spatial variability of METRIC ET was assessed using Local Moran's I and LISA cluster analysis. Moran's I for the METRIC ET was 0.93, indicating high spatial clustering. Figure 15 shows clustering of both high (High-High) and low (Low-Low) ET values and very few outliers (Low-High, High-Low) of statistical significance ($p \leq 0.05$). The LISA map (Figure 16) displays the locations of these clusters and outliers. The majority of the high ET clusters are in the western side of the meadow, whereas low ET clusters are concentrated on the north and eastern side of the meadow. There are a few low ET clusters on the western part of the meadow containing pixels that were classified as rocks using the RGB imagery. Both High-Low and Low-High outliers were spread throughout the meadow.
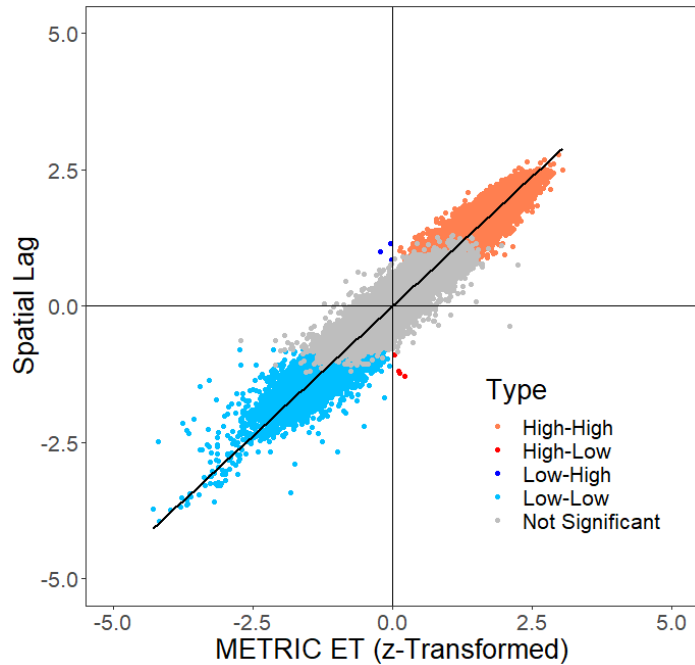
Figure 15. Moran's I scatterplot of METRIC evapotranspiration results indicating areas of positive spatial autocorrelation or clusters (High-High and Low-Low) and negative spatial autocorrelation or outliers (High-Low and Low-High).
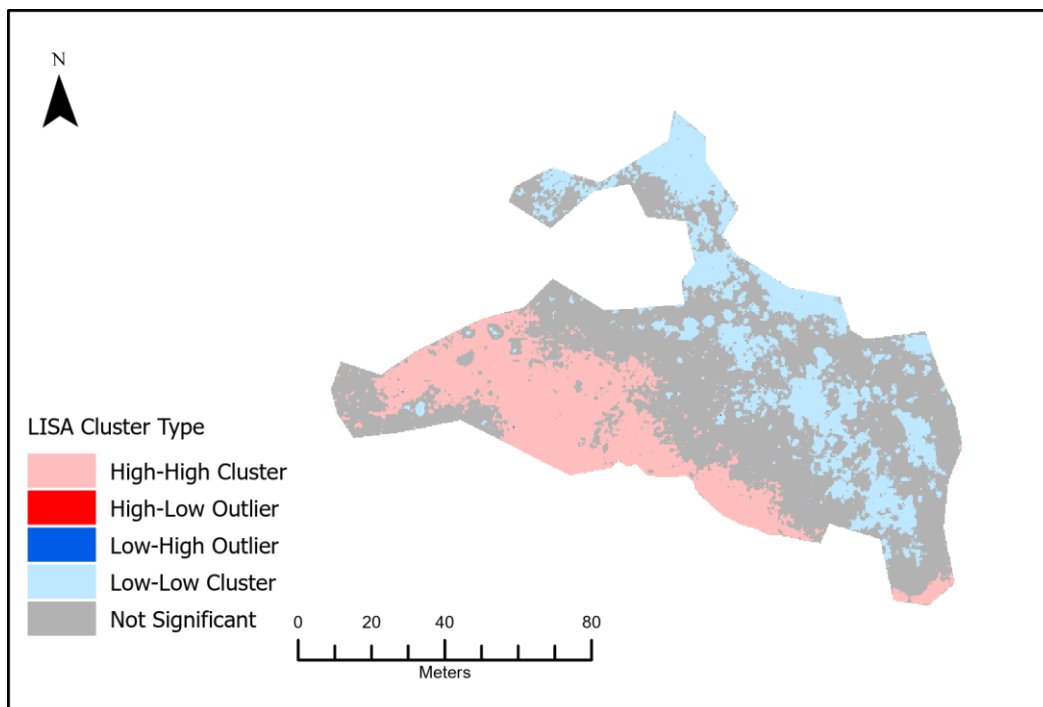

Figure 16. LISA cluster and outlier analysis map of METRIC evapotranspiration results at Bonsai, Fortress Mountain, Alberta on August 26, 2020.

Chapter 4: Discussion

4.1 Evapotranspiration Controls

Hourly ET rates of plant communities at Bonsai meadow are comparable to those found in other studies of similar plant species (McNaughton & Jarvis, 1983; Ohta et al., 2008). Fir tree ET averaged 0.10 mm h^{-1}, which is comparable to the daily average of 0.12 mm h^{-1} in a mature fir forest in Quebec on August 20 (McCaughey, 1978). The average rate of ET from larch tree plots of 0.16 mm h^{-1} is higher than the values of 0.06 – 0.10 mm h^{-1} in larch forests in Siberia from April to September (Ohta et al., 2008) and approximately 0.10 mm h^{-1} in boreal larch forests in Northeast China (Liu et al., 2020). Shrub plots had a total average ET of 0.14 mm h^{-1}, while the ground vegetation plots had an average ET of 0.11 mm h^{-1}. These values are comparable to a study at an alpine region in Northern China from August 21 to September 14, where shrub community ET averaged 0.09 mm h^{-1} and the alpine meadow had an average ET of 0.10 mm h^{-1} (Li et al., 2021). Although moss communities had the lowest average total ET at 0.08 mm h^{-1}, it is higher than average moss ET of 0.03 mm h^{-1} measured in another study by Raz-Yaseef et al. (2017) using chamber measurements in Alaska in July. Hourly ET rates are comparable to other alpine ecosystems or species, however, some dissimilarities between ET rates in each study could be attributed to differences in LAI, local climate, available moisture or individual species (Brümmer et al., 2012; Hopkins, 2006).

Multiple linear regression of climatic controls on chamber ET show that net radiation had the most significant positive relationship with ET throughout the study period, while surface temperature fell just short of statistical significance and VWC did not have a significant influence. These results are consistent with previous studies that found radiation and temperature as the driving forces for ET in similar plant communities in alpine ecosystems (Brümmer et al., 2012; Jarvis & McNaughton, 1986; Li et al., 2021; Liu et al., 2020). Recent literature suggests that ET is only influenced by VWC in alpine ecosystems that are water limited and undergoing water stress due to lack of precipitation or low VWC (Calanca et al., 2006; Gu et al., 2005; van den Bergh et al., 2013; Zhang et al., 2016). Based on the VWC measurements at the meteorological tower, PWS and WI scores, the vegetation plots at Bonsai meadow were not experiencing water stress. Therefore, the results of this study are consistent with the literature with ET mainly controlled by net radiation and surface temperature when plant water stress is low.

Chamber ET had weak relationships with vegetation health indices, such as NDVI, WI, and PWS, but had a strong relationship with plant community type. Similarly, the spatial trend of high NDVI from the multispectral imagery did not overlap with clusters of high ET in the METRIC results. Vegetation indices identified fir and moss communities as the healthiest, densest, and greenest vegetation plots with the highest water content and the least water stress (lowest PWS; highest average NDVI and WI scores). However, ET rates of the fir plots were among the lowest in the dataset. Furthermore, shrub and larch plots had the highest ET, yet were among the least healthy and most water stressed plots. As deciduous vegetation has thinner cuticles than evergreen vegetation, shrub leaves and larch needles are susceptible to water loss (Hopkins, 2006). These results are in contrast with studies that suggest NDVI has a significant positive relationship with ET in alpine environments (Bai et al., 2019; Pei et al., 2017). However, Pape & Löffler (2016) found that net primary productivity had weak relationships with NDVI and strong relationships with vegetation type in an alpine environment, although no direct comparisons are made with ET. Given the differences in plant physiology between deciduous broadleaf and evergreen needle-leaf species (Hopkins, 2006), results here agree with Pape & Löffler (2016) where plant community type could have a bigger influence on plant function than NDVI, especially when plants are not undergoing water stress. Further, Peñuelas et al. (1993) suggests that structural and physiological differences in plant species affect the reflectance in near-infrared wavelengths used in NDVI, WI, and PWS indices. Therefore, the results of spectral indices could also be affected by vegetation type and spectral mixing in each plot, as vegetation plots contained a variety of flowers, leaves, and soil particles which have varying spectral response.

Plants have reduced ET rates in shaded conditions, as temperatures decrease, photosynthesis stops, and stomata close (Hopkins, 2006). However, the degree of shade can vary spatially across a site and plant communities vary in sensitivity to shade due to physiology (Jarvis & McNaughton, 1986; Reich et al., 1998; Sanchez et al., 2016). Although all plant communities had statistically significant differences between sunlit and shaded measurements, fir tree communities had the most similar values across all measurement days. As an evergreen conifer, the needle-leaves on fir trees survive winters and can last 8 to 13 years before dropping and starting another regrowth cycle (Zon, 1914). The needle-leaves have a lower surface area to volume ratio than broadleaves, are covered by thick cuticles, and have sunken stomata to prevent water loss in colder months (Hopkins, 2006). These adaptations reduce water loss through transpiration during

sunny conditions and water loss through evaporation in shady conditions (Hopkins, 2006; Reich et al., 1998; Sanchez et al., 2016). Fir tree communities also had the highest LAI, with dense clusters of needle-leaves. Clustering of needle-leaves can also limit ET with a reduction in wind speed against individual leaves, further reducing boundary-layer conductance at the leaf level (Jarvis & McNaughton, 1986). Results of this study show that broadleaf species, such as the shrub and ground vegetation plots, are more sensitive to shade than conifers. Broadleaf species have a higher surface area to volume ratio, thinner cuticles, shallower stomatal openings, and require a higher total PPFD than conifer species for photosynthesis (Hopkins, 2006; Sanchez et al., 2016). Therefore, results of this study concur with the literature, which states that broadleaf species are more sensitive to shading and cloud cover than conifers (Sanchez et al., 2016). As broadleaf species are predicted to move upslope in alpine regions (He et al., 2015; Niu et al., 2019), competitive replacement of conifer species with broadleaf species may increase ET fluctuations due to horizon shading and cloud cover.

As deciduous conifers, larch trees have a distinct hydrological function from evergreen conifers (Liu et al., 2020). At the end of the study period, the larch tree needles began to turn yellow and eventually dropped after a snow event on September 7. The larch tree communities had higher total average ET during sunlit measurements and lower total average ET during shaded measurements than fir tree communities. Larch trees have greater net photosynthesis but are less shade tolerant than most evergreen conifers (Reich et al. 1998). Moss communities also showed a significant difference in evaporation between sunny and shady measurements as mosses do not have stomata and roots to control water loss, evaporation is mainly influenced by radiation, wind and water supply (Heijmans et al., 2004).

4.2 Spatial Variability of Evapotranspiration

The spatial patterns of average chamber ET at Bonsai meadow are consistent with alpine literature, in which spatial ET is controlled by local climate, moisture and vegetation patterns influenced by elevation (Christensen et al., 2008; Körner, 2007; Menzel & Lang, 1998; van den Bergh et al., 2013). This study shows that average chamber ET increases with soil moisture and proximity to the creek. Although proximity to the talus slope did not have a significant direct relationship with chamber ET, there were significantly moderate relationships with controls on ET, such as soil moisture. Hrach et al. (2021) also found that there is a spatial pattern of decreasing soil moisture from the distance of the stream to the headwall due to slope, heterogeneous hydraulic conductivity

and permeability. Heterogenous soil distribution and slope causes varying hydraulic conductivity and permeability at Bonsai meadow, where groundwater flows from West to East along the flow of the creek towards the stream confluence and South to North from the talus slope to Bonsai Lake (Christensen, 2017; Hrach et al., 2021). Similarly, results in other studies of spatial ET (Condon et al., 2020; Nachabe et al., 2005) show that proximity to surface water and shallow groundwater connections can prevent plant water stress and evaporative stress. Vegetation also impacts soil moisture variability due to variable root water uptake rates, as trees have deeper rooting depths than other plants (Tromp-van Meerveld & McDonnell, 2006). Based on the physiological differences between plant communities described in Section 4.1, this study further illustrates that spatial difference in chamber ET is likely attributed to vegetation type and their physiological response to lateral soil moisture distribution.

METRIC ET showed clusters of high ET in the Southern and Western sections and clusters of low ET along the Northern and Eastern sections of the meadow. The clusters of high ET resemble a similar pattern to the chamber results, where high ET follows the source of groundwater flow paths measured by Christensen (2017). On the Eastern section of the meadow from South to North, there is a cluster of high ET near the talus slope followed by clusters of low ET surrounding the dried creek. Although many of the low ET clusters coincide with rocks, the spatial pattern also follows the groundwater flow path from South to North (Christensen, 2017). These results suggest that near the end of the growing season when the water source from the headwall decreases due to snowmelt availability, the creek and surrounding vegetation are water limited, leading to lower rates of ET from stomatal closure. Like Menzel & Lang (1998), this study found that evaporation over rocks across the study site was minimal and appeared as negative values in METRIC ET due to calibration of the hot pixel on a bare soil surface cover as opposed to rock. High ET cluster patterns in the Southern and Western parts of the meadow also aligned with groundwater flow paths found in Christensen (2017) but were contrary to the seasonal shading patterns observed by Hrach et al. (2021), where results suggested lower average ET in the sections of the meadow where horizon shading was most prominent. This inconsistency could be due to the timing of image capture, as METRIC ET estimates were based on instantaneous ET calculated from multispectral, thermal, and LiDAR imagery when horizon shading was mostly homogeneous and only affected the Westernmost corner during thermal imagery capture (Figure 1).

58

4.3 Model Applications for Alpine Ecosystems

METRIC ET has a strong relationship ($R^2 \geq 0.75$, n=18) with chamber ET results for all plant communities on hourly and daily timescales. METRIC ET had a slightly higher bias (MBE=0.00 mm h^{-1}, 0.25 mm d^{-1}) and error (RMSE=0.09 mm h^{-1}, 0.95 mm d^{-1}) in comparison to the traditional applications in agricultural environments (He et al., 2017; Tasumi, 2019). However, it is comparable to applications in mountainous areas (MBE=0.03 – 0.06 mm h^{-1}, 0.17 – 0.61 mm d^{-1}, RMSE=0.06 – 0.08 mm h^{-1}, 0.71 – 1.24 mm d^{-1}) using Landsat and MODIS satellite imagery (Acharya & Sharma, 2021; Carrillo-Rojas, Silva, Córdova, Célleri, & Bendix, 2016; Wasti, 2020). While daily METRIC ET had a strong relationship (R^2=0.82) with daily average chamber ET, the model overestimates daily ET by an average of 0.25 mm d^{-1}. METRIC ET was based on thermal imagery captured during sunny conditions, whereas average daily chamber ET was measured in both sunny and shaded conditions. Shaded measurements that reduce average chamber ET are not reflected in METRIC imagery. Similarly, daily METRIC ET does not account for changes in climate and vegetation conditions throughout the study period. Overestimation of ET can occur as a result of misrepresentation of climate conditions at the meteorological station and overestimating the bare soil ET (Dhungel & Barber, 2018; Tasumi, 2019). Although the bare soil condition in this study fits the criteria for the FAO-56 manual (Allen et al., 1998) estimate for all soil types after light (3-10 mm) precipitation events, calculation of the bare soil condition is based on the timeframe of thermal image capture and does not account for climate or vegetation changes at the end of the growing season or the pervious permeability of soils at Bonsai, which could lead to water loss from groundwater flow as opposed to evaporation.

METRIC estimation accuracy varied between plant communities. Taller, deciduous vegetation, such as shrub and larch, were underestimated (MBE=-0.06 – 0.07 mm h^{-1}), while all other vegetation communities were slightly overestimated (MBE=0.04 – 0.05 mm h^{-1}) in hourly METRIC results. METRIC ET is dependent on hot and cold pixel selection for calibration of sensible heat flux, and is traditionally based on $T_{s\ datum}$, NDVI, and albedo (Allen et al., 2013; Castelli et al., 2018; Tasumi, 2019), and does not account for different vegetation types. Moreover, the short crop (0.12 m) ET_r was used instead of the alfalfa-based (0.5 m) ET_r for the cold pixel calculation, as the plant height at the cold pixel was 0.01 m and a majority of the meadow vegetation are under 0.5 m in height, aside from the taller vegetation, which could be the cause of underestimation in tree and shrub communities.

Lower lying vegetation communities, such as ground vegetation and moss, had the highest hourly (44-55%) and daily (65-74%) relative difference between METRIC and chamber estimates. Hourly METRIC estimates for fir communities were an exception with a MRD of 76%. Model accuracy is dependent on accurate calculations of intermediate parameters, such as albedo, momentum roughness length, and LAI (Carrasco-Benavides et al., 2014; Dhungel & Barber, 2018). Albedo measurement from remote sensing is sensitive to different surface covers, angle of the sensor, and availability of sensor bands (Tasumi et al., 2008; Xu et al., 2020). Non-nadir images do not account for the bidirectional reflectance distribution function, which can decrease at-surface reflectance accuracy used for the NTB model (Tasumi et al., 2008). Additionally, the relationship between plant height and LAI varies between needleleaf, broadleaf, crops, and grass (Yuan, Wang, Yin, & Zhan, 2013). CHM-derived plant height had a moderately weak relationship with field-measured LAI (R^2=0.34) and was used for all plant community types, which could lead to inaccurate estimation of LAI and momentum roughness length. Short, dense vegetation, such as shrubs, may have insufficient ground returns due to the penetration abilities of LiDAR, which can misclassify canopy pixels as ground pixels (Luo et al., 2015; Sadro et al., 2007). Difficulty of estimating heterogeneous, short, wetland vegetation height and the associated LAI from LiDAR imagery could be the cause of low estimation accuracy for lower lying vegetation.

Chapter 5: Conclusions

5.1 Conclusions

METRIC applications using high-resolution UAV imagery is effective for estimating the spatial variability of subalpine ecosystems sensitive to climate change. Plant community distribution is responsive to changing climate conditions, contributing to spatial variability of ET in subalpine ecosystems. This study examined the spatial patterns of ET in a subalpine wetland and the sensitivity of this ET to plant community type, climate, and vegetation health. Chamber measurements determined statistically significant differences between plant community ET and response to climate conditions. Accuracy assessments concluded that the METRIC model using UAV imagery had high estimation accuracy for ET and was an effective tool for analyzing spatial variability of ET at an ecosystem-scale.

Community-scale ET was mostly controlled by net radiation and plant type. Although vegetation health indices did not have a significant influence on ET patterns, they illustrate low water stress among all plant communities using the PWS index. Evergreen conifers, such as fir, had the lowest ET per leaf area but were the healthiest, least water stressed, and most shade tolerant plant community due to the sunken stomatal openings, thicker cuticles, and smaller surface area to volume ratio of needle-leaves in comparison to broadleaves. Deciduous conifers, such as larch, had a statistically higher rate of ET per leaf area, but were among the least healthy, most water stressed, and were more sensitive to shade than evergreen conifers. Broadleaf vegetation, such as shrubs and ground vegetation, were the most sensitive to shading conditions, and need higher PPFD for stomatal opening and photosynthesis. Shading dynamics also impacted the rate of evaporation in moss communities, which lack roots and stomata to regulate water loss.

NTB, CHM, and METRIC models were applied using local meteorological data and UAV imagery to produce accurate estimates of ET at a high spatial resolution. Overall, METRIC results were highly correlated with hourly and daily chamber ET. Taller vegetation had the highest estimation accuracy while lower-lying vegetation and moss had the lowest estimation accuracy. Spatial trends of ET were influenced by Ts, connections to groundwater or surface water connections, and plant type. While VWC did not have significant impacts on community-scale ET, it was significantly correlated with the spatial patterns of ET. METRIC ET was highest in the Southern and Western sections and lowest in the Eastern and Northern sections, following the groundwater flow paths observed in a previous study at Bonsai meadow by Christensen (2017).

Average chamber ET also increased with proximity to surface water and average VWC. Variability in hydraulic conductivity and vegetation water uptake rates further affect the soil moisture availability and ET rates. As high-resolution imagery and new classification techniques become more accessible with UAV applications, the potential of METRIC applications for ET estimation could be important for understanding the spatial hydrology of vulnerable ecosystems.

5.2 Project limitations and suggestions for future research

This study was limited by data availability due to time constraints and COVID travel restrictions during the data collection period. Due to a shortened collection period, chamber results are based on the end of the growing season and may not reflect ET values from the peak growing season. Similarly, METRIC results are based on thermal imagery collected near the beginning of the study period on August 26th, when average air temperature, net radiation, and PPFD were at the highest point in the day and are only applicable to spatial ET during those climate conditions. Furthermore, shading dynamics at the site are not captured by imagery used for METRIC. Future studies should consider collecting imagery in diverse climate conditions to capture the variability of spatial ET throughout the growing season.

Difficulties in estimating intermediate parameters from multispectral, thermal, or LiDAR imagery impacted METRIC ET accuracy. LiDAR imagery underestimated LAI and momentum roughness length of short and sparse vegetation. Multispectral imagery and spectroradiometer readings were subject to the mixed pixel problem, in which varying ground cover affected the recorded average spectral signatures. Thermal imagery is also susceptible to estimation accuracy due to increasing sensor temperature during image capture, which overestimates surface temperature over time, affecting the relative temperature within the imagery. Although METRIC uses an internal calibration to minimize biases in absolute temperature, it does not correct discrepancies in relative temperature. The importance of in-situ measurements of intermediate parameters for ground-truthing imagery is emphasized in this study.

METRIC applications in mountainous regions typically use a correction factor described in Allen et al. (2013) to account for the variability in wind and radiation observed between high and low elevations at the landscape-scale. However, the correction factor was excluded in this study due to the small study area with an elevational gradient of less than 7 m and mostly homogeneous radiation at the time of image capture. It is recommended that the correction factor

is used in future applications of METRIC in larger mountainous areas with more heterogeneous climate conditions.

5.3 Significance of research

Alpine regions are vulnerable to species migration from climate change, which can have an important influence on ET at the ecosystem-scale. As temperatures rise and growing seasons become longer, the spatial heterogeneity of alpine vegetation and the associated ET will impact the local water balance. Limited research has been performed on plant community scale ET in subalpine meadows in the CRM. This study quantifies the variability of ET between alpine plant communities and their response to variable climate conditions. As broadleaf species are expected to move upslope in alpine regions and have a higher sensitivity to shading conditions than conifer species, ET variability may increase in these areas. Furthermore, this study demonstrates a workflow for adapting UAV imagery for METRIC model applications at the ecosystem-scale. As UAV imagery becomes more accessible to researchers, the spatial variability of ET can be monitored in vulnerable and inaccessible alpine ecosystems using the METRIC model.

References

Aber, J. S., Pavri, F., & Aber, S. W. (2012). High-latitude and high-altitude wetland case studies. *Wetland Environments: A Global Perspective; John Wiley & Sons, Ltd.: Chichester, UK,* 336-357.

Aboutalebi, M., Torres-Rua, A. F., McKee, M., Kustas, W. P., Nieto, H., Alsina, M. M., ... & Dokoozlian, N. (2020). Incorporation of unmanned aerial vehicle (UAV) point cloud products into remote sensing evapotranspiration models. *Remote sensing, 12*(1), 50.

Acharya, B., & Sharma, V. (2021). Comparison of satellite driven surface energy balance models in estimating crop evapotranspiration in semi-arid to arid inter-mountain region. *Remote Sensing*, *13*(9), 1822.

Allen, R. B., & Peet, R. K. (1990). Gradient analysis of forests of the Sangre de Cristo Range, Colorado. *Canadian Journal of Botany*, *68*(1), 193-201.

Allen, R. G., Burnett, B., Kramber, W., Huntington, J., Kjaersgaard, J., Kilic, A., ... & Trezza, R. (2013). Automated calibration of the METRIC-Landsat evapotranspiration process. *JAWRA Journal of the American Water Resources Association*, *49*(3), 563-576.

Allen, R. G., Hill, R. W., & Srikanth, V. (1994). Evapotranspiration parameters for variably-sized wetlands. In *American Society of Agricultural Engineers. Meeting (USA)*.

Allen, R. G., Pereira, L. S., Raes, D., & Smith, M. (1998). FAO Irrigation and drainage paper No. 56. *Rome: Food and Agriculture Organization of the United Nations*, *56*(97), e156.

Allen, R. G., Tasumi, M., & Trezza, R. (2007). Satellite-based energy balance for mapping evapotranspiration with internalized calibration (METRIC)—Model. *Journal of irrigation and drainage engineering*, *133*(4), 380-394.

Anderson, M. C., Norman, J. M., Mecikalski, J. R., Otkin, J. A., & Kustas, W. P. (2007). A climatological study of evapotranspiration and moisture stress across the continental United States based on thermal remote sensing: 1. Model formulation. *Journal of Geophysical Research: Atmospheres*, *112*(D10).

Anselin, L. (1995). Local indicators of spatial association—LISA. *Geographical analysis*, *27*(2), 93-115.

Armstrong, R. N., Pomeroy, J. W., & Martz, L. W. (2019). Spatial variability of mean daily estimates of actual evaporation from remotely sensed imagery and surface reference data. *Hydrology and Earth System Sciences, 23*(12), 4891-4907.

ASCA. (2020). Treaty Land Acknowledgement. Alberta School Councils' Association. Alberta Education. Edmonton, Alberta.

Bai, M., Mo, X., Liu, S., & Hu, S. (2019). Contributions of climate change and vegetation greening to evapotranspiration trend in a typical hilly-gully basin on the Loess Plateau, China. *Science of the Total Environment*, *657*, 325-339.

Bannari, A., Morin, D., Bonn, F., & Huete, A. R. (1995). A review of vegetation indices. *Remote sensing reviews, 13*(1-2), 95-120.

Barros, C., Gueguen, M., Douzet, R., Carboni, M., Boulangeat, I., Zimmermann, N. E., ... & Thuiller, W. (2017). Extreme climate events counteract the effects of climate and land-use changes in Alpine tree lines. *Journal of applied ecology, 54*(1), 39-50.

Barry, R. G. (1992). *Mountain weather and climate*. Psychology Press.

Bastiaanssen, W. G. (1995). Regionalization of surface flux densities and moisture indicators in composite terrain. *A remote sensing approach under clear skies in Mediterranean climates*, *271*.

Bastiaanssen, W. G. (2000). SEBAL-based sensible and latent heat fluxes in the irrigated Gediz Basin, Turkey. *Journal of hydrology*, *229*(1-2), 87-100.

Bastiaanssen, W. G., Menenti, M., Feddes, R. A., & Holtslag, A. A. M. (1998). A remote sensing surface energy balance algorithm for land (SEBAL). 1. Formulation. *Journal of hydrology*, *212*, 198-212.

Bengtsson, L. (1982). The importance of refreezing on the diurnal snowmelt cycle with application to a northern Swedish catchment. *Hydrology Research*, *13*(1), 1-12.

Betts, A. K., Chen, F., Mitchell, K. E., & Janjić, Z. I. (1997). Assessment of the land surface and boundary layer models in two operational versions of the NCEP Eta model using FIFE data. *Monthly Weather Review*, *125*(11), 2896-2916.

Boots, B. (2002). Local measures of spatial association. *Ecoscience*, *9*(2), 168-176.

Brown, S. M., Petrone, R. M., Mendoza, C., & Devito, K. J. (2010). Surface vegetation controls on evapotranspiration from a sub-humid Western Boreal Plain wetland. *Hydrological Processes: An International Journal, 24*(8), 1072-1085.

Brümmer, C., Black, T. A., Jassal, R. S., Grant, N. J., Spittlehouse, D. L., Chen, B., ... & Wofsy, S. C. (2012). How climate and vegetation type influence evapotranspiration and water use efficiency in Canadian forest, peatland and grassland ecosystems. *Agricultural and Forest Meteorology*, *153*, 14-30.

Calanca, P., Roesch, A., Jasper, K., & Wild, M. (2006). Global warming and the summertime evapotranspiration regime of the Alpine region. *Climatic Change*, *79*(1), 65-78.

Calgary Foundation. (2019). Land Acknowledgement. Retrieved from Calgary Foundation: For Community, Forever: https://calgaryfoundation.org/about-us/vitalpriorities/strengthening-relationships-with-indigenous-communities/landacknowledgement/?fbclid=IwAR3S0eLUkNtMVpenUUycoJLriPmcfa E0viCpK_uH51F BxLvuhpZeSjnftZk

Carrasco-Benavides, M., Ortega-Farías, S., Lagos, L. O., Kleissl, J., Morales-Salinas, L., & Kilic, A. (2014). Parameterization of the satellite-based model (METRIC) for the estimation of

instantaneous surface energy balance components over a drip-irrigated vineyard. *Remote Sensing*, *6*(11), 11342-11371.

Carrillo-Rojas, G., Silva, B., Córdova, M., Célleri, R., & Bendix, J. (2016). Dynamic mapping of evapotranspiration using an energy balance-based model over an Andean páramo catchment of southern Ecuador. *Remote Sensing*, *8*(2), 160.

Caturegli, L., Matteoli, S., Gaetani, M., Grossi, N., Magni, S., Minelli, A., ... & Volterrani, M. (2020). Effects of water stress on spectral reflectance of bermudagrass. *Scientific Reports*, *10*(1), 1-12.

Chapin III, F. S., Bret-Harte, M. S., Hobbie, S. E., & Zhong, H. (1996). Plant functional types as predictors of transient responses of arctic vegetation to global change. *Journal of vegetation Science, 7*(3), 347-358.

Chen, J. M., & Liu, J. (2020). Evolution of evapotranspiration models using thermal and shortwave remote sensing data. *Remote Sensing of Environment, 237*, 111594.

Choler, P. (2005). Consistent shifts in alpine plant traits along a mesotopographical gradient. *Arctic, Antarctic, and Alpine Research, 37*(4), 444-453.

Christensen, C. W. (2017). *A geophysical study of alpine groundwater processes and their geologic controls in the southeastern Canadian Rocky Mountains* (Master's thesis, Graduate Studies).

Christensen, C. W., Hayashi, M., & Bentley, L. R. (2020). Hydrogeological characterization of an alpine aquifer system in the Canadian Rocky Mountains. *Hydrogeology journal*, *28*(5), 1871-1890.

Christensen, L., Tague, C. L., & Baron, J. S. (2008). Spatial patterns of simulated transpiration response to climate variability in a snow dominated mountain ecosystem. *Hydrological Processes: An International Journal*, *22*(18), 3576-3588.

Clark, J. S., Iverson, L., Woodall, C. W., Allen, C. D., Bell, D. M., Bragg, D. C., ... & Jackson, S. T. (2016). The impacts of increasing drought on forest dynamics, structure, and biodiversity in the United States. *Global change biology*, *22*(7), 2329-2352.

Colomina, I., & Molina, P. (2014). Unmanned aerial systems for photogrammetry and remote sensing: A review. *ISPRS Journal of photogrammetry and remote sensing*, *92*, 79-97.

Condon, L. E., Atchley, A. L., & Maxwell, R. M. (2020). Evapotranspiration depletes groundwater under warming over the contiguous United States. *Nature communications*, *11*(1), 1-8.

Coners, H., Babel, W., Willinghöfer, S., Biermann, T., Köhler, L., Seeber, E., ... & Leuschner, C. (2016). Evapotranspiration and water balance of high-elevation grassland on the Tibetan Plateau. *Journal of Hydrology*, *533*, 557-566.

Cui, J., An, S., Wang, Z., Fang, C., Liu, Y., Yang, H., ... & Liu, S. (2009). Using deuterium excess to determine the sources of high-altitude precipitation: Implications in hydrological

relations between sub-alpine forests and alpine meadows. *Journal of Hydrology*, *373*(1-2), 24-33.

Culicov, O. A., & Yurukova, L. (2006). Comparison of element accumulation of different moss- and lichen-bags, exposed in the city of Sofia (Bulgaria). *Journal of atmospheric chemistry*, *55*(1), 1-12.

DeBeer, C. M., Wheater, H. S., Carey, S. K., & Chun, K. P. (2016). Recent climatic, cryospheric, and hydrological changes over the interior of western Canada: a review and synthesis. *Hydrology and Earth System Sciences, 20*(4), 1573.

Dhungel, S., & Barber, M. E. (2018). Estimating calibration variability in evapotranspiration derived from a satellite-based energy balance model. *Remote sensing*, *10*(11), 1695.

Diarra, A., Jarlan, L., Er-Raki, S., Le Page, M., Aouade, G., Tavernier, A., ... & Khabba, S. (2017). Performance of the two-source energy budget (TSEB) model for the monitoring of evapotranspiration over irrigated annual crops in North Africa. *Agricultural water management, 193*, 71-88.

Dingman, S. L. (2015). *Physical hydrology*. Waveland press.

Dubayah, R., & Rich, P. M. (1995). Topographic solar radiation models for GIS. *International journal of geographical information systems, 9*(4), 405-419.

Duffie, J. A., & Beckman, W. A. (1991). Solar Engineering of Thermal Processes. *John Wiley & Sons, Ind.*, 250-330.

Duguay, C. R. (1993). Radiation modeling in mountainous terrain review and status. *Mountain research and development*, 339-357.

Dymond, C. C., & Johnson, E. A. (2002). Mapping vegetation spatial patterns from modeled water, temperature and solar radiation gradients. *ISPRS Journal of Photogrammetry and Remote Sensing*, *57*(1-2), 69-85.

Fang, L., Hain, C. R., Zhan, X., & Anderson, M. C. (2016). An inter-comparison of soil moisture data products from satellite remote sensing and a land surface model. *International journal of applied earth observation and geoinformation*, *48*, 37-50.

Fu, D., Chen, B., Zhang, H., Wang, J., Black, T. A., Amiro, B. D., ... & Verma, S. (2014). Estimating landscape net ecosystem exchange at high spatial–temporal resolution based on Landsat data, an improved upscaling model framework, and eddy covariance flux measurements. *Remote Sensing of Environment*, *141*, 90-104.

Ge, Y., Liang, Y., Wang, J., Zhao, Q., & Liu, S. (2014). Upscaling sensible heat fluxes with area-to-area regression kriging. *IEEE Geoscience and Remote Sensing Letters*, *12*(3), 656-660.

Giménez, C., Gallardo, M., & Thompson, R. B. (2005). Plant – Water Relations. In *Encyclopedia of Soils in the Environment* (pp. 231–238). Elsevier.

Grime, J. P. (2006). Trait convergence and trait divergence in herbaceous plant communities: mechanisms and consequences. *Journal of Vegetation Science, 17*(2), 255-260.

Gu, S., Tang, Y., Cui, X., Kato, T., Du, M., Li, Y., & Zhao, X. (2005). Energy exchange between the atmosphere and a meadow ecosystem on the Qinghai–Tibetan Plateau. *Agricultural and Forest Meteorology*, *129*(3-4), 175-185.

Gueymard, C. (1995). *SMARTS2: a simple model of the atmospheric radiative transfer of sunshine: algorithms and performance assessment* (Vol. 1, p. 85). Cocoa, FL: Florida Solar Energy Center.

Guzinski, R., Nieto, H., Stisen, S., & Fensholt, R. (2015). Inter-comparison of energy balance and hydrological models for land surface energy flux estimation over a whole river catchment. *Hydrology and Earth System Sciences*, *19*(4), 2017-2036.

Hannah, D. M., Brown, L. E., Milner, A. M., Gurnell, A. M., McGregor, G. R., Petts, G. E., ... & Snook, D. L. (2007). Integrating climate–hydrology–ecology for alpine river systems. *Aquatic Conservation: Marine and Freshwater Ecosystems, 17*(6), 636-656.

Harder, P., Pomeroy, J. W., & Westbrook, C. J. (2015). Hydrological resilience of a Canadian Rockies headwaters basin subject to changing climate, extreme weather, and forest management. *Hydrological Processes, 29*(18), 3905-3924.

Harte, J., Saleska, S., & Shih, T. (2006). Shifts in plant dominance control carbon-cycle responses to experimental warming and widespread drought. *Environmental Research Letters*, *1*(1), 014001.

Hauer, F. R., Baron, J. S., Campbell, D. H., Fausch, K. D., Hostetler, S. W., Leavesley, G. H., ... & Stanford, J. A. (1997). Assessment of climate change and freshwater ecosystems of the Rocky Mountains, USA and Canada. *Hydrological Processes, 11*(8), 903-924.

Hayashi, M. (2020). Alpine hydrogeology: The critical role of groundwater in sourcing the headwaters of the world. *Groundwater*, *58*(4), 498-510.

Hayashi, M., van der Kamp, G., & Schmidt, R. (2003). Focused infiltration of snowmelt water in partially frozen soil under small depressions. *Journal of Hydrology*, *270*(3-4), 214-229.

He, H. S., Hao, Z., Mladenoff, D. J., Shao, G., Hu, Y., & Chang, Y. (2005). Simulating forest ecosystem response to climate warming incorporating spatial effects in north-eastern China. *Journal of Biogeography*, *32*(12), 2043-2056.

He, R., Jin, Y., Kandelous, M. M., Zaccaria, D., Sanden, B. L., Snyder, R. L., ... & Hopmans, J. W. (2017). Evapotranspiration estimate over an almond orchard using Landsat satellite observations. *Remote Sensing*, *9*(5), 436.

Healy, R. W., Winter, T. C., LaBaugh, J. W., & Franke, O. L. (2007). *Water budgets: foundations for effective water-resources and environmental management* (Vol. 1308, p. 90). Reston, Virginia: US Geological Survey.

Heijmans, M. M., Arp, W. J., & Chapin III, F. S. (2004). Controls on moss evaporation in a boreal black spruce forest. *Global Biogeochemical Cycles*, *18*(2).

Hoegh-Guldberg, O., Jacob, D., Bindi, M., Brown, S., Camilloni, I., Diedhiou, A., ... & Hijioka, Y. (2018). Impacts of 1.5 C global warming on natural and human systems. *Global warming of 1.5° C. An IPCC Special Report*.

Hoffmann, H., Nieto, H., Jensen, R., Guzinski, R., Zarco-Tejada, P., & Friborg, T. (2016). Estimating evaporation with thermal UAV data and two-source energy balance models. *Hydrology and Earth System Sciences*, *20*(2), 697-713.

Honkavaara, E., Eskelinen, M. A., Pölönen, I., Saari, H., Ojanen, H., Mannila, R., ... & Pulkkanen, M. (2016). Remote sensing of 3-D geometry and surface moisture of a peat production area using hyperspectral frame cameras in visible to short-wave infrared spectral ranges onboard a small unmanned airborne vehicle (UAV). *IEEE Transactions on Geoscience and Remote Sensing, 54*(9), 5440-5454.

Hopkins, W. G. (2006). *Photosynthesis and respiration*. Infobase Publishing.

Hopkinson, C., Chasmer, L. E., Sass, G., Creed, I. F., Sitar, M., Kalbfleisch, W., & Treitz, P. (2005). Vegetation class dependent errors in lidar ground elevation and canopy height estimates in a boreal wetland environment. *Canadian Journal of Remote Sensing*, *31*(2), 191-206.

Houborg, R., Anderson, M., Gao, F., Schull, M., & Cammalleri, C. (2012, July). Monitoring water and carbon fluxes at fine spatial scales using HyspIRI-like measurements. In *2012 IEEE International Geoscience and Remote Sensing Symposium* (pp. 7302-7305). IEEE.

Hrach, D. M., Petrone, R. M., Van Huizen, B., Green, A., & Khomik, M. (2021). The Impact of Variable Horizon Shade on the Growing Season Energy Budget of a Subalpine Headwater Wetland. *Atmosphere*, *12*(11), 1473.

Hu, T., Ma, Q., Su, Y., Battles, J. J., Collins, B. M., Stephens, S. L., ... & Guo, Q. (2019). A simple and integrated approach for fire severity assessment using bi-temporal airborne LiDAR data. *International Journal of Applied Earth Observation and Geoinformation*, *78*, 25-38.

Huntingford, C., Blyth, E. M., Wood, N., Hewer, F. E., & Grant, A. (1998). The effect of orography on evaporation. *Boundary-layer meteorology*, *86*(3), 487-504.

Intergovernmental Panel on Climate Change. (2013). Climate change 2013: The physical science basis. *Contribution of working group I to the fifth assessment report of the intergovernmental panel on climate change*, *1535*.

Isard, S. A. (1989). Topoclimatic controls in an alpine fellfield and their ecological significance. Physical Geography, 10(1), 13-31.

Isard, S. A. (1986). Factors influencing soil moisture and plant community distribution on Niwot Ridge, Front Range, Colorado, USA. *Arctic and Alpine Research*, *18*(1), 83-96.

Jarvis, P. G., & McNaughton, K. G. (1986). Stomatal control of transpiration: scaling up from leaf to region. *Advances in ecological research*, *15*, 1-49.

Jiang, C., Ryu, Y., Fang, H., Myneni, R., Claverie, M., & Zhu, Z. (2017). Inconsistencies of interannual variability and trends in long-term satellite leaf area index products. *Global Change Biology*, *23*(10), 4133-4146.

Jovanovic, N., & Israel, S. (2012). Critical review of methods for the estimation of actual evapotranspiration in hydrological models. *Evapotranspiration-Remote Sensing and Modeling*, 24.

Jung, M., Reichstein, M., Ciais, P., Seneviratne, S. I., Sheffield, J., Goulden, M. L., ... & Zhang, K. (2010). Recent decline in the global land evapotranspiration trend due to limited moisture supply. *Nature*, *467*(7318), 951-954.

Kerkhoven, E., & Gan, T. Y. (2011). Differences and sensitivities in potential hydrologic impact of climate change to regional-scale Athabasca and Fraser River basins of the leeward and windward sides of the Canadian Rocky Mountains respectively. *Climatic Change*, *106*(4), 583-607.

Knowles, J. F., Harpold, A. A., Cowie, R., Zeliff, M., Barnard, H. R., Burns, S. P., ... & Williams, M. W. (2015). The relative contributions of alpine and subalpine ecosystems to the water balance of a mountainous, headwater catchment. *Hydrological Processes, 29*(22), 4794-4808.

Körner, C. (2003). *Alpine plant life: functional plant ecology of high mountain ecosystems; with 47 tables.* Springer Science & Business Media.

Körner, C. (2007). The use of 'altitude' in ecological research. *Trends in ecology & evolution*, *22*(11), 569-574.

Körner, C., Neumayer, M., Menendez-Riedl, S. P., & Smeets-Scheel, A. (1989). Functional morphology of mountain plants. *Flora*, *182*(5-6), 353-383.

Lafleur, P. M., McCaughey, J. H., Joiner, D. W., Bartlett, P. A., & Jelinski, D. E. (1997). Seasonal trends in energy, water, and carbon dioxide fluxes at a northern boreal wetland. *Journal of Geophysical Research: Atmospheres*, *102*(D24), 29009-29020.

Lapp, S., Byrne, J., Townshend, I., & Kienzle, S. (2005). Climate warming impacts on snowpack accumulation in an alpine watershed. *International Journal of Climatology: A Journal of the Royal Meteorological Society, 25*(4), 521-536.

LeCain, D. R., Morgan, J. A., Schuman, G. E., Reeder, J. D., & Hart, R. H. (2002). Carbon exchange and species composition of grazed pastures and exclosures in the shortgrass steppe of Colorado. *Agriculture, ecosystems & environment*, *93*(1-3), 421-435.

Lee, S. Y., Ryan, M. E., Hamlet, A. F., Palen, W. J., Lawler, J. J., & Halabisky, M. (2015). Projecting the hydrologic impacts of climate change on montane wetlands. *Plos one*, *10*(9), e0136385.

Leith, R. M., & Whitfield, P. H. (1998). Evidence of climate change effects on the hydrology of streams in south-central BC. *Canadian Water Resources Journal*, *23*(3), 219-230.

Li, H., Zhang, F., Zhu, J., Guo, X., Li, Y., Lin, L., ... & Du, M. (2021). Precipitation rather than evapotranspiration determines the warm-season water supply in an alpine shrub and an alpine meadow. *Agricultural and Forest Meteorology*, *300*, 108318.

Li, X., Liu, S., Li, H., Ma, Y., Wang, J., Zhang, Y., ... & Guo, Z. (2018). Intercomparison of six upscaling evapotranspiration methods: From site to the satellite pixel. *Journal of Geophysical Research: Atmospheres*, *123*(13), 6777-6803.

Liang, S. (2001). Narrowband to broadband conversions of land surface albedo I: Algorithms. *Remote sensing of environment*, *76*(2), 213-238.

Liu, J., Cheng, F., Munger, W., Jiang, P., Whitby, T. G., Chen, S., ... & Man, X. (2020). Precipitation extremes influence patterns and partitioning of evapotranspiration and transpiration in a deciduous boreal larch forest. *Agricultural and Forest Meteorology*, *287*, 107936.

Liu, S., Xu, Z., Song, L., Zhao, Q., Ge, Y., Xu, T., ... & Zhang, F. (2016). Upscaling evapotranspiration measurements from multi-site to the satellite pixel scale over heterogeneous land surfaces. *Agricultural and Forest Meteorology, 230*, 97-113.

Liu, Y., Liu, R., & Chen, J. M. (2012). Retrospective retrieval of long-term consistent global leaf area index (1981–2011) from combined AVHRR and MODIS data. *Journal of Geophysical Research: Biogeosciences, 117*(G4).

Luo, S., Wang, C., Pan, F., Xi, X., Li, G., Nie, S., & Xia, S. (2015). Estimation of wetland vegetation height and leaf area index using airborne laser scanning data. *Ecological Indicators*, *48*, 550-559.

Malek, E. (1992). Night-time evapotranspiration vs. daytime and 24h evapotranspiration. *Journal of Hydrology*, *138*(1-2), 119-129.

Marsh, C. B., Pomeroy, J. W., & Spiteri, R. J. (2012). Implications of mountain shading on calculating energy for snowmelt using unstructured triangular meshes. *Hydrological Processes, 26*(12), 1767-1778.

McCaughey, J. H. (1978). Estimation of net radiation for a coniferous forest, and the effects of logging on net radiation and the reflection coefficient. *Canadian Journal of Forest Research*, *8*(4), 450-455.

McLeod, M. K., Daniel, H., Faulkner, R., & Murison, R. (2004). Evaluation of an enclosed portable chamber to measure crop and pasture actual evapotranspiration at small scale. *Agricultural water management, 67*(1), 15-34.

McNaughton, K. G., & Jarvis, P. G. (1983). Predicting effects of vegetation changes on transpiration and evaporation. *Water deficits and plant growth*, *7*, 1-47.

Menzel, L., & Lang, H. (1998). Spatial variation in evapotranspiration in Swiss Alpine regions. *IAHS Publications-Series of Proceedings and Reports-Intern Assoc Hydrological Sciences*, *248*, 115-122.

Mitchell, P. J., Lane, P. N., & Benyon, R. G. (2012). Capturing within catchment variation in evapotranspiration from montane forests using LiDAR canopy profiles with measured and modelled fluxes of water. *Ecohydrology, 5*(6), 708-720.

Mitsch, W. J., & Wu, X. (1995). *Wetlands and global change* (pp. 205-230). Boca Raton, CRC Lewis Publishers.

Monteith, J. L. (1963). Gas exchange in plant communities. *Environmental control of plant growth*, *95*, 95-112.

Nachabe, M., Shah, N., Ross, M., & Vomacka, J. (2005). Evapotranspiration of two vegetation covers in a shallow water table environment. *Soil Science Society of America Journal*, *69*(2), 492-499.

Newton, B. W., Prowse, T. D., & Bonsal, B. R. (2014). Evaluating the distribution of water resources in western Canada using synoptic climatology and selected teleconnections. Part 1: Winter season. *Hydrological Processes*, *28*(14), 4219-4234.

Nieto, H., Kustas, W. P., Torres-Rúa, A., Alfieri, J. G., Gao, F., Anderson, M. C., ... & McKee, L. G. (2019). Evaluation of TSEB turbulent fluxes using different methods for the retrieval of soil and canopy component temperatures from UAV thermal and multispectral imagery. *Irrigation science, 37*(3), 389-406.

Niu, H., Hollenbeck, D., Zhao, T., Wang, D., & Chen, Y. (2020). Evapotranspiration estimation with small UAVs in precision agriculture. *Sensors*, *20*(22), 6427.

Niu, Y., Yang, S., Zhou, J., Chu, B., Ma, S., Zhu, H., & Hua, L. (2019). Vegetation distribution along mountain environmental gradient predicts shifts in plant community response to climate change in alpine meadow on the Tibetan Plateau. *Science of the Total Environment*, *650*, 505-514.

Nkemdirim, L. C. (1996). Canada's chinook belt. *International Journal of Climatology: A Journal of the Royal Meteorological Society*, *16*(4), 441-462.

Norman, J. M., Kustas, W. P., & Humes, K. S. (1995). Source approach for estimating soil and vegetation energy fluxes in observations of directional radiometric surface temperature. *Agricultural and Forest Meteorology, 77*(3-4), 263-293.

Nybakken, L., Sandvik, S. M., & Klanderud, K. (2011). Experimental warming had little effect on carbon-based secondary compounds, carbon and nitrogen in selected alpine plants and lichens. *Environmental and Experimental Botany*, *72*(3), 368-376.

Ohta, T., Maximov, T. C., Dolman, A. J., Nakai, T., van der Molen, M. K., Kononov, A. V., ... & Yabuki, H. (2008). Interannual variation of water balance and summer evapotranspiration in an eastern Siberian larch forest over a 7-year period (1998–2006). *Agricultural and Forest Meteorology*, *148*(12), 1941-1953.

Oke, T. R. (1978). *Boundary layer climates: Second Condition*. Routledge.

Osmond, H. L. (1941). The chinook wind east of the Canadian Rockies. *Canadian Journal of Research*, *19*(4), 57-66.

Pape, R., & Löffler, J. (2016). Spatial patterns of alpine phytomass, primary productivity, and related calorific resources. *Ecosphere*, *7*(6), e01347.

Parker, B. R., Vinebrooke, R. D., & Schindler, D. W. (2008). Recent climate extremes alter alpine lake ecosystems. *Proceedings of the National Academy of Sciences*, *105*(35), 12927-12931.

Paulson, C. A. (1970). The mathematical representation of wind speed and temperature profiles in the unstable atmospheric surface layer. *Journal of Applied Meteorology and Climatology*, *9*(6), 857-861.

Paznekas, A., & Hayashi, M. (2016). Groundwater contribution to winter streamflow in the Canadian Rockies. *Canadian Water Resources Journal/Revue canadienne des ressources hydriques, 41*(4), 484-499.

Pei, T., Wu, X., Li, X., Zhang, Y., Shi, F., Ma, Y., ... & Zhang, C. (2017). Seasonal divergence in the sensitivity of evapotranspiration to climate and vegetation growth in the Yellow River Basin, China. *Journal of Geophysical Research: Biogeosciences*, *122*(1), 103-118.

Peñuelas, J., Filella, I., Biel, C., Serrano, L., & Save, R. (1993). The reflectance at the 950–970 nm region as an indicator of plant water status. *International journal of remote sensing*, *14*(10), 1887-1905.

Petrone, R. M., Chasmer, L., Hopkinson, C., Silins, U., Landhäusser, S. M., Kljun, N., & Devito, K. J. (2015). Effects of harvesting and drought on CO_2 and H_2O fluxes in an aspen-dominated western boreal plain forest: early chronosequence recovery. *Canadian Journal of Forest Research, 45*(1), 87-100.

Petrone, R. M., Price, J. S., Carey, S. K., & Waddington, J. M. (2004). Statistical characterization of the spatial variability of soil moisture in a cutover peatland. *Hydrological processes, 18*(1), 41-52.

Petrone, R. M., Waddington, J. M., & Price, J. S. (2001). Ecosystem scale evapotranspiration and net CO_2 exchange from a restored peatland. *Hydrological processes, 15*(14), 2839-2845.

Phillips, T., Petrone, R. M., Wells, C. M., & Price, J. S. (2016). Characterizing dominant controls governing evapotranspiration within a natural saline fen in the Athabasca Oil Sands of Alberta, Canada. *Ecohydrology*, *9*(5), 817-829.

Pomeroy, J. W., Harder, P., & Galloway, G. (2020 unpublished). UAV Imagery at Bonsai 2020. *Unpublished Data*.

Pomeroy, J. W., Harder, P., & Heavens, R. (2020 unpublished). Spectral Signatures at Bonsai 2020. *Unpublished Data*.

Pomeroy, J., MacDonald, M., DeBeer, C., & Brown, T. (2009). Modelling alpine snow hydrology in the Canadian Rocky Mountains. In *77th Annual Meeting of the Western Snow Conference* (pp. 3-11).

Pomeroy, J. W., Toth, B., Granger, R. J., Hedstrom, N. R., & Essery, R. L. H. (2003). Variation in surface energetics during snowmelt in a subarctic mountain catchment. *Journal of Hydrometeorology, 4*(4), 702-719.

Raz-Yaseef, N., Young-Robertson, J., Rahn, T., Sloan, V., Newman, B., Wilson, C., ... & Torn, M. S. (2017). Evapotranspiration across plant types and geomorphological units in polygonal Arctic tundra. *Journal of Hydrology*, *553*, 816-825.

Reich, P. B., Tjoelker, M. G., Walters, M. B., Vanderklein, D. W., & Buschena, C. (1998). Close association of RGR, leaf and root morphology, seed mass and shade tolerance in seedlings of nine boreal tree species grown in high and low light. *Functional Ecology*, *12*(3), 327-338.

Reinelt, E. R. (1970). On the role of orography in the precipitation regime of Alberta. *Albertan Geographer*, *6*, 45-58.

Rejmánková, E., Rejmánek, M., Djohan, T., & Goldman, C. R. (1999). Resistance and resilience of subalpine wetlands with respect to prolonged drought. *Folia Geobotanica, 34*(2), 175-188.

Rinehart, A. J., Vivoni, E. R., & Brooks, P. D. (2008). Effects of vegetation, albedo, and solar radiation sheltering on the distribution of snow in the Valles Caldera, New Mexico. *Ecohydrology: Ecosystems, Land and Water Process Interactions, Ecohydrogeomorphology, 1*(3), 253-270.

Rood, S. B., Pan, J., Gill, K. M., Franks, C. G., Samuelson, G. M., & Shepherd, A. (2008). Declining summer flows of Rocky Mountain rivers: Changing seasonal hydrology and probable impacts on floodplain forests. *Journal of Hydrology*, *349*(3-4), 397-410.

Rooney, R., Bolding, M., & Lei, C. (2019 unpublished). Vegetation Survey at Bonsai at Bonsai 2019. *Unpublished Data*.

Rouse, J. W., Haas, R. H., Deering, D. W., Schell, J. A., & Harlan, J. C. (1974). *Monitoring the vernal advancement and retrogradation (green wave effect) of natural vegetation* (No. E75-10354).

Sadro, S., Gastil-Buhl, M., & Melack, J. (2007). Characterizing patterns of plant distribution in a southern California salt marsh using remotely sensed topographic and hyperspectral data and local tidal fluctuations. *Remote Sensing of Environment*, *110*(2), 226-239.

Sanchez, A., Hughes, N. M., & Smith, W. K. (2016). Leaf/shoot level ecophysiology in two broadleaf and two needle-leaf species under representative cloud regimes at alpine treeline. *Journal of Plant Ecology*, *9*(6), 762-772.

Saugier, B., & Katerji, N. (1991). Some plant factors controlling evapotranspiration. *Agricultural and Forest Meteorology, 54*(2-4), 263-277.

Schoennagel, T., Veblen, T. T., & Romme, W. H. (2004). The interaction of fire, fuels, and climate across Rocky Mountain forests. *BioScience, 54*(7), 661-676.

Senior, R. A., Hill, J. K., & Edwards, D. P. (2019). ThermStats: an R package for quantifying surface thermal heterogeneity in assessments of microclimates. *Methods in Ecology and Evolution*, *10*(9), 1606-1614.

Shea, J. M., & Marshall, S. J. (2007). Atmospheric flow indices, regional climate, and glacier mass balance in the Canadian Rocky Mountains. *International Journal of Climatology: A Journal of the Royal Meteorological Society*, *27*(2), 233-247.

Shuttleworth, W. J. (2012). *Terrestrial hydrometeorology*. John Wiley & Sons.

Siewert, M. B., & Olofsson, J. (2020). Scale-dependency of Arctic ecosystem properties revealed by UAV. *Environmental Research Letters*, *15*(9), 094030.

Simpson, G., Runkle, B. R., Eckhardt, T., & Kutzbach, L. (2019). Evaluating closed chamber evapotranspiration estimates against eddy covariance measurements in an arctic wetland. *Journal of Hydrology, 578,* 124030.

Sims, D. A., & Gamon, J. A. (2003). Estimation of vegetation water content and photosynthetic tissue area from spectral reflectance: a comparison of indices based on liquid water and chlorophyll absorption features. *Remote sensing of environment*, *84*(4), 526-537.

Sloat, L. L., Henderson, A. N., Lamanna, C., & Enquist, B. J. (2015). The effect of the foresummer drought on carbon exchange in subalpine meadows. *Ecosystems*, *18*(3), 533-545.

Smith, C. D. (2008). The relationship between monthly precipitation and elevation in the Alberta foothills during the foothills orographic precipitation experiment. In *Cold Region Atmospheric and Hydrologic Studies. The Mackenzie GEWEX Experience* (pp. 167-185). Springer, Berlin, Heidelberg.

Smith, T. M., Shugart, H. H., Woodward, F. I., & Burton, P. J. (1993). Plant functional types. In *Vegetation Dynamics & Global Change* (pp. 272-292). Springer, Boston, MA.

Solondz, D. S., Petrone, R. M., & Devito, K. J. (2008). Forest floor carbon dioxide fluxes within an upland-peatland complex in the Western Boreal Plain, Canada. *Ecohydrology: Ecosystems, Land and Water Process Interactions, Ecohydrogeomorphology*, *1*(4), 361-376.

Sospedra-Alfonso, R., Melton, J. R., & Merryfield, W. J. (2015). Effects of temperature and precipitation on snowpack variability in the Central Rocky Mountains as a function of elevation. *Geophysical Research Letters, 42*(11), 4429-4438.

Spies, R. R., Franz, K. J., Hogue, T. S., & Bowman, A. L. (2015). Distributed hydrologic modeling using satellite-derived potential evapotranspiration. *Journal of Hydrometeorology*, *16*(1), 129-146.

Stanisci, A., Bricca, A., Calabrese, V., Cutini, M., Pauli, H., Steinbauer, K., & Carranza, M. L. (2020). Functional composition and diversity of leaf traits in subalpine versus alpine vegetation in the Apennines. *AoB Plants, 12*(2), plaa004.

Stannard, D. I. (1988). *Use of a hemispherical chamber for measurement of evapotranspiration* (No. 88-452). Dept. of the Interior, US Geological Survey: Books and Open-File Reports [distributor].

Tang, R., Li, Z. L., Jia, Y., Li, C., Chen, K. S., Sun, X., & Lou, J. (2013). Evaluating one-and two-source energy balance models in estimating surface evapotranspiration from Landsat-derived surface temperature and field measurements. *International Journal of Remote Sensing*, *34*(9-10), 3299-3313.

Tasumi, M. (2003). *Progress in operational estimation of regional evapotranspiration using satellite imagery*. University of Idaho.

Tasumi, M. (2019). Estimating evapotranspiration using METRIC model and Landsat data for better understandings of regional hydrology in the western Urmia Lake Basin. *Agricultural water management*, *226*, 105805.

Tasumi, M., Allen, R. G., & Trezza, R. (2008). At-surface reflectance and albedo from satellite for operational calculation of land surface energy balance. *Journal of hydrologic engineering*, *13*(2), 51-63.

Tattersall, G. J. (2016). Infrared thermography: A non-invasive window into thermal physiology. *Comparative Biochemistry and Physiology Part A: Molecular & Integrative Physiology,* 202, 78-98.

Thériault, J. M., Déry, S. J., Pomeroy, J. W., Smith, H. M., Almonte, J., Bertoncini, A., ... & Thompson, H. D. (2021). Meteorological observations collected during the Storms and Precipitation Across the continental Divide Experiment (SPADE), April–June 2019. *Earth System Science Data*, *13*(3), 1233-1249.

Toetz, D. (1995). Water chemistry and periphyton in an alpine wetland. *Hydrobiologia*, *312*(2), 93-105.

Torres-Rua, A., Ticlavilca, A. M., Aboutalebi, M., Nieto, H., Alsina, M. M., White, A., ... & Dokoozlian, N. (2020, May). Estimation of evapotranspiration and energy fluxes using a deep-learning-based high-resolution emissivity model and the two-source energy balance model with sUAS information. In *Autonomous Air and Ground Sensing Systems for*

Agricultural Optimization and Phenotyping V (Vol. 11414, p. 114140B). International Society for Optics and Photonics.

Trenberth, K. E., Smith, L., Qian, T., Dai, A., & Fasullo, J. (2007). Estimates of the global water budget and its annual cycle using observational and model data. *Journal of Hydrometeorology*, *8*(4), 758-769.

Tromp-van Meerveld, H. J., & McDonnell, J. J. (2006). On the interrelations between topography, soil depth, soil moisture, transpiration rates and species distribution at the hillslope scale. *Advances in water resources*, *29*(2), 293-310.

van den Bergh, T., Inauen, N., Hiltbrunner, E., & Körner, C. (2013). Climate and plant cover co-determine the elevational reduction in evapotranspiration in the Swiss Alps. *Journal of hydrology*, *500*, 75-83.

Viviroli, D., & Weingartner, R. (2004). The hydrological significance of mountains: from regional to global scale. *Hydrology and earth system sciences, 8*(6), 1017-1030.

Viviroli, D., Weingartner, R., & Messerli, B. (2003). Assessing the hydrological significance of the world's mountains. *Mountain research and Development*, *23*(1), 32-40.

Walker, M. D., Wahren, C. H., Hollister, R. D., Henry, G. H., Ahlquist, L. E., Alatalo, J. M., ... & Epstein, H. E. (2006). Plant community responses to experimental warming across the tundra biome. *Proceedings of the National Academy of Sciences*, *103*(5), 1342-1346.

Walter, I. A., Allen, R. G., Elliott, R., Jensen, M. E., Itenfisu, D., Mecham, B., ... & Martin, D. (2000). ASCE's standardized reference evapotranspiration equation. In *Watershed management and operations management 2000* (pp. 1-11).

Wang, S., Garcia, M., Ibrom, A., & Bauer-Gottwein, P. (2020). Temporal interpolation of land surface fluxes derived from remote sensing–results with an unmanned aerial system. *Hydrology and Earth System Sciences, 24*(7), 3643-3661.

Wasti, S. (2020). Estimation of land surface Evapotranspiration in Nepal using Landsat based METRIC model. *arXiv preprint arXiv:2007.13922*.

Webb, E. K. (1970). Profile relationships: The log-linear range, and extension to strong stability. *Quarterly Journal of the Royal Meteorological Society*, *96*(407), 67-90.

Whitfield, P. H. (2012). Floods in future climates: a review. *Journal of Flood Risk Management, 5*(4), 336-365.

Whitfield, P. H., & Pomeroy, J. W. (2016). Changes to flood peaks of a mountain river: implications for analysis of the 2013 flood in the Upper Bow River, Canada. *Hydrological Processes, 30*(25), 4657-4673.

Whitfield, P. H., Moore, R. D., Fleming, S. W., & Zawadzki, A. (2010). Pacific decadal oscillation and the hydroclimatology of western Canada—Review and prospects. *Canadian Water Resources Journal*, *35*(1), 1-28.

Whittaker, R. H., Buol, S. W., Niering, W. A., & Havens, Y. H. (1968). A soil and vegetation pattern in the Santa Catalina Mountains, Arizona. *Soil Science, 105*(6), 440-450.

Whittington, P. N., & Price, J. S. (2006). The effects of water table draw-down (as a surrogate for climate change) on the hydrology of a fen peatland, Canada. *Hydrological Processes*, *20*(17), 3589-3600.

Wickland, K. P., Striegl, R. G., Schmidt, S. K., & Mast, M. A. (1999). Methane flux in subalpine wetland and unsaturated soils in the southern Rocky Mountains. *Global Biogeochemical Cycles*, *13*(1), 101-113.

Wissinger, S. A., Bohonak, A. J., Whiteman, H. H., & Brown, W. S. (1999). Subalpine wetlands in Colorado: habitat permanence, salamander predation, and invertebrate communities. *Invertebrates in freshwater wetlands of North America: ecology and management. Wiley, New York,* 757-790.

Xu, M., An, T., Zheng, Z., Zhang, T., Zhang, Y., & Yu, G. (2022). Variability in evapotranspiration shifts from meteorological to biological control under wet versus drought conditions in an alpine meadow. *Journal of Plant Ecology*.

Xu, X., Asawa, T., & Kobayashi, H. (2020). Narrow-to-Broadband Conversion for Albedo Estimation on Urban Surfaces by UAV-Based Multispectral Camera. *Remote Sensing*, *12*(14), 2214.

Yan, C., Takeuchi, S., & Qiu, G. Y. (2019). Soil warming affects sap flow responses to meteorological conditions for Betula albosinensis at a subalpine wetland in the edge of northeast Qinghai–Tibet Plateau. *Ecohydrology, 12*(3), e2079.

Yengoh, G. T., Dent, D., Olsson, L., Tengberg, A. E., & Tucker III, C. J. (2015). *Use of the Normalized Difference Vegetation Index (NDVI) to assess Land degradation at multiple scales: current status, future trends, and practical considerations*. Springer.

Yuan, Y., Wang, X., Yin, F., & Zhan, J. (2013). Examination of the quantitative relationship between vegetation canopy height and LAI. *Advances in Meteorology*, *2013*.

Zecha, C. W., Link, J., & Claupein, W. (2013). Mobile sensor platforms: categorisation and research applications in precision farming. *Journal of Sensors and Sensor Systems, 2*(1), 51-72.

Zhang, S. Y., Li, X. Y., Zhao, G. Q., & Huang, Y. M. (2016). Surface energy fluxes and controls of evapotranspiration in three alpine ecosystems of Qinghai Lake watershed, NE Qinghai-Tibet Plateau. *Ecohydrology*, *9*(2), 267-279.

Zhang, X., Vincent, L. A., Hogg, W. D., & Niitsoo, A. (2000). Temperature and precipitation trends in Canada during the 20th century. *Atmosphere-ocean*, *38*(3), 395-429.

Zhang, Y., Peña-Arancibia, J. L., McVicar, T. R., Chiew, F. H., Vaze, J., Liu, C., ... & Pan, M. (2016). Multi-decadal trends in global terrestrial evapotranspiration and its components. *Scientific reports, 6*(1), 1-12.

Zhang, Y., Wang, G., & Wang, Y. (2011). Changes in alpine wetland ecosystems of the Qinghai–Tibetan plateau from 1967 to 2004. *Environmental monitoring and assessment*, *180*(1-4), 189-199.

Zhao, L., Li, J., Xu, S., Zhou, H., Li, Y., Gu, S., & Zhao, X. (2010). Seasonal variations in carbon dioxide exchange in an alpine wetland meadow on the Qinghai-Tibetan Plateau. *Biogeosciences, 7*(4), 1207-1221.

Zheng, G., & Moskal, L. M. (2009). Retrieving leaf area index (LAI) using remote sensing: theories, methods and sensors. *Sensors, 9*(4), 2719-2745.

Zon, R. (1914). *Balsam fir* (No. 55). US Department of Agriculture.

Appendix 1: UAV Imagery

Multispectral images were collected on August 26 (Figure A-1) and an NDVI image was calculated using Equation 5 from the multispectral imagery (Figure A-2). Thermal imagery was collected on August 26 and brightness temperature was compared to surface temperature measurements using surface temperature sensors at the site (Figure A-3). As biases in surface temperature are corrected during the internal calibration of sensible heat flux in METRIC (Allen et al., 2007) and emissivity is not expected to vary substantially (0.96-0.99) between vegetation types (Messina & Modica, 2020), brightness temperature values were used as surface temperature in METRIC. The LiDAR point cloud imagery used for the canopy height model was collected on August 24 (Figure A-4).
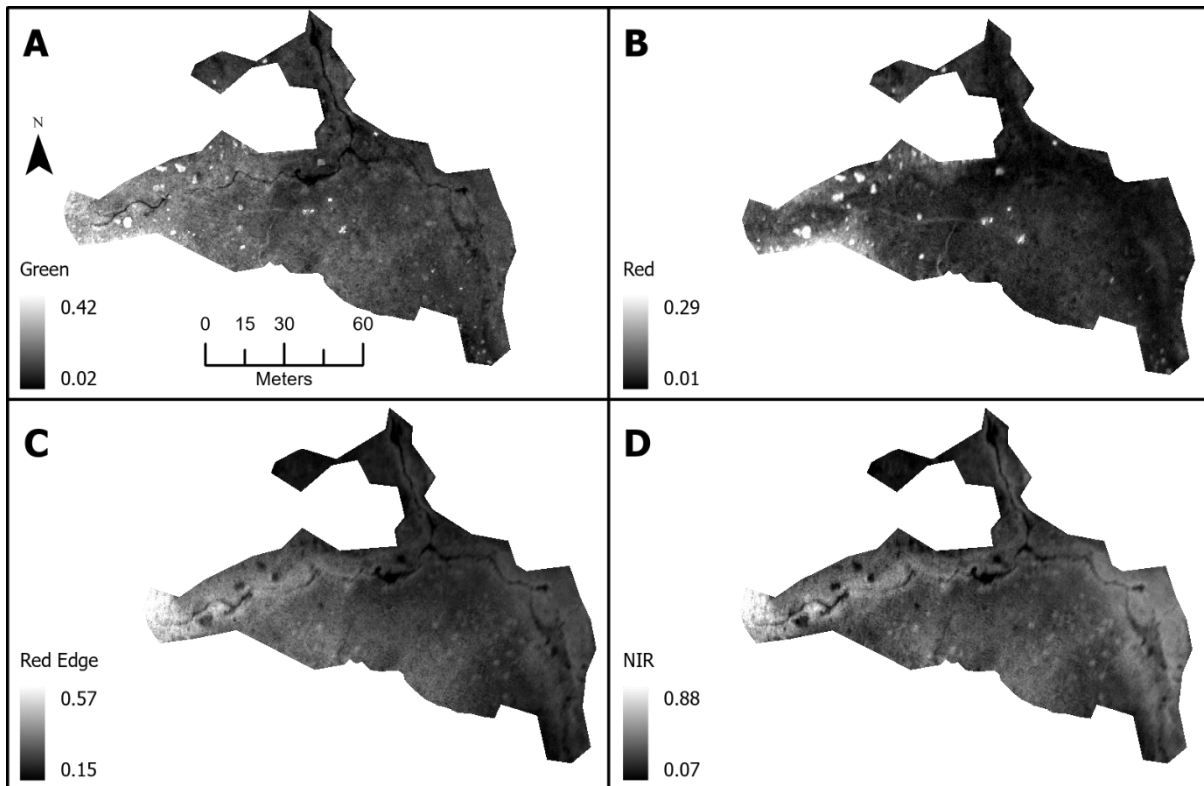

Figure A - 1. Multispectral imagery of Bonsai, Fortress Mountain, Alberta on August 26, 2020. Reflectance values in a) green; b) red; c) red edge; and d) near-infrared wavelengths.
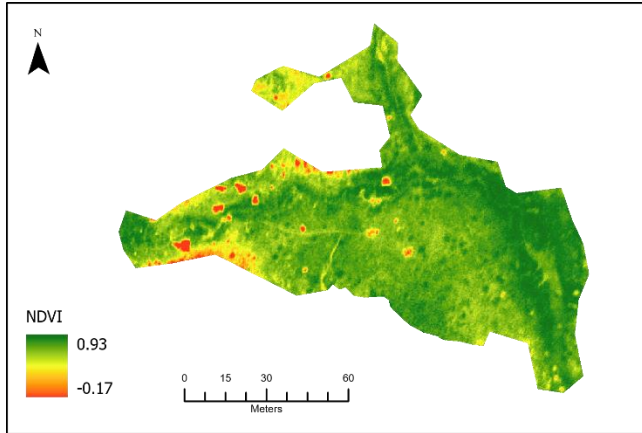
Figure A - 2. NDVI values derived from multispectral imagery of Bonsai, Fortress Mountain, Alberta on August 26, 2020.
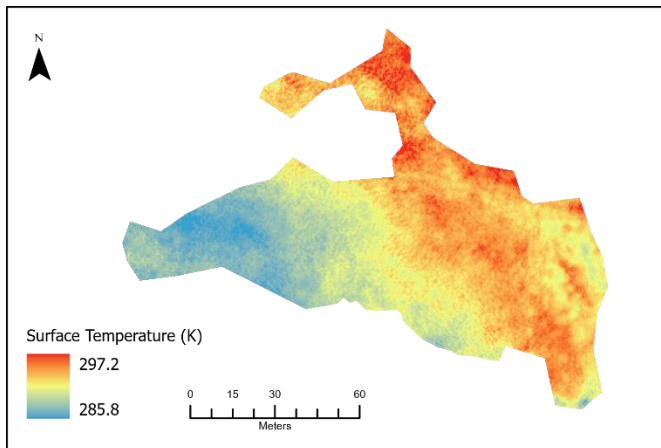

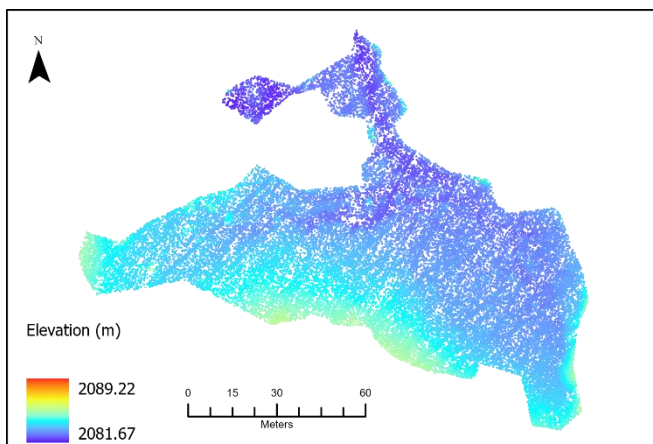**Figure A - 3. Thermal imagery of Bonsai, Fortress Mountain, Alberta on August 26, 2020.**

Figure A - 4. LiDAR point cloud displaying elevation of Bonsai, Fortress Mountain, Alberta on August 24, 2020.